Numerical Investigation of the Effects of Shrinkage and Thermal Loading on the Behaviour of Misaligned Dowels in Jointed Concrete Pavement

by

Cyril Levy

A thesis
presented to the University of Waterloo
in fulfilment of the
thesis requirement for the degree of
Master of Applied Science
in
Civil Engineering

Waterloo, Ontario, Canada, 2010

AUTHOR'S DECLARATION

I hereby declare that I am the sole author of this thesis. This is a true copy of the thesis, including any required final revisions, as accepted by my examiners. I understand that my thesis may be made electronically available to the public.

Cyril Levy

Abstract

Dowel bars in jointed plain concrete pavement (JPCP) have the important function of transferring wheel loads from one slab to the other, hence ensuring that the deflections on each side of the joint are kept almost equal. As well, the dowels should not impede the concrete pavement movements due to environmental effects (temperature and moisture). Dowel bar misalignment, attributed to deficient construction practice, is a major cause of joint distress or faulting by inhibiting the free movement of the slab at the joint. To prevent these issues, tolerance guidelines on misalignment levels are implemented by transportation agencies. Review of previous studies indicate that many researchers analysed the effects of dowel bar misalignment on pavement behaviour using a pull-out test, that is a force-based opening of the joint. These approaches neglect that joints movements in the field are strain-governed by non-linear temperature and shrinkage actions, leading to combined axial movements and curling of the slab.

In this study, the fundamental dowel bar behaviour under shrinkage and thermal loading was determined through detailed 3D finite element modelling (3D-FEM). To that end, models of dowel jointed concrete slabs were developed and subjected to realistic non-linear profiles of shrinkage and thermal strains. Studies were carried out on a single-bar model, taking into account bar-concrete friction and plastic concrete behaviour. The parameters that were investigated included different configurations and levels of bar misalignment and different friction coefficients between the steel and the concrete, simulating the use of bond-breakers. To interpret the results from the numerical analysis, criteria for concrete damage were developed and used in parallel with measures of joint load transfer efficiency; these were

obtained by examining the response of the slab under a Falling Weight Deflectometer (FWD) drop at the joint. The results were verified by comparing the outputs of a model consisting of one half of a slab to published data.

The analysis of the models revealead that none of the models showed signs of significant damage after the application of shrinkage and two thermal cycles. Analyses with up to ten thermal cycles did not indicate progressive accumulation of damage, suggesting that for the chosen parameters there is no the concrete around the dowel bar will not fail. Models with bars placed higher in the slab and bars with angular misalignment exhibited more damage than the non-misaligned models without reaching the damage criteria used in this study. The models did not exhibit the amount of damage reported in the studies on dowel bar misalignment having used pull-out tests. It was found that no significant difference existed between uncoated and coated dowel bars models results with regards to concrete damage at the joint. However, a high coefficient of friction between the dowel and the concrete, simulating dowel bar corrosion, proved to be the most detrimental to joint integrity. All of the models performed very well with respect to joint load transfer efficiency, suggesting that the plastic strains in the concrete around the dowel did not have a significant impact on joint performance for the realistic range of parameters investigated.

Acknowledgements

I would like to express my sincere gratitude and appreciation to my research supervisor Prof. Jeffrey West from the Civil and Environmental Department at the University of Waterloo for his support, perseverance and guidance that was indispensable for the accomplishment of this project. I also would like to express my appreciation to Prof. Susan Tighe for her interest in the research project and for serving on the examining committee.

I wish to thank my family for their support, care, and continous encouragement. Special thanks go to my parents for their dedication and to my brother.

My gratitude also goes to all my friends and colleagues for their support and help through the course of this research work.

Finally I would like to express my gratefulness to the Cement Association of Canada and the Natural Science and Engineering Research Council for their financial support.

Table of Contents

List of Tables

List of Figures

Chapter 1

Introduction

1.1 Problem Statement

Dowel bars in Jointed Plain Concrete Pavement (JPCP) have an important function: to transfer the wheel load from one slab to another, thus ensuring that the deflections on each side of the joint are kept almost equal. As well, the dowels should not hinder the concrete pavement to freely expand and contract under environment changes (temperature and moisture); the joint should allow horizontal movement of the concrete slab.

Dowel bars are generally placed in the concrete by positioning them on wire basket assemblies, or are inserted directly into the concrete by mean of a Dowel Bar Inserter (DBI) on the paver. Dowel bar misalignment can happen during the paving process due to initial misplacement. The dowel bar design position requires that the bar center be halfway through the joint edges, halfway through the slab upper and lower surfaces, and parallel to traffic direction. A dowel bar is considered misaligned when it has been translated or rotated from its design position. Misalignment is a major cause of joint distress or faulting by inhibiting the free movement of the slab at the joint. Lastly, a correlation exists between the extent and severity of concrete damage and the amount of dowel bar misalignment.

Transportation agencies impose limits on allowable misalignment levels to prevent such

troubles. However, there is currently no clear consensus among North America agencies on the amount of misalignment that can be tolerated. Some guidelines exist [1], and several studies have been carried out to determine tolerances on misalignment, generally showing that the misalignment tolerances were too conservative and could be loosened [2, 3, 4].

The general analysis of JPCP is also a recent field of study. The fundamental behaviour has been studied under experimental and numerical slab pull-out tests, and the various stages undergone by the concrete material are well documented [3, 5, 6]. The behaviour of the joint under wheel loads alone has been investigated as well, and the patterns of stresses around the dowel bar are known [5, 7]. Likewise, the inclusion of fatigue behaviour and non-linear environmental loading is an area in development.

1.2 Research Scope and Objectives

Dowel bar performance is a fundamental factor in the pavement life cycle. The overall objective of this study is to gain further insight into the behaviour of the doweled joint, by the mean of a realistic modelling of joint deflections caused by shrinkage and thermal loading. Realistic conditions, similar to those encountered on the field, are necessary to study the performance of pavements with misaligned bars that meet or exceed the current alignment tolerances.

The majority of studies on damage due to misalignment can be divided into two categories. Field studies were useful to determine the types and levels of joint damage or the performance of dowel placement methods, but were unable to separate the different factors responsible for concrete damage [2, 8, 9]. Laboratory or numerical studies used to simulate total joint opening due to thermal loads with a single pullout test, hence not taking into account neither cyclic loading nor the effects of slab curling [3, 4, 5]. With these results in mind, the objectives of this study are as follows:

1. Develop and calibrate a three-dimensional finite element model (3D-FEM) of a typical joint system, subjected to shrinkage and cyclic loading due to thermal changes; the

program ABAQUS was used for this purpose;

2. Determine, for various misalignment configurations and bar coatings: the total joint deflections (opening and uplift), bar forces and moments;

3. Determine the mechanisms that characterize the interaction between the dowel bar and the surrounding concrete, and the repercussions on joint deflections and dowel bar actions, as well as local damage of concrete;

4. Evaluate the joint performance for different configurations, using local damage criterion for concrete, and measures of load transfer efficiency of the joint.

1.3 Layout of the Thesis

This thesis is outlined as follows. Chapter 2 provides background information on concrete joint construction and specifications, and a review of the literature (technical reports, papers and thesis) available on the subject of joint performance, dowel concrete interaction and dowel bar misalignment. Chapter 3 contains a description of the 3D models developed using ABAQUS. Chapter 4 is devoted to the full description of a single bar 3D-FEM model, including preliminary sensitivity analysis. Chapter 5 presents the results of the single bar model, with a discussion of the various material stages including concrete failure and the verification procedure. Chapter 6 provides a summary of the conclusions and recommendations of the research.

Chapter 2

Background and Literature Review

2.1 Introduction

JPCP is created by inclusion of transverse joints into the pavement to control transverse and longitudinal cracking resulting from restrained deformations caused by temperature and moisture variations in the slab. The discontinuity created by the saw cuts may reduce vertical load transfer capacity of the pavement at the joint. Vertical wheel loads are transferred across the joint by a combination of aggregate interlock and load-transfer devices.

Current practice for joint load transfer in JPCP is to use either a series of round steel dowel bars spread across the joint within the PCC (portland cement concrete) or to rely on aggregate interlock if the truck traffic is low. The bond between the dowel bars and the concrete is minimized to allow the joint to open and close freely when subjected to longitudinal length changes of the slab. Recommended practice is for the dowel diameter to be approximately one eighth of the slab thickness with a dowel spacing of 300 mm, with a dowel length of approximately 456 mm [2].

Long term performance of the joint is highly dependent on the alignment of the dowel bars. Dowel bars should be placed parallel to the longitudinal axis of the road and the horizontal plane of the pavement to allow opening of the joint under thermal loading and

shrinkage. Longitudinal movements of the pavement may be restrained by misalignment of the dowel bars (joint locking) or subbase friction, however resistance to movement due to subbase friction is not as significant for slabs up to 12 m in length [2]. Although joint locking will have a minimal effect on vertical load transfer across the joint, it will result in high, localized stresses and cracking of the concrete near the joint. Progressive deterioration of the concrete resulting from restrained joint movements will decrease the efficiency of the bars to carry vertical loads, leading to faulting and reduced pavement service life.

This chapter is intended to provide some definitions and review the available literature on (a) general joint specifications and behaviour; (b) the effects of the interaction between the dowel bar and the concrete, including misalignment; and (c) shrinkage and thermal loading. This background will be useful to understand the key concepts governing jointed pavement behaviour, as well as provide models and parameters that we will later use to try and numerically simulate realistic doweled joint behaviour.

2.2 Contraction Joints and Dowel Bar Specifications

2.2.1 Contraction Joints Design

Two main types of structural joints are used in concrete pavement:

- Transverse contraction joints are a sawed, formed, or tooled groove in a concrete slab that creates a weakened vertical plane. It regulates the location of the cracking caused by dimensional changes in the slab, and is by far the most common type of joint in concrete pavements. Dowel bars are generally employed to transfer wheel loads across the joint and reduce slab deflections at the vicinity of the joint by transferring some of the load from the loaded slab to the unloaded slab.

- Longitudinal joints are joints between two slabs which allow slab warping without appreciable separation or cracking of the slabs. Usually, tie bars are used to transfer wheel loads across the joint and prevent lane separation, but sometimes keyways are

also used for this purpose.

Contraction joints are placed in the concrete to control the location of cracks resulting from the tensile and bending stresses caused by traffic loadings and environment loadings (thermal and moisture variations).

Transverse contraction joints are usually cut at right angle to the direction of traffic and spaced every three to fifteen metres depending on slab thickness, thinner concrete slabs requiring smaller spacings. The joints are saw-cut at one quarter to one third the depth of the slab. Typically, a contraction joint is first sawed very narrow (3 mm) to control cracking, then later widened (10 to 15 mm wide) to create a joint sealant reservoir. The concrete slab thicknesses usually range from 150 mm to 300 mm [10, 11].

Underneath the PCC slab lie the base and subbase courses. They provide additional load distribution, a uniform support to the pavement and a stable platform for construction equipment and contribute to drainage and frost resistance. The base also helps prevent subgrade soil movement due to slab pumping. The main materials used for the base include aggregate and stabilized aggregate (asphalt or cement treated base). Lower quality materials are generally used for the subbase.

The United States Federal Highway Administration (FHWA) provides some guidance on PCC pavement characteristics in Canada and Europe based on a scanning tour [12]. The standard concrete pavement in Ontario is a dowelled, jointed plain concrete pavement with a 4.25 m widened outside lane. Perpendicular transverse joints are randomly spaced at an average 4.25 m. Concrete pavement thicknesses range from 200 to 280 mm. The thickness design is based on both the 1993 AASHTO Guide for the Design of Pavement Structures and the Cement Association of Canada (CAC) mechanistic-empirical rigid design method. Since 1992, a 100 mm thick, asphalt-treated, open-graded drainage layer has been used for pavements on the highest-volume routes. Joints in concrete pavements are sealed with rubberized hot-poured sealant in 10 mm reservoirs. Regarding the base course, 100 mm thick, asphalt-treated, open-graded drainage layer is used for pavements on the highest-volume routes.

Load transfer mechanisms in JPCP are necessary due to the discontinuity created by the joint. Vertical load transfer is typically provided by aggregate interlock and/or dowel bars. Aggregate interlock is the mechanical locking which forms between the fractured surfaces along the crack below the joint saw cut. This is an adequate load transfer method for low-volume roads but is generally insufficient for higher traffic loads, especially trucks. Moreover, aggregate interlock is ineffective in cracks wider than about 0.9 mm. The dowel bars often provide the majority of load transfer across the joint [10].

2.2.2 Dowel Bar Specifications, Load Tranfer Efficiency

Dowel Bar Specifications

Dowel bars are round steel bars that provide a vertical mechanical connection between slabs without restricting horizontal joint movement. They increase load transfer efficiency by allowing the unloaded slab to assume some of the load before the load is actually over it. This reduces joint deflection and stress in the approach and leave slabs.

Dowel bars are typically 32 to 38 mm in diameter (at least one eighth of the pavement thickness), 460 mm long and spaced 305 mm apart. A typical layout is shown on Figure 2.1, with 11 dowel bars, of which 4 are in the wheel path. In order to prevent corrosion, dowel bars are either epoxy-coated or stainless steel. Dowel bars are usually inserted at midslab depth and coated on one side with a bond-breaking agent to prevent bonding to the PCC. Thus, the dowels help transfer load but allow adjacent slabs to expand and contract independent of one another [10, 11].

Load Transfer Efficiency

Characterization of joint performance is of primary importance to determine how a joint will behave under loading. Load transfer efficiency based on deflection is the main indicator used to determine how a concrete joint performs. When a wheel load is applied at a joint or crack, both the loaded slab and adjacent unloaded slab deflect. The deflection of the unloaded slab is directly related to joint performance. If a joint is performing perfectly, both the loaded

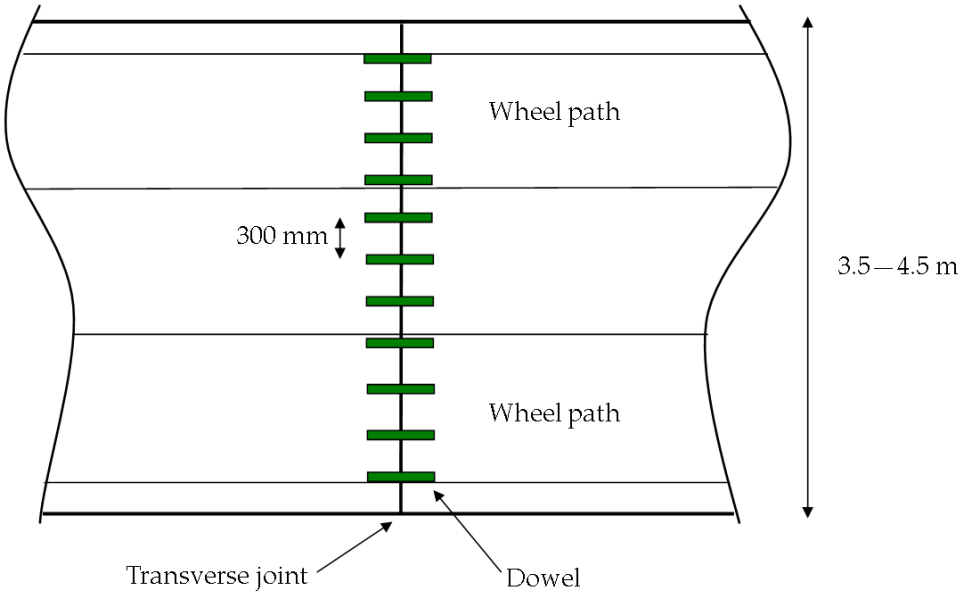

Figure 2.1: Typical dowel bar location on transverse joint [10]

and unloaded slabs deflect equally. Deflection load transfer efficiency (LTE_δ, often simply abbreviated load transfer efficiency, LTE) is defined by the Equation 2.1 [13, 14].

$$LTE_\delta = \frac{\Delta_u}{\Delta_l} \tag{2.1}$$

where Δ_u and Δ_l are the deflections of the unloaded and the loaded side of a joint, respectively.

Another common version of the deflection load transfer efficiency is:

$$LTE^*_\delta = \frac{2\Delta_u}{\Delta_u + \Delta_l} \tag{2.2}$$

Similarly, load transfer efficiency can be computed based on stress:

$$LTE_\sigma = \frac{\sigma_u}{\sigma_l} \tag{2.3}$$

where σ_u and σ_l are the bending stresses of the unloaded and the loaded slab respectively.

Ioannides and Korovesis [13] also introduced the transferred load efficiency (TLE):

$$TLE = \frac{P_T}{P} \tag{2.4}$$

where P_T is the load transferred across the entire length of the joint and P the total applied force.

Moreover Ioannides and Korovesis [13] present the load distribution factor, f_d, which indicates the load share of any given dowel bar from the total transferred load through a joint as expressed by the equation:

$$f_d = \frac{P_i}{P_T} \tag{2.5}$$

where P_i is the load transferred by a particular dowel bar.

2.3 Construction Practices, Misalignment Definitions, Tolerances

2.3.1 Dowel Bar Placement

Two different methods are currently used to place the dowel bars within the concrete joint [10, 15]:

- The basket-assembly method: dowel baskets are simple truss structures used to hold dowel bars at the appropriate height before concrete placement. They are left in place after the PCC is placed but do not contribute to the pavement structure.
- The dowel bar inserter (DBI): this method gained popularity since the late 1980s in North America, and Ontario has allowed the use of dowel bar inserters since the 1990s [12]. Dowel bars are inserted at predetermined locations by the slipform paver as the concrete is being placed.

For both methods, the joints are cut after the concrete has been in place for 4 to 12 hours.

Figure 2.2: Dowel baskets placed on a lean concrete base in advance of PCC placement [10]

Figure 2.3: Dowel Bar Inserter in action on Highway 401, Ontario, Canada [16]

2.3.2 Types of Misalignement

Dowel bar misalignment can be caused by a combination of misplacement during the initial placement (basket assembly) and movements during paving operation (bar insertion for DBI, vibration, joint cutting). A dowel bar can be misaligned in five different ways: three translations (transversal, longitudinal and vertical) and two rotations (horizontal and vertical), plus any combination of misalignments. Misalignment types and magnitude definitions are shown on Figure 2.4.

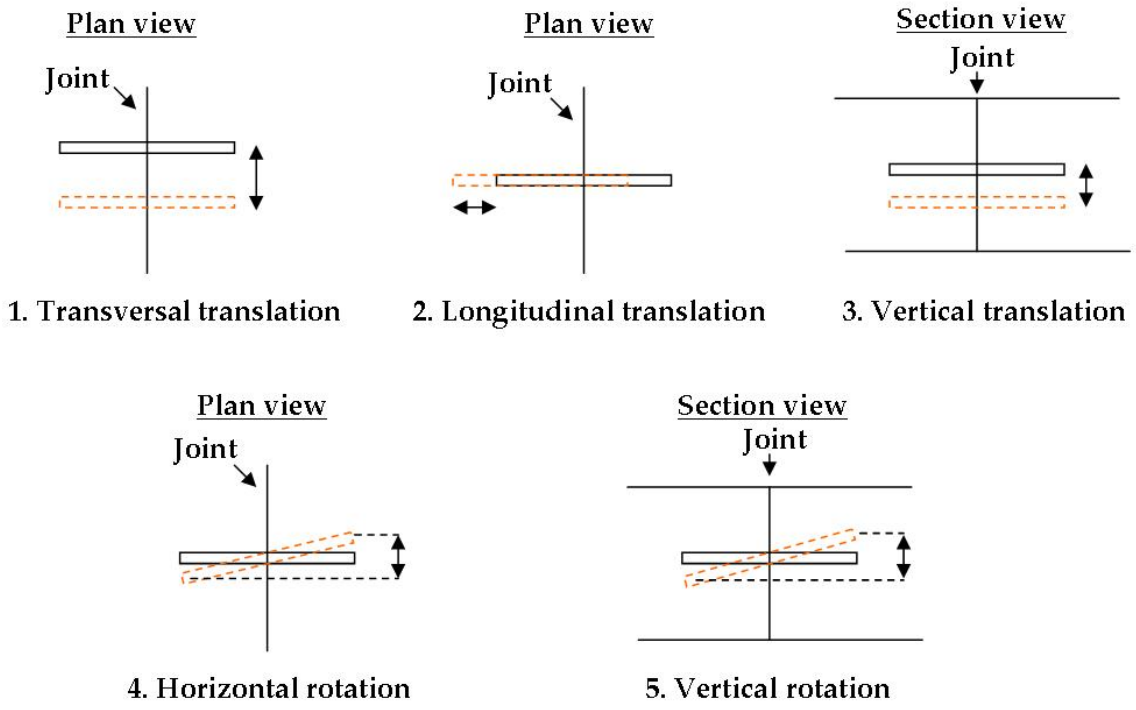

Figure 2.4: Misalignment types [2]

The main factors affecting dowel bar misalignment have been identified by Tayabji [2] for the two methods of dowel placement (Table 2.1).

Some comparison studies have been made regarding the influence of each method on misalignment values. Burati et al. [8] compared the efficiency of dowel placement by the basket assembly or the implanted dowel method. Surveys were conducted at selected concrete pavement locations constructed in the early 1960s in Alabama to provide distress

Table 2.1: Factors affecting misalignment depending on placement method [2]

Basket assembly	Implanted dowels
1. Basket rigidity 2. Quality control during basket fabrication 3. Care during basket transportation and placement 4. Fastening of basket to subbase 5. Location of saw cut over basket 6. Paving operation 7. Field inspection during construction	1. Implanting machine operation 2. Strike-off after dowel placement 3. Consolidation (vibration) after dowel placement 4. Location of saw cut over implanted dowels 5. Field inspection during construction

and dowel alignment data. No significant differences were found between the basket assembly and implanted projects with respect to joint related distress. Although faulting was not severe, 250mm thick pavement exhibited less faulting than did the 225 mm pavement. There was no evidence to identify dowel-bar misalignment errors as the cause of the pavement distress. Finally there was no statistical proof that either basket projects or implanted projects were superior.

Other studies confirm that there is no relation between the dowel placement method and misalignment; however some isolated field evaluations found that the misalignment levels were unacceptable for the inserted dowels, so that many highway agencies in the United States still specifically prohibit their use [1, 2, 17].

In a field investigation by the Missouri Department of Transportation [9], it was concluded that the Gunter-Zimmerman DBI provides similar dowel bar placement accuracy to dowel baskets. The DBI performed a little better with regards to horizontal skew, while dowel baskets held a very slight edge on vertical skew performance. Hence the authors recommended allowing the use of this particular DBI, and advocated separately evaluating any DBI made by another manufacturer.

Leong [15] reports a field evaluation of misalignment at various sections of Ontario highways, using radar and MIT-scan device. It was found that the number of joints having at least one bar exceeding the misalignment tolerance of 12 mm was higher in the case of basket installed dowel bars compared to DBI installed ones: 97.5% for the basket method against 88% for the DBI method. When the tolerance was increased to 25 mm, the survey showed that 53% of the joints with basket installed dowel bars and 30% of the joints with DBI installed dowel bars exceeded the new tolerance.

2.3.3 Tolerances on Misalignment and Control Equipment

Placement Tolerances

No clear consensus exists among North American agencies on the tolerable amounts of misalignment. Ontario dowel alignment specifications were reviewed in 2006 as a result of poor dowel bar placement on a project in 2003 [1]. In 2006, the MTO (Ministry of Transportation of Ontario) established a new set of requirements for dowel bar alignment as summarized below for 450 mm-long dowel bars.

Table 2.2: Requirements for dowel bar alignment

	Horizontal and vertical rotational alignments	Longitudinal shift	Depth
Acceptable level	$<$ 15 mm	$<$ 40 mm	94 to 106 mm for 200 mm-thick slab 106 to 127 mm for 225 mm-thick slab 113 to 153 mm for 250 mm-thick slab
Rejection criterion	$>$ 25 mm	$>$ 50 mm	$<$ 75 mm concrete cover at the slab bottom and top

Control Equipment

In order to make sure the pavement meets the requirements for good performance, the position of the dowel bars should be inspected at two stages of the construction [15]:

- During the paving process: inspection should give the exact locations of the joints before they are saw-cut.
- After the pavement is constructed: inspection should give the dowel bar positions to prove that the section complies with the specifications.

Non-destructive techniques (NDT) are the preferred way to determine the locations of dowel bars. The main methods of testing include the falling-weight deflectometer (FWD) and the magnetic imaging tools (MIT-Scan).

- The FWD applies a load pulse simulating a moving truck by dropping a mass onto a loading plate lying on the pavement, placed at different specified heights. The deflections of the pavement in response to the load are then usually recorded by geophones. Calculation of the elastic moduli using the joint displacement allows the dowel bars to be located along the joints.
- The MIT-Scan (and now MIT-Scan-2) is a recent device developed in Germany that uses the principles of pulse-induction. During testing, the transmitter emits a weak, pulsating magnetic signal and detects a transient magnetic response signal induced in the metal dowel bars. The methods of tomography are used to determine the location of the dowel bars.

2.3.4 Typical Forms of Joint-Related Distress

Several types of distress related to malfunctioning transverse joints have been identified in various studies [18]. Joint distresses affect both load carrying capacity and riding quality.

- Slab cracking: including corner breaks and transverse cracking at midslab (Figures 2.5 and 2.6).
- Joint spalling: cracking, breaking, chipping, or fraying of slab edges within 0.3 m from the face of the transverse joint (Figure 2.7).
- Faulting of the joint: difference of elevation of across a joint (Figure 2.8).

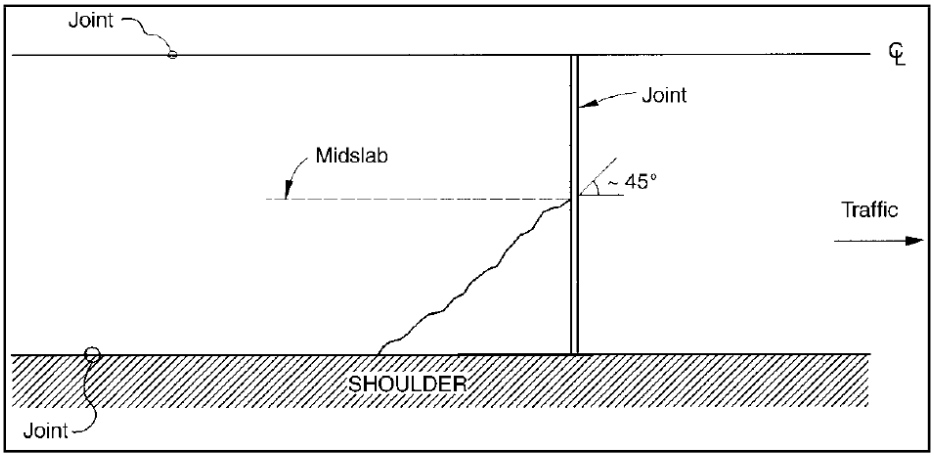

Figure 2.5: Corner breaks [18]

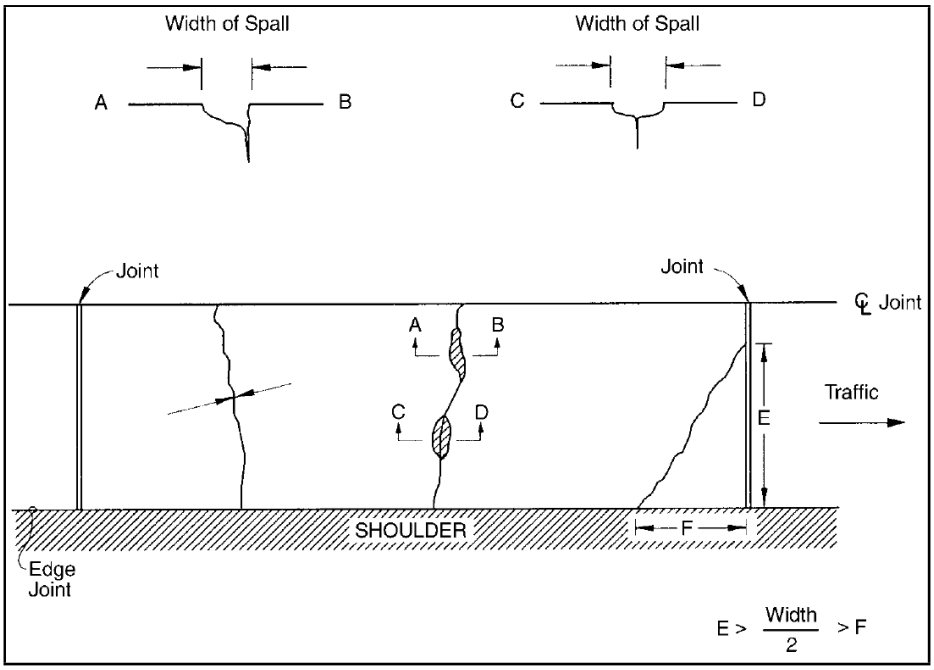

Figure 2.6: Transverse cracking [18]

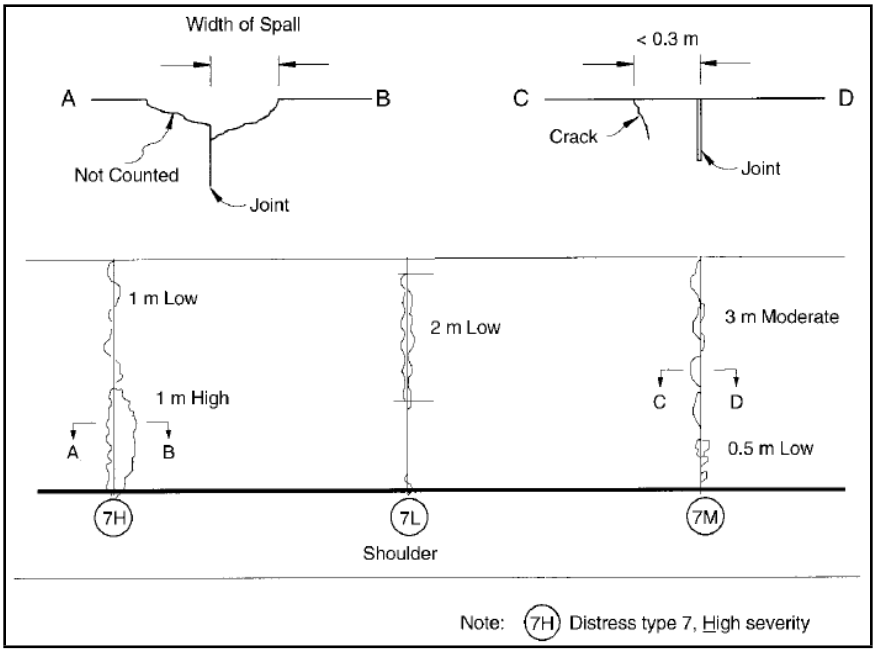

Figure 2.7: Joint spalling [18]

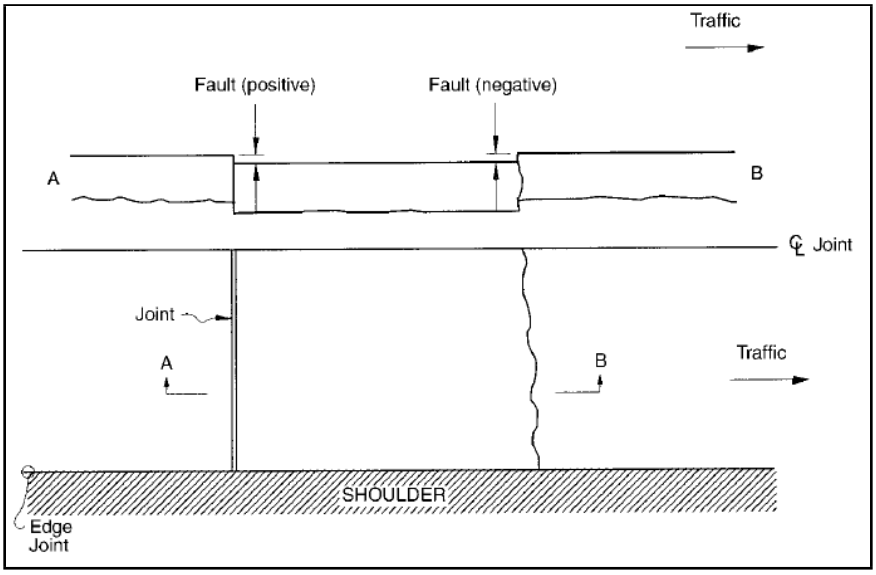

Figure 2.8: Joint faulting [18]

2.4 General Joint Performance

Bodosci et al. [19] presented the effect of pavement variables on joint deflection. Experimental concrete pavement was built in 1972 in Chillicothe, Ohio, by the Ohio Department of Transportation. The variables built into the pavement included two base types (190.5 mm-thick granular base and 101.6 mm-thick asphalt-treated base), different joint spacings (5.18 m, 6.4 m and 12.2 m), one section with skewed joints, and joints with no dowels, standard uncoated dowels, and plastic-coated dowels. A thorough investigation of vertical joint deflections produced by a two-axle truck with a 80 kN rear axle load and moving at 80 km/hr was presented.

The average morning deflection was more than twice the average afternoon deflection due to slab curling in the morning, while the average winter deflections were higher than in the summer, but not statistically significant. Joints supported on asphalt-stabilized base had smaller vertical deflections than those supported on granular base. This result was expected, because the stabilized base provides better support and minimizes pumping and erosion.

There was no significant difference between the average joint deflections of doweled and undoweled joints on stabilized base. Joint deflections were slightly higher with standard uncoated dowels than with plastic-coated dowels. Joint spacing had little effect on the average vertical joint deflection. However, when the cracks in the pavement were considered, the difference in average deflections was much more noticeable, and in general average deflections were greater when the distance between the cracks was larger.

Mannava et al. [20] conducted a test program to determine the load-deflection characteristics of a doweled joint interface, representative of a pavement joint. Three concrete strengths (17 MPa, 28 MPa and 45 MPa), three dowel diameters (19.0 mm, 25.4 mm and 38.1 mm) and two joint openings (8.9 mm and 20.3 mm) were tested on a $380 \times 380 \times 250$ mm slab with a single embedded smooth dowel. Vertical loading was applied on the loaded block until the dowels became plastic, where possible, and dowel displacements were recorded at the reacting block.

Approximate linear joint behaviour was observed to around 40 % of the ultimate load, followed by joint softening. It was observed that concrete strength, dowel diameter and joint opening width can have substantial impact on the ultimate strength and elastic dowel-concrete interaction of an interface containing a smooth dowel. A 25 % reduction of dowel diameter from 25.4 mm to 19.0 mm resulted in a similar stiffness reduction of approximately 20 % for specimens with the low concrete strength and smaller joint width. For specimens with the lowest concrete strength and smallest dowel diameter, slightly more than doubling the joint width led to a joint stiffness of about one-half its previous value. A 35 % reduction in concrete compressive strength from approximately 38 to 24 MPa caused the joint elastic stiffness to be reduced to approximately 45 % of its previous value for specimens with intermediate dowel size and small joint width.

Corley-Lay and Morrison [21] analyzed the performance of six sections of jointed PCC pavement constructed in 1967 on I-95 in North Carolina. All six sections were 230 mm thick with flexible paved shoulders and a joint spacing of nine metres, with or without dowels, and with different base types: 100 mm coarse aggregate base (CABC), 150 mm cement-treated subbase and 100 mm bituminous concrete base. Based on combined measures of surface pavement condition, faulting, and roughness, it was found that the test section with the best overall performance consisted of undoweled PCC placed on bituminous base course. This section remains in fair to good condition after 33 years, resulting in the most favorable annual cost. The poorest performances were pavements placed on very stiff cement-treated base or subbase. Presence of dowels resulted in lower average faulting by 1 to 1.5 mm at 33 years for sections where direct comparison was available. However, no doweled comparison section was constructed with bituminous base course.

Kim and Hjelmstad [22] invastigated various aspects of the structural behaviour of doweled joints in rigid pavement systems for airports by using non-linear three-dimensional finite element models. The models included two concrete slabs connected by dowels. The slabs and supporting layers were simulated by continuum solid elements, to capture the severe local deformation in the concrete slab in the vicinity of the wheel loads. The dowels

were simulated by using Timoshenko beam elements.

The structural behaviour of the doweled joint was investigated for various designs and loading conditions, including tire pressure, slab thickness, dowel looseness, and different landing gear configurations. Parametric analyses allowed a comparison of the amount of transferred load compared to the amount of applied wheel load. The engaged dowel was taken as a measure of the performance of the doweled joint. An engaged dowel carries at least 1 % of the transferred load.

It was found that nine engaged dowels achieved almost 99 % of the load transfer for a single-wheel load with 43 cm slab thickness. The load transfer efficiency was found to decrease with an increase in applied wheel load for the multiple-wheel load cases. Dowel looseness reduces load transfer significantly and increases maximum bending stresses up to 18% for the worst case. It was also found that small gaps between the dowel and the concrete cause a significant loss in the load transferred by the dowels.

Shoukry et al. [14] documented an evaluation of the accuracy of determining load transfer efficiency (LTE) of dowel jointed concrete pavements. For this purpose, FWD tests were conducted on pavement sites at different times during 2003, 2004, and 2005. Thirty transverse joints were tested along the slab edges as well as along the wheel-path. Trend analysis was performed to evaluate the effect of design features and site conditions on LTE. The effects of the seasonal temperature variations and the position of load application were also examined. Several key observations were made:

1. Load transfer efficiency was found to be a complex parameter that depends on many factors including load position, testing time, slab temperature, and load transfer device.

2. Testing time and season were found to have a significant effect on the measured load transfer efficiency. For the same joint, the load transfer efficiency measured in winter was found to be less than that measured in summer.

3. The slabs fitted with 32 mm (1.25 in) diameter dowels displayed higher variability of the measured load transfer efficiency than those fitted with 38 mm (1.5 in) diameter

dowels.

4. Joint opening changes daily and seasonally as the ambient temperature changes. As the amount of joint opening increases due to slab contraction during winter, the measured load transfer efficiency generally decreases.

5. As the slab temperature increases, the load transfer efficiency increases.

6. Poor correlation was found between the deflection-based load transfer efficiency and the percentage of the load transferred through the load transferring devices mounted across the transverse joint. The average transferred shear was between 8 and 21 % depending on the location of the FWD drop whereas the deflection-based load transfer efficiency ranged from 77 to 89 %.

However it can be noted that these conclusions were expected since most of the shear load is carried through the sub-layers to the ground; deflection-based load transfer efficiency still is an accurate indicator as far as riding quality is concerned, and even part of the joint role is to transmit deflections across the joint.

2.5 Effects of Misalignment on Joint Performance

2.5.1 Interaction Between the Dowel Bar and the Concrete

Riad [7] presented the nature and magnitude of the stresses at the dowel-concrete interface in rigid pavement joints. The state of maximum stresses induced around the dowel bars was examined using the three-dimensional finite element method (3D-FEM). The results obtained from the 3D-FEM simulation of pavement structures indicate that the current design of the regular coated dowel bar (450 mm long, and 32 mm diameter) satisfies the allowable compressive bearing stresses of concrete when subjected to the travel of the design axle load across the joint. Fatigue testing under 100,000 and 1,000,000 axle loads cycles suggested that these compressive stresses will eventually grow during the service life of the pavement structure.

Both 3D-FEM and experimental results reported by Riad [7] indicate the existence of two types of stresses at the concrete-dowel interface. The first is the development of compressive stresses at the top and bottom of the dowel, and the second is the formation of tensile stresses at both sides of the dowel bar. The tensile stresses were found to be more critical, as they exceeded the allowable tensile strength of the concrete material, which initiated a tensile crack in the concrete socket on the sides of the dowel bar.

The distribution of stresses along the dowel bar showed that the concentration of both tensile and compressive stresses takes place along the first 38 mm from the face of the joint, and diminishes shortly inside the slab beyond that point. The maximum induced stresses around the dowel bar in straight joints in comparison with those in skewed joints were found to be quite similar. Riad [7] concluded that skewing the joint did not enhance the performance of the dowel bar, and is considered to be an expensive ineffective refinement of the joint.

In a report by Shoukry et al. [23] the dowel pull-out force and the dowel-concrete coefficient of friction were measured using a laboratory setup of vibrating wire strain gauges embedded in both the dowel and the concrete. The gauges were set to measure the shrinkage strain induced in the concrete that surrounds the dowel as it cures causing the solidified concrete to clamp on the steel dowel. As the dowel is pulled out of concrete, both the dowel-pulling force and the elastic strain recovery in concrete were recorded versus the dowel displacement. Several observations were made. The measurements reveal that radial strain in concrete around the dowel is not uniform along the dowel circumference. The pull-out forces and push-in forces were found to be higher for the 38 mm diameter dowel bar than for the 32 mm diameter dowel bar. The debonding agents reduced the pullout and push-in forces required for the displacement of the dowel bar, as well as the radial and axial strains. Moreover, higher strains developed in the concrete when the uncoated dowel bar was completely pulled out. The forces required for pulling and pushing the dowel bar reduced with the increase in the number of cycles in the case of uncoated dowel bar. The pulling and pushing forces to displace the dowel bar also increased as the shrinkage of

concrete increased. The uncoated dowel bar pulled slightly out of concrete and could not be pushed back completely to its initial position, which was the not case with coated dowel bars.

A mathematical model was developed to estimate the friction coefficient at the dowel-concrete interface using a shrink-fit model, which proved to be valid. A shrink-fit model assumes that radial forces are generated at the concrete-dowel interface due to shrink fitting of the concrete over the dowel bar. The coefficient of friction is then calculated from the strains measured at the steel-concrete interface in the experimental slabs. The model found that the friction coefficient at the dowel-concrete interface was reduced to about one fourth with the application of a debonding agent. The silicone coat was observed to be more durable than the tectyl coat, as patches of tectyl coat adhered to the surface of concrete at the interface, and the surface of silicone coated dowel bar was less damaged when compared to tectyl coat dowel bar. Shoukry et al. [23] also developed 3D-FEM models recreating the experimental slabs with one dowel bar and expanding it to models with multiple bars. The models predicted higher stress fields in the concrete around the uncoated dowel bar during pull-out than that of coated bars. The stress field in concrete around coated dowels was very low. However, results were in poor agreement in the case of coated dowel bars.

2.5.2 Effects of Misalignment on Joint Performance

Tayabji [2] conducted a field investigation to develop placement tolerances for dowels at concrete pavement joints. A theoretical analysis of dowel misalignment was attempted too but not completed due to the complexity of correctly incorporating the three-dimensional nature of dowel misalignment. The effect of dowel misalignment was then investigated in the laboratory by conducting pullout tests on sections of concrete slabs incorporating a joint and dowels with different levels of misalignment.

Two 90 cm wide by 215 cm long slabs of 200 and 250 mm thickness were pulled apart gradually to obtain a joint opening of 6.4 mm. Rollers were used along the sides of the slabs to ensure that the pullout direction remained perpendicular to the joint during the

test. Misalignment levels per 460 mm length were 0, 6.25, 12.5, 25, 50 and 100 mm in the horizontal and vertical directions. The specimens were tested at 1, 3, 7 and 28 days.

Two different test procedures were used. In one procedure, a single misaligned dowel was used. In the other, a pair of misaligned dowels was used. For the simple misaligned dowel bar, pullout loads measured during these tests were relatively low and there were no significant differences in the load for the different levels of misalignments.

For the pair of misaligned dowels, the same level of misalignment with opposite directions were used (no roller were placed on the sides). It was shown that the pullout load increased with the level of dowel misalignment, but the magnitudes of the pullout load remained relatively low for misalignment levels of less than 25 mm. Also, no spalling was seen around dowel bars at the joint face for misalignment levels of less than 25 mm.

Khazanovich et al. [4] studied dowel bar misalignment and its impact on joint performance. The objective of this study was to develop justifiable tolerance levels that ensure that doweled joints do not cause high level of stress and damage due to misaligned dowel.

First the PCC-dowel interaction was modeled using the finite element method with ABAQUS code. Two approaches were explored: modelling contact behaviour using soft elements or using special contact elements. The first model was not used because large deformations cause significant distortion of the interlayer elements, making the solution unstable. Therefore, special contact elements are used; the friction model used in ABAQUS is an extended version of the classical Coulomb model. The pullout test was used as a benchmark test for establishing dowel-concrete interface parameters.

Two finite element models were used for this study: an axisymmetric model and a plane stress model. Providing contact pressure between the dowel and the concrete was done by assigning a positive change of dowel temperature. Comparison of pullout forces and mean contact shear stress showed relatively good agreement between the two models. Moreover, the parameters (friction coefficient and initial temperature) of 2D plane stress model and axisymmetric model were used later in 2D and 3D models of the misaligned dowel, respectively.

Two models were developed to study the effect of vertical dowel misalignment on joint behaviour: a simple 2D model and a more comprehensive 3D model. Khazanovich et al. [4] could not decisively conclude whether the 2D model was valid or not. The 3D models investigated different misalignment patterns: uniformly misaligned dowels, oppositely misaligned dowels or single misaligned dowels; however the study itself was limited to a unique dowel model, which did not take into account non-uniformity of misalignment. 4.6-meter long slabs were modelled, with a dowel length equal to 460 mm and a dowel spacing equal to 305 mm. The bottom surface was supported by a Winkler foundation with a stiffness value (k) equal to 54 MPa/m.

Two similar 2D and 3D models were used to investigate the effect of horizontal dowel misalignment on joint behaviour. A 2D multi-slab model was developed as well to the effect of misalignment of more than one dowel.

The following conclusions were drawn by Khazanovich et al. [4]:

- Non uniform dowel misalignment leads to significant increases in PCC stresses in the areas surrounding the dowels.
- A single misaligned dowel resulted in higher PCC stresses than in the case of uniformly misaligned dowels but lower than in the case of oppositely misaligned dowels.
- The multi-slab model suggests that if several joints are locked up due to dowel misalignment, a uniform drop in temperature may cause significant longitudinal stresses and lead to premature cracking if acting together with heavy axle loading and slab curling.
- The level of non-uniformity of dowel misalignment is very important.
- To model random dowel misalignment properly, at least three dowels should be modeled.
- Even in the case of oppositely misaligned dowels, misalignment up to 3.2 mm did not cause significant restraints on joint behaviour.

- A more comprehensive model should be used to verify and, if necessary, modify these recommendations.

Leong et al. [3] present an analysis of the potential impact of misaligned dowel bars on concrete pavement joint performance. Research was done to determine the upper limit on the allowable misalignment that could be tolerated before joint lockup and potential slab cracking could occur. The potential for joint lockup and slab cracking was studied with a series of three dowel bars and the finite difference method.

The force required to pull apart two concrete slabs connected by dowel bars at different alignments was analysed. Pullout tests were simulated with the finite difference program FLAC3D. Two 200 mm-thick slabs with a width of 900 mm and a length of 1000 mm were used in the study, and three 456×32 mm dowel bars were placed at 300 mm intervals. The contact between the concrete and the dowel bar surface was modeled with a grout material and initial concrete pressure was simulated by initial bond between the dowel bar and the surrounding concrete. The loading was simulated by a displacement applied to the slabs. Leong et al. [3] assumed that the concrete had a tensile strength of 3 MPa to define the onset of cracking.

For a single misaligned dowel bar, at the 14 mm joint opening, Leong et al. [3] reported an approximate 1 kN increase in the pullout force for a 5 mm increase in misalignment magnitude up to a misalignment magnitude of 20 mm. An approximate 4 kN increase occurred as the misalignment increased from 20 to 25 mm. The increase in pullout force as the misalignment increased from 25 to 30 mm was less than 1 kN. The results indicated no difference between misalignment in the horizontal plane or vertical plane in terms of pullout force.

For three misaligned dowel bars (same direction), at the 14 mm joint opening, Leong et al. [3] reported an increase of 5 kN in pullout force for a misalignment increase of 5 mm, up to a misalignment value of 20 mm for both the horizontal and the vertical plane. For an increase in misalignment from 20 to 25 mm, the pullout force increased by 10 kN. The difference in the pullout force between misalignment in the horizontal and vertical planes

was generally less than 2 kN. The tensile stress in the concrete near the midpoint of the center dowel bar reached 3 MPa for both scenarios.

With oppositely misaligned dowel bars, for a 14 mm joint opening, an increase in misalignment magnitude from 12 to 20 mm produced an increase in pullout force of 3 kN to 7 kN. As the misalignment increases from 20 to 25 mm, the pullout forces almost doubled, and was less than 2 kN for an increase in misalignment magnitude of 25 to 30 mm. The tensile stress in the concrete near the midpoint of the center dowel bar reached 3 MPa for both horizontal and vertical misalignment.

Overall, the results show a gradual increase in the pullout force for dowel bar misalignment magnitudes less than 20 mm. For an increase in the misalignment from 20 to 25 mm, a greater increase in pullout force was observed. Based on the stress distributions obtained from the simulations, cracking of the concrete was expected to occur if the dowel bar misalignment was more than 25 mm in either the horizontal or vertical plane.

A report by the Buch et al. [5] presented an experimental and analytical investigation on the pullout behaviour and the joint opening behaviour of misaligned dowel bars in concrete pavement joints. Experimental investigations were conducted to determine the fundamental joint opening behaviour of concrete pavements, and to evaluate the effects of dowel misalignment on joint opening behaviour.

A comprehensive laboratory experimental investigation was carried out to study the joint opening behaviour of misaligned dowel bars placed in contraction joints. The effect of the following parameters was investigated: dowel misalignment type (vertical, horizontal, combined); dowel misalignment magnitude (0, 6.25 mm, 12.5 mm, 19 mm, and 25 mm); number of misaligned dowels (one, two, three or five), and misalignment orientation (clockwise or counter-clockwise). The test setup consisted of two concrete slabs connected at the joint using steel dowel bars. The steel dowels were smooth round bars 32 mm in diameter, 460 mm in length and placed at the mid-depth of the slab. Two slab sizes were considered in the test: a smaller slab (overall dimensions 1.2 m $\times$ 1.2 m $\times$ 25 cm) that could accommodate one and two dowel bars, and a larger slab (overall dimensions 2.4 m $\times$ 1.8 m $\times$ 25 cm) that

could accommodate three and five dowel bars.

The results on the laboratory tests show that the pullout behaviour is characterized by two distinct regions: the initial fully bonded region and the debonded / post-slip behaviour region. In general, for a given misalignment type, as the magnitude of misalignment was increased, the amount of pullout force per bar to produce joint opening also increased. Test specimens with non-uniform orientation of misaligned dowels required a higher force per bar to produce joint opening compared to the alternate or the uniform orientation of misaligned dowel bars. For a given misalignment magnitude, the load induced per dowel to produce joint opening increased as the number of misaligned dowels increased. The results indicate that irrespective of the dowel misalignment type (vertical, horizontal or combined) and magnitude, the force required to open the joint in a pavement slab with non-uniform misaligned dowel bars is higher compared to alternate and uniform orientation of misalignments. Structural distress such as spalling was observed in the test specimens with non-uniform orientation of dowel bars. In particular, test specimens with non-uniform misalignment magnitude greater than 1/12 radians exhibited cracking.

Buch et al. [5] developed a 3D finite element model to further investigate the interaction between the dowel and the surrounding concrete. The following events or damage limit states were identified based on the material 3D stress state results, and are represented on Figure 2.9:

(A) Debonding/initial slip state. For all specimens, slip occurred after the pullout force per dowel increased above 5 to 7 kN (average bond shear stress τ_b of 0.21 to 0.30 MPa);

(B) Onset of concrete material inelasticity or cracking;

(C) Maximum principal stresses (S_{max}) exceeds the concrete tensile strength (f_t');

(D) Minimum principal stresses (S_{min}) exceeds the concrete compressive strength (f_c');

(E) Significant crushing (compressive inelastic strains);

(F) Significant cracking (tensile cracking strains).

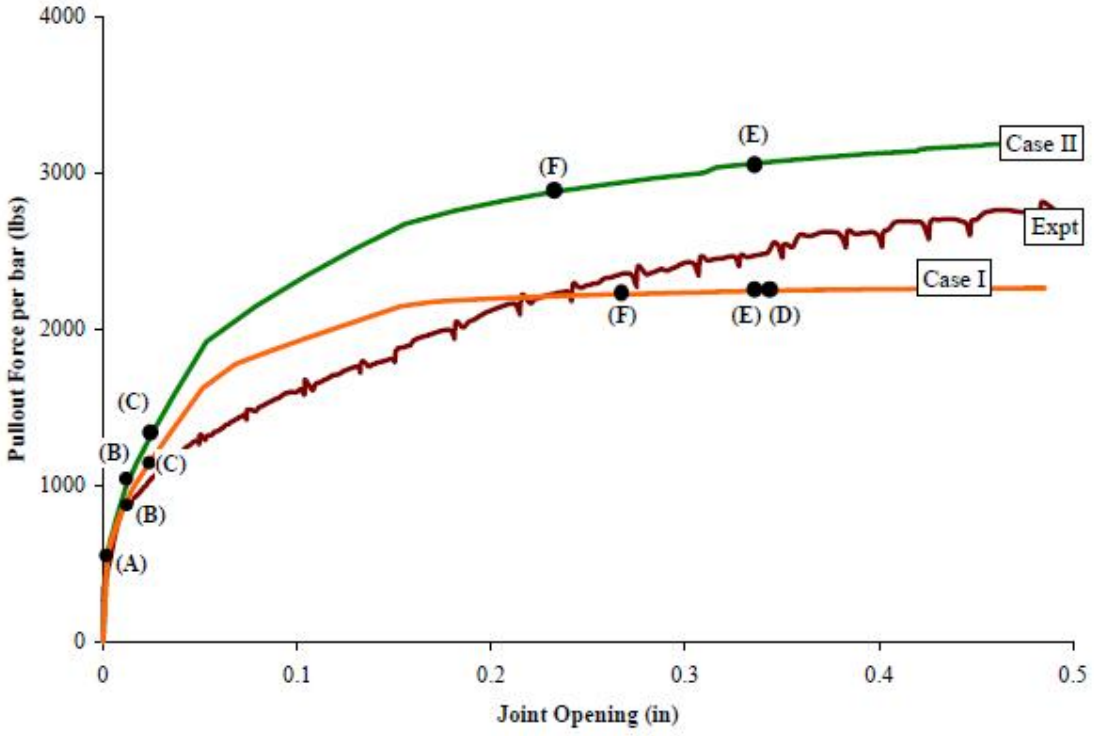

Figure 2.9: Occurrence of the different events during a pullout test [5]

The analytical results indicate that:

1. The debonding limit state occurs almost instantaneously irrespective of the dowel misalignment type, magnitude, orientation, etc. in the concrete slab.

2. As the misalignment magnitude (angle of skew) is reduced, the occurrence of a damage limit state is delayed as the joint is opened.

3. These analytical models, approaches and limit states are recommended for future analytical work on realistic pavement joints with thermal and traffic loads.

4. As the magnitude of misalignment increases, the events occur for smaller joint openings. Events B and C occur for joint openings less than 3.2 mm. The effects of non-uniform misalignment can be more detrimental than uniform or alternate misalignment. Events D, E and F occur at larger joint openings. As the misalignment magnitude increases, these events occur for smaller joint openings.

Buch et al. [5] presented preliminary results on the effects of load combined with dowel misalignment as well. A single dowel bar model and a three dowel bar model were developed. The models consisted of concrete slabs supported on a base layer and a subbase layer; the subgrade was modeled using a Winkler foundation. A monotonically static load up to 71 kN was applied on the concrete slab, directly on top on the dowel bar.

The results from the analyses indicated that the joint opening of 3.2 mm produced stress concentration zones in joints with misaligned dowels. These zones were similar to those predicted by the finite element models with joint openings only. A joint opening of 3.2 mm does not produce any significant distress for the misalignment magnitudes and type considered in this portion of the study. Applying the wheel loading changes the stress states and the stress concentration zones (for the horizontal misalignment) finite element models. The inelastic strains (compression and tension) induced in the concrete by the wheel loading increase much faster after the dowel misalignment exceeds 1/36 radians. The pavement specimens with three dowel bars with different types and orientations of misalignment with magnitude less than or equal to 1/36 radians do not undergo significant inelastic straining in compression (crushing) or tension (cracking) for total wheel loads equal to 71 kN.

Buch et al. pursued their analytical investigation further [6], applying it to predict the initial pullout bond stress of dowel bars with corrosion protection systems. The experimental pullout bond stress data on tectyl coated epoxy dowels, MMFX stainless steel and zinc clad dowel bars were provided by the Michigan Department of Transportation (MDOT). The pullout bond stress for zinc clad dowel bars was the highest followed by the MMFX steel and the tectyl coated epoxy dowel bars. The three dimensional finite element models (3D-FEM) developed in by Buch et al.[5] were used to validate the experimental results. The bonding pull-out force results from the 3D-FEM model compared favorably with the experimental results. The results showed the formation of events / material damage limit states occurred during the dowel pullout behaviour of zinc clad dowel bars.

The results of the study of combined effects of load and different pullout bond stress data showed nominal stresses and strains forming around the dowel bar at a joint opening

of 3.2 mm. These stresses were produced due to the self weight of the concrete slabs. As wheel loads were applied, the bearing stresses in the concrete surrounding the dowel bar increased. The magnitude of the dowel pullout bond stress was a function of the dowel surface preparation and irregularities at the contact interface with the surrounding concrete. The results from the numerical (3D-FEM) analysis indicated that if the dowel pullout bond stress was greater than 0.77 MPa, then limit states B (onset of concrete material in-elasticity) or C (cracking stress exceeded) occurred before dowel slip (limit state A). Thus, if the dowel pullout stress exceeded 0.77 MPa, there was potential for concrete cracking or inelasticity in the concrete at the dowel–concrete interface. Buch et al. [6] found that this was not acceptable, because concrete cracking or inelasticity would lead to fatigue deterioration and eventual failure (functional or structural) of the joint with repeated cycles. The current MDOT specification of maximum pullout bond stress limited to 0.41 MPa (60 psi) provides a resistance factor (or factor of safety) of approximately 1.87, which was reasonable in the authors judgement. The authors recommended carrying a detailed study on the pullout bond stress using suitable MDOT approved bond-breaking agents.

2.6 Effects of Moisture and Temperature on Concrete Pavement

2.6.1 Creep and Shrinkage of Concrete

Creep and shrinkage are aging effects that can significantly modify concrete properties and long-term behaviour. Shrinkage is contraction happening due to the loss of moisture content in concrete after it is poured. Two types of shrinkage can be distinguished [24, 25]:

- Autogenous or endogenous shrinkage is a volume change that happens immediately after the cement and water come in contact during concrete mixing. These early age volume changes are typically ignored in design of concrete structures since their magnitude can be much less than shrinkage resulting from drying.

- Drying shrinkage is the result of loss of water due to environment action (evaporation,

diffusion) and can lead to slab curling and warping.

Creep is permanent deformation of concrete under sustained load. Aside from material properties, the three main factors that determine the amount of creep in concrete are the magnitude of the load, its duration and the time at which it is applied. In pavement, the only permanent stresses are caused by concrete self-weight.

Goel et al. [26] compared various recent creep and shrinkage models to available experimental data. The ACI-209R-82 model, the B3 model, the CEB-FIP model code 1990, and the GL2000 model were evaluated. To compare the various prediction models, results obtained by these models were compared with the experimental results of Russell and Larson (1989) and the RILEM data bank. The researchers concluded that the ACI-209 codal provisions were applicable to concretes under standard conditions, and that the GL2000 model performed best for shrinkage predictions in the concrete. Ultimate shrinkage strains ranged from 500 to 1000 microstrains, as seen on Figure 2.10. However, it must be noted that in the experimental studies the researchers have reviewed and compared, the theoretical results to have been conducted in specific environments and for different durations varying from 7 to 5,000 days. Therefore, a definitive conclusion on the validity of each model might be somewhat questionable.

The previous results actually apply only to the maximum shrinkage happening in concrete; drying shrinkage is indeed a highly non-uniform phenomenon. Shrinkage rate increases non-linearly from the bottom to the top of the slab due to greater moisture loss happening on top of the slab [27, 28, 29].

Kim and Lee [27] suggested an analysis of differential drying shrinkage in concrete, in which creep of concrete is considered. The authors recall that the non-uniform moisture distribution in concrete causes differential drying shrinkage. Tensile stress occurs on the exposed surface of concrete structures and may result in crack formation. It was observed that this residual stress was significantly affected by creep of concrete, essentially in the form of shrinkage-induced stresses. The results from the theoretical analysis were compared with experimental shrinkage strain measured in a concrete slab.

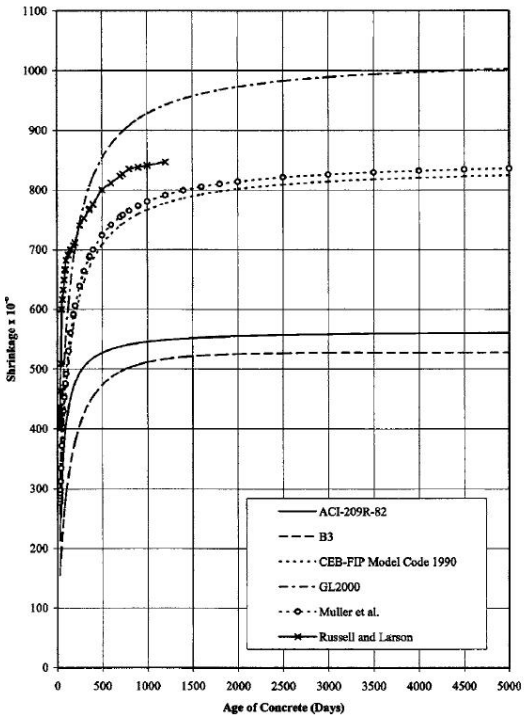

Figure 2.10: Time-dependent variation of shrinkage for concrete having 32.45 MPa compressive strength at 28 days [26]

Two different concrete mixes were selected: Mix I with a water/cement ratio of 0.65 and a 28 MPa compressive strength, and Mix II with a water/cement ratio of 0.40 and a 44 MPa compressive strength. Drying shrinkage at a given time t (in h) was represented as a one-dimensional function of slab depth from drying surface y (in m). The distribution of internal drying shrinkage strains (including creep effects) can be described by Equation 2.6, where $\lambda = {}^{y}/_{\sqrt{t}}$ is the Boltzmann variable and a and b are regression coefficients whose values are presented in Table 2.3.

$$\epsilon_{sh}(y,t) = ae^{b\lambda} \tag{2.6}$$

Table 2.3: Regression coefficients of Eq. 2.6 [27]

Specimen	a	b
Mix I	353×10^{-6}	-415.4
Mix II	238×10^{-6}	-426.1

From the results of this investigation on differential drying shrinkage, the following conclusions were drawn:

- The internal drying shrinkage strain significantly varied according to the depth from drying surface, and the stresses induced by this differential drying shrinkage could cause surface cracks. Thus the differential drying shrinkage must be considered in the analysis of thick concrete structures.

- The residual stress inside the slab is greatly reduced by the creep of concrete. It is therefore necessary to consider creep in the analysis of differential drying shrinkage.

Weiss et al. [30] investigated early-age cracking in restrained concrete structures. The goals of this study were: (1) the development of test methods to assess the potential for shrinkage cracking; (2) the development of a theoretical model to predict cracking; and (3) the evaluation of nonexpansive shrinkage reducing admixture (SRA). The parameters of the performed tests were: the type of specimen (ring and slab), concrete strength (33 and 90 MPa), and the amount of shrinkage reducing admixture (0, 1 and 2 %).

Several specimens were tested for compressive strength, fracture properties, and free and restrained shrinkage (slabs restrained at end, or at end and base). Weiss et al. [30] noted first that high strength concrete cracks considerably earlier than normal strength concrete due to higher initial strain rate, earlier initial gain of stiffness and reduced creep relaxation. Significant reductions in free shrinkage were observed with the addition of SRA: shrinkage reduction at 50 days were 25 % (1 % SRA) and 45 % (2 % SRA) for normal strength concrete and 30 % (1 % SRA) and 42 % (2 % SRA) for high strength concrete. Moreover the initial rate of shrinkage is lower with the addition of SRA. In restrained shrinkage tests, it was observed that the addition of SRA significantly effects the age at first cracking. A 2 % addition of SRA drastically increases the age at first cracking in all specimens while there was no cracking at the end of the test (50 days) in the normal strength concrete restrained slabs. Delaying the age at first cracking results in narrower cracks in all specimens.

The addition of SRA did not produce significant effects on the compressive properties of normal strength concrete, but reduced the compressive strength of high strength concrete by 16 %, as well as introducing a slight retarding effect. However Weiss et al. [30] pointed out that SRA increased concrete flow properties, therefore reducing water needs to obtain comparable workability and counteracting the negative effects on compressive strength. Fracture tests results showed comparable results with or without the use of SRA.

Theoretical modelling of shrinkage was attempted. Concrete being a quasi-brittle material, stable crack growth occurs prior to the peak stress and strain softening is observed in the post-peak region. In addition to time development of material properties, concrete is sensitive to time-dependent creep under loading, which results in increased complexity in the computation of the state of stress. Shrinkage strains were determined experimentally but creep strains were approximated using the CEB-FIP model. Weiss et al. [30] derived the stress distribution from the total strain, computed as a sum of initial loading strain, creep strain and differential shrinkage strains, and were able to derive the age of shrinkage cracking and the maximum stable crack extension.

Results indicate that the theoretical predictions for the age at first cracking compared reasonably well with experimental data. It was observed that tensile creep reduces tensile stress development, and that characterization of early-age tensile creep is critical for a complete understanding of shrinkage cracking.

Gilbert [24] addresses the effects of shrinkage on the serviceability of concrete structures and presents a model for predicting time-dependent shrinkage strain. In this model, the total shrinkage strain ϵ_{cs} is divided into two components, endogenous shrinkage, ϵ_{cse}, which is assumed to develop relatively rapidly and increases with concrete strength, and drying shrinkage, ϵ_{csd}, which develops more slowly, but decreases with concrete strength. At any time t (in days) after pouring, the endogenous shrinkage is given by

$$\epsilon_{cse} = \epsilon^*_{cse}(1.0 - e^{-0.1t}) \tag{2.7}$$

where ϵ^*_{cse} is the final endogenous shrinkage strain and may be taken as $\epsilon^*_{cse} = (3f'_c - 50) \times 10^{-6}$, where f'_c is in MPa. The basic drying shrinkage ϵ^*_{csd} is given by

$$\epsilon^*_{csd} = (1100 - 8f'_c) \times 10^{-6} \geq 250 \times 10^{-6} \tag{2.8}$$

The drying shrinkage is taken as

$$\epsilon_{csd} = k_1 \epsilon^*_{csd} \tag{2.9}$$

The variable k_1 is given as

$$k_1 = \frac{k_4 k_5 t^{0.8}}{t^{0.8} + (t_h/7)}$$

where $k_4 = 0.8 + 1.2e^{-0.005 t_h}$ and k_5 is equal to 0.7 for an arid environment, 0.6 for a temperate environment and 0.5 for a tropical/coastal environment.

A paper by Lim et al. [31] describes a series of discrete test and analysis methods as an integrated approach for the estimation of time- and position-dependent humidity changes and shrinkage in early-age concrete. The total moisture loss in concrete was assumed to be a result of autogenous drying and conventional external drying. Humidity reduction due to autogenous drying or self-desiccation (Δh_{AS}) is expressed as a function of the degree of hydration in terms of strength ratio, which can be determined by the maturity and strength relationship (Equation 2.10).

$$\Delta h_{AS} = \frac{a + \alpha}{b} \tag{2.10}$$

where α is the degree of hydration and a and b are experimental coefficients ($a = 0.1$ and 10 for cylinder specimen).

Moisture loss due to external drying was estimated by finite element analysis based on the nonlinear diffusion theory. Estimated humidity reduction is then used to estimate shrinkage potential in the concrete by applying a linear shrinkage coefficient, which may be determined by tests. The total humidity reduction at time t and depth d from drying surface

is expressed as:

$$\Delta h_{TOT}(d,t) = \Delta h_{DS}(d,t) + \Delta h_{AS}(t) \tag{2.11}$$

The empirical equation determined by Parrot (1988) was used for the humidity profile in drying shrinkage:

$$h_{DS}(d,t) = h_a + (a - h_a)\frac{1}{1 + (b \cdot t/d^n)} \tag{2.12}$$

where h_a is the ambient humidity and a,b,n are experimental coefficients. By applying a linear shrinkage coefficient, another function of time and position was formulated for the prediction of shrinkage potential of the concrete, in the form of shrinkage strain.

Lim et al. [31] pointed out that the coefficients of the equations were specifically featured for the cylinder specimen used in their study and may not be relevant to other concrete having different mixture proportions, curing conditions, or shape.

2.6.2 Thermal Effects

Heath and Roesler [28] investigated the transverse cracking of Jointed Plain Concrete Pavement (JPCP) test slabs under environmental loading. The test slabs were constructed with Fast Setting Hydraulic Cement Concrete (FSHCC) in Palmdale, California. Cores drilled above the transverse cracking indicated top-down cracking had occurred. Heath and Roesler [28] indicated that initial strains in the slab were most likely due to thermal contraction of the concrete after construction. After two months, strains at the top of the slabs had increased significantly while the strains measured in the bottom of the slab remained constant. It was determined that this increase in the top of slab was a result of drying shrinkage, not thermal contraction. The differential strains through the slab thickness from the combined effect of drying shrinkage and night time temperature gradients resulted in bending stresses, which exceeded the concrete strength and caused transverse cracking.

Significant corner curling of the field concrete slabs was recorded, with as much as 2.5 mm daily movement under environmental conditions. The corner deflection data suggested that the slab corners were permanently curled upward due to the differential drying shrinkage in

the slab. An analysis of the slab corner deflections was performed by comparing the measured to predicted values from finite element analyses using non-linear slab temperature profiles and drying shrinkage differentials. For 3D-FEM analysis, the slabs were 200 mm thick, the concrete modulus of elasticity was 35 GPa, the temperature was considered uniform across the depth of the slab (no gradient was applied since it was estimated that bending from temperature was neglectable compared to that of drying shrinkage), and the shrinkage law was taken as bi-linear with a gradient of 250 $\mu\epsilon$. The measured data and 3D-FEM showed differential drying shrinkage had resulted in the corners of the slab being in a permanently curled up position, resulting in an unsupported corner condition at all times.

By analyzing the differential shrinkage and a negative temperature distribution, the highest tensile stresses from environmental loading were found to be at the middle of the slab at the surface. This validated the field findings that crack initiation began at the top of the slab and propagated downward.

Heath and Roesler [28] made recommendations focused on the use of fast setting hydraulic cement concrete (FSHCC) in rigid pavement rehabilitation, which may not be applicable to PCC pavements and may be contrary to previous experience with rigid pavements constructed using PCC. From their experience, the researchers first emphasized that predicting the drying shrinkage gradient through a field slab was the most difficult factor to quantify as this was influenced by creep, elastic deformations and environmental conditions. General recommendations that might be applicable to newly constructed PCC pavements include the following:

- Flexible bases (for example asphalt concrete mixes) are preferred as they will deform under long-term environmental loading and thereby decrease stresses in the slabs. Stiffer bases (for example lean concrete bases) will not allow any relaxation of environmental stresses. Furthermore, bases with a high frictional resistance (e.g. lean concrete bases or open graded mixes) should not be used without a bond breaking layer between the base and slab. The high frictional resistance can create significant tensile stresses in pavement slabs when the concrete cools from a high temperature of

experiences high shrinkage.

- Shorter joint spacing (less than 4.5 m) will decrease environmental and traffic load stresses.

- The time of day and environmental condition when paving is performed should be considered. It is usually preferable to pave under cool, moist conditions and not during the heat of the day.

Liu and Fwa [32] developed a closed-form model to analyze the effect of nonlinear temperature distribution on thermal warping stresses in concrete pavements. The effects of the following factors on warping stresses in concrete pavement were analyzed: horizontal slab dimensions, slab thickness, slab elastic modulus, modulus of subgrade reaction, and temperature profile across slab thickness. The general form of quadratic equation used to describe the non-linear temperature distribution is:

$$T = A_T + B_T z + C_T z^2 \tag{2.13}$$

where T is the temperature in degrees, z is slab depth from the middle, and A_T, B_T and C_T are coefficients that can be derived from measured temperature data.

All of the cases analyzed concluded that the assumption of linear temperature distribution would lead to significantly underestimate the maximum warping stresses at the top surface of pavement slab, and significantly overestimate the maximum warping stresses at the bottom surface of the pavement slab.

Mahboub et al. [33] examined field data from a section of heavily instrumented concrete pavement on the Gene Snyder Freeway, Louisville, Kentucky, and developed a 3D-FEM model using the ANSYS program to predict the mechanical behaviour of the rigid pavement. The three selected slabs were 3.66 m wide and 228 mm thick, with a 153 mm thick base of dense-graded aggregate. The effects of environmental loads (mainly temperature-induced loads) were compared to that of traffic loads by collecting the data with the road open to traffic and with the road closed to traffic.

Field observations revealed that the slabs responded to temperature cycles by curling. However, upon the reversal of environmental conditions, the slabs never reached a fully flat position. Therefore, Mahboub et al. [33] assumed that the slabs in this study were manufactured with some level of residual strain (caused by concrete curing, loss of moisture, and shrinkage). Hence, distributed body forces were applied to the model to simulate the inital strains and residual stresses in the slab and adjusted during model calibration.

Using the field data and modelling, an attempt was made to quantify the effects of traffic and temperature loads on concrete slabs. It was found that the contribution of the ordinary highway traffic induced pavement response was rather small compared to the temperature-induced response (ratio of 20 %). Therefore, the trends of the change in strains in concrete pavement are dominated by the change in air temperature, while the static vehicle load and traffic load induced a relatively small fluctuation in the strain change tendency. This was an important finding according to the authors, with potentially serious ramifications in concrete pavement design and analysis.

A study by Wells et al. provided a detailed analysis of the strain that develops a result of environmental loads [34]. The study characterizes slab response immediately after construction (first 72 h after paving) and also addresses seasonal effects over the first 10 months following construction. A heavily instrumented test section was constructed on SR-22 in Murrysville, Pennsylvania, to help characterize slab response to environmental loads better. The pavement consisted of 305 mm JPCP constructed on top of a 100 mm asphalt-stabilized base and 127 mm of densely graded subbase. Static strain and climatic data collected through the first 10 months after construction (August 2004 through June 2005) were analyzed to interpret pavement response to environmental loads as a function of location with respect to joint proximity, depth within the slab, and level of restraint applied to the slab.

During the first 72 h after paving, the largest strain measured was along the transverse joint. This finding was because of the absence of a curb and gutter, so that there is no restriction on movement from the outside portion of the slab. The longitudinal strain along

the centerline exhibited the lowest strain, since movement was restrained by the presence of a previously constructed adjacent lane. The decrease in strain between that measured at the corner in the transverse direction compared with the longitudinal and diagonal along the centerline joint was about 50 μstrain, which corresponds to a stress of 1.2 MPa. The magnitude of the strain decreased with increasing slab depth, which indicated that the bond between the base and the bottom of the slab was sufficient to restrain slab deformation. Also, the temperature fluctuations at the bottom of the slab were less than those at the top of the slab.

Wells et al. [34] exhibited interesting findings about the strain that developed during the first 10 months after construction. The average strain in the fall was around -450 μstrain, whereas the average strain in the winter was -600 μstrain. The ambient temperatures increased during the spring and summer; this resulted in a decrease in the average strain to -250 μstrain. The daily strain fluctuations were the largest in the spring. Moisture-related shrinkage was typically less than thermal strain. Thermal strain was found to be twice as high as the drying shrinkage the first winter after construction. A substantial amount of drying shrinkage occurred within the first 50 days after construction. Variations in drying shrinkage occur not only through the depth of the slab but also across the surface of the slab. Moisture-related shrinkage was the lowest at midpanel, where its exposure to the air was limited to the surface of the slab. Moisture-related shrinkage was the highest along the lane-shoulder joint because the tied curb and gutter were not constructed until a few weeks after the lane was paved. Moisture-related shrinkage continued to increase through the winter months but then begined to decrease during the spring, when precipitation events occurred more frequently. Wells authors remarked that this gradual lessening of drying shrinkage makes makes it possible to quantify the amount of reversible shrinkage that will occur throughout the slab.

Hejamadi [35] studied the measured behaviour of slabs fitted with an alternative design to dowel bars called “Shokbars” and compared it to the measured behaviour of slabs fitted with regular dowel bars. The effect of slab-base friction on the expansion and contraction of

concrete slabs was studied and the thermal stresses known to cause the top-down transverse cracking at the midslab were investigated. The Shokbars, developed by Shoukry in 2001, aimed at reducing the magnitude of contact stresses while preserving the load transfer efficiency of doweled joints through the service life of pavement. The Shokbars consisted of two 38 mm internal diameter, 6.35 mm thick and 50 mm long protective sleeves around the dowel which bond permanently to the surrounding concrete, while allowing the dowel to slide freely in them as shown in Figure 2.11. The Shokbar was designed such that each sleeve embeds itself in the jointed slabs.

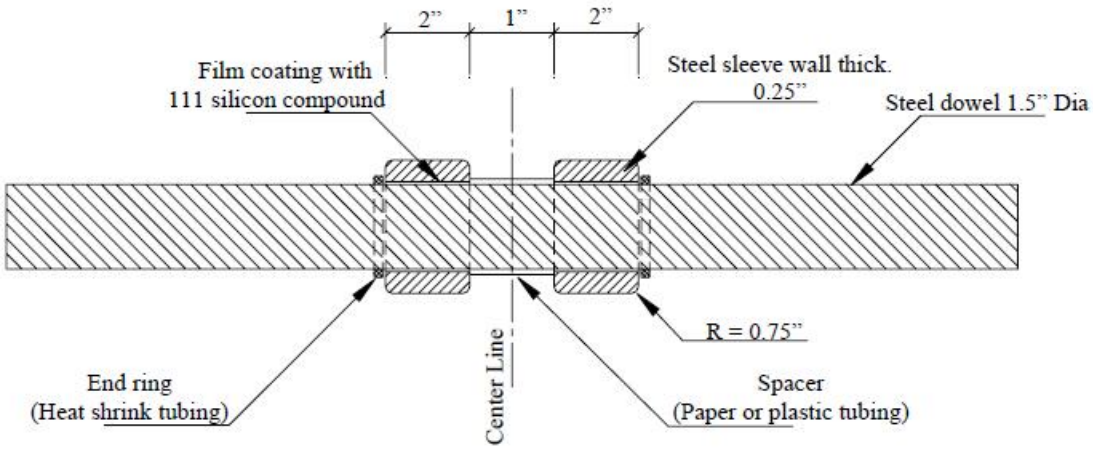

Figure 2.11: Design of Shokbar [35]

Hejamadi [35] used the thermal diffusivity theory to develop a method to calculate the temperature and the thermally induced strain at different depths through the slab thickness given the time history of weather parameters (air temperature, solar radiation, relative humidity, and wind velocity). This method is capable of calculating the slab temperature for a 24 hour period and also for a sequence of days including days with light rain and cloud cover. Equations for the strains developed at the slab top and bottom were also presented. The temperatures calculated by the method were compared with the values measured from the test slabs. The results from the proposed model were found to be in reasonable agreement with the experimentally measured data from the slabs. The results

indicate that the new dowel bar design reduces the concrete slab strains especially during the initial stages of concrete setting. The Shokbars reduce permanent residual strain in the slab, lower the axial forces in the dowels considerably and help in relieving curling stresses in the pavement. The measured data show that slabs fitted with Shokbars have symmetrical joint opening compared with the slabs that were fitted with regular dowel bars. Hejamadi also reported that Shokbars were previously experimentally tested for load transfer, and maintained steady values of load transfer efficiency across the joint through 10 million cycles of fatigue loading.

Chou and Lee [36] presented the results of a field experiment project conducted at the Taiwan International Airport during slab replacement maintenance. The variation of slab curling stresses during a day and during a year were analyzed. The following conclusions were drawn:

1. Concrete shrinks immediatly after it is poured, and, at the early stages of curing, drying shrinkage dominates the joint movements.

2. Slab temperature, especially on the surface, is greatly affected by air temperature. The change in temperature of the interior of the slab is affected by a time-delay factor.

3. Temperature variation at the top of the slab is much greater than that at the bottom. This results in a larger movement at the top than at the bottom. The computed maximum thermal stresses in tension were around 1 MPa.

2.6.3 Shrinkage and Thermal Effects Modelling

Combined shrinkage effects and thermal loads can lead to axial and bending stresses in the slabs. Axial actions on a slabs, apart from dowel action, include two main actions: (a) shortening and expansion of the slab in a horizontal plane, and (b) the friction of the slab on the base. It is therefore important to identify the friction law that governs the interaction between the slab and the base. Bending stresses are caused by slab curling, which is a result of the shortening and expansion of the slab in a non-uniform manner across the cross-section.

Since curling occurs concurrently with slab contraction/expansion, all slab actions due to shrinkage and temperature are reviewed in a second section. More detailed derivations of the required parameter values are included in the next chapter.

Slab-Base Friction

Limited data are available concerning the friction between the concrete surface and the underlying base layers.

Lee [37] studied the characteristics of friction between concrete slab and base and proposed a model for the determination of friction between concrete slab and base. The paper reviewed the existing studies for friction between the slab and the base; in particular the variation of the friction coefficient with the slab displacement was analyzed. The Coulomb model for friction is expressed as follows:

$$\begin{aligned} F &= A + BN \\ \mu &= \frac{F}{N} = \frac{A}{N} + B \end{aligned} \tag{2.14}$$

where μ is the friction coefficient, F the frictionnal force, A a constant to represent adhesion characteristic between two surfaces, B a constant to represent shear characteristic between two surfaces and N the weight of the sliding object.

Deformability of the sliding object and base results in preliminary displacement before sliding occurs. Preliminary displacement is affected by base stiffness, while the maximum friction coefficient is affected by the roughness of the sliding plane (Figure 2.12). The effect of movement cycles was also addressed: it was found that after a few cycles (3 or 4), the variation of the friction coefficient was insignificant (Figure 2.13).

Lee [37] proposed a base friction model, associated with correction factors to convert it to different conditions. The variation of the friction coefficient with slab displacement is approximated as a linear increase followed by a plateau. The slab displacement corresponding to μ_{max} is called preliminary displacement (PD); those factors are not used directly since

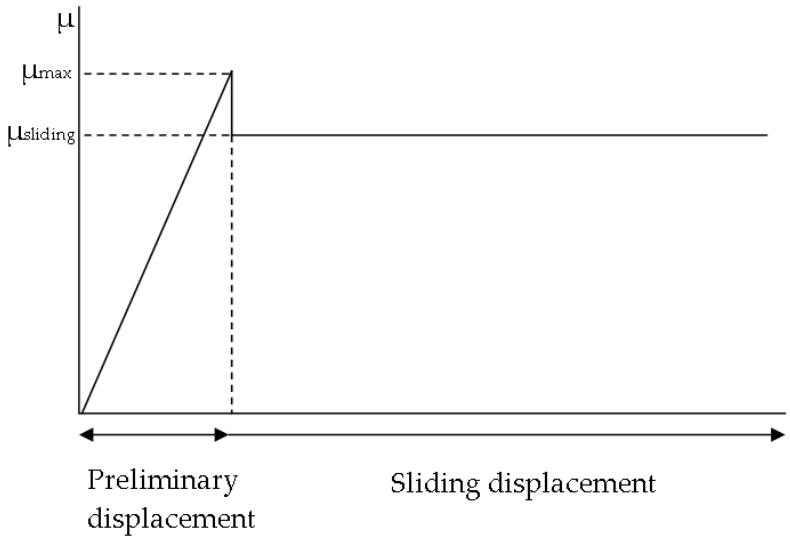

Figure 2.12: Friction coefficient as a function of displacement [37]

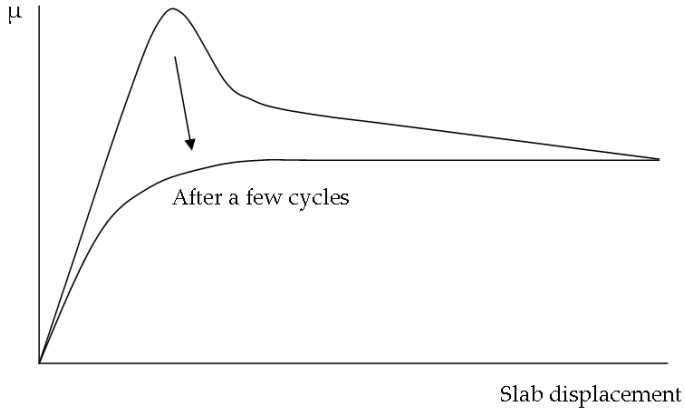

Figure 2.13: Typical shape of friction coefficient-displacement curve [37]

they depend on test conditions. The equations can be written as:

$$T\mu = \begin{cases} T\mu_{max} \cdot (Disp/TCPD) & \text{if } Disp < TCPD \\ T\mu_{max} & \text{if } Disp \geq TCPD \end{cases} \tag{2.15}$$

where $Disp$ is a displacement of an element of the concrete slab, $T\mu_{max}$ is corrected μ_{max}, TPD is corrected PD after accommodating for the difference of test conditions and actual pavement conditions, and $TCPD$ is corrected TPD to provide equivalent frictional stress

acting on the slab in the simplified model and in actual curves.

Zhang and Leng [38] investigated the effect of pavement material properties as well as slab/base interfacial characteristics on the shrinkage-induced stresses in concrete pavements is investigated by application of an analytical shrinkage stress model. The model is based on the interfacial friction stress transmitted between slab and base when concrete shrinks. A bilinear model describing the frictional stress-slippage behaviour of the slab/base interface was adopted in the modelling. The following limiting assumptions were made:

1. Concrete behaves in a linearly elastic manner.

2. All shrinkage-inducing deformation is uniformly distributed throughout the concrete slab.

3. The base beneath the concrete slab is a rigid material and the deformation under action of the horizontal friction forces is ignored.

4. The effects of warping and creep of concrete are not taken into account.

Friction stress acting on the slab surface is modelled as

$$T = \begin{cases} \frac{T_0}{\delta_0}|u| & \text{for } 0 \leq |u| \leq \delta_0 \\ T_0 & \text{for } \delta_0 < |u| \end{cases} \tag{2.16}$$

In Equation 2.16, u is the average slippage along the thickness of the slab relative to the base at location x, which is given by $u(x) = u_\epsilon(x) + u_c(x)$, where u_ϵ is the displacement induced by concrete shrinkage, u_c is the displacement resulting from internal axial stress, T_0 is the steady-state frictional stress, δ_0 is the corresponding slippage as the frictional stress achieves T_0. The relationship between friction stress and slab slippage is shown in Figure 2.14.

From the model calculations, it was found that when concrete shrinks, a symmetrical non-uniform axial tensile stress field in a pavement with finite length is formed. The axial shrinkage stress distribution in the pavement takes the form of an initial linear increasing

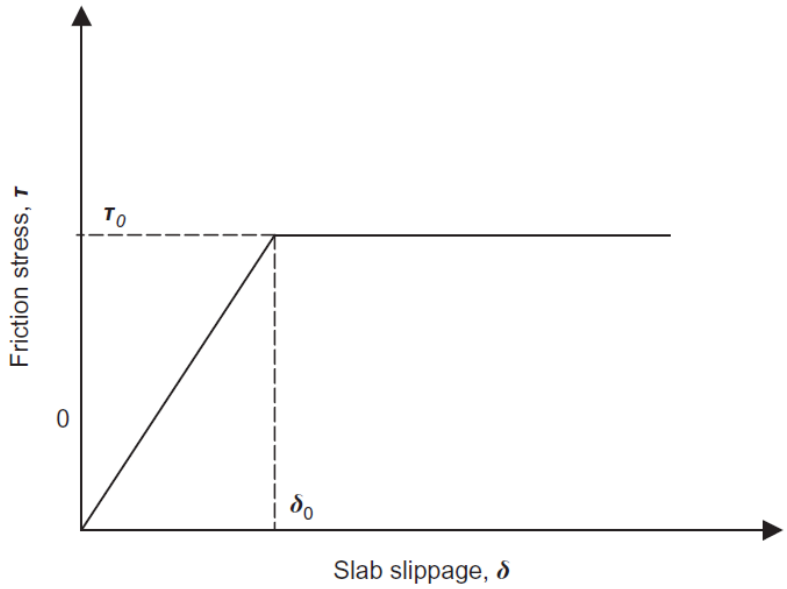

Figure 2.14: Friction stress law used in the model by Zhang and Leng [38]

portion from both slab ends and a plastic-like portion with an almost constant axial stress in the middle part of the slab. The ratio between the linear increasing portion and the plastic-like portion is governed by the degree of concrete shrinkage strain. After a long period of build-up, the stress distribution in the slab can be seen as an almost triangular shape, with a peak stress at the centre of the slab. Zhang and Leng [38] concluded that the model is applicable only in the case where shrinkage of concrete is uniform throughout the depth of slab, which is not realistic, as mentioned previously.

Slab Curling due to Shrinkage and Temperature

As mentioned before, differential shrinkage and thermal strains across the depth of the pavement lead to slab curling and warping. Higher temperatures during the day at the top of the slab lead to downward bending of the slab, while during the night the top temperature is lower than the bottom temperature, inducing upward slab bending, as illustrated on Figure 2.15.

Jeong and Zollinger [39] reports the results of a concrete slab constructed at Texas A&M University to study temperature, moisture, and creep effects on the curling and warping

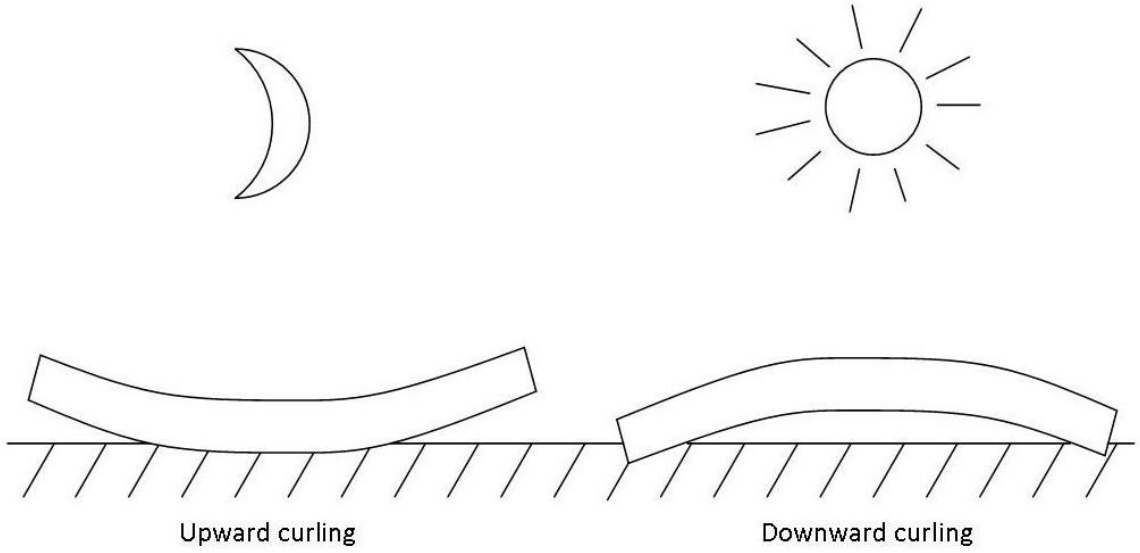

Figure 2.15: Night-time and day-time slab curling

behaviour of jointed concrete pavements under different curing conditions. Curling and warping of a slab are caused by moisture or temperature differentials through its depth. Jeong recall that curling and warping result in a loss of support along the slab edges or at the slab interior. Moreover, restraint stresses form within the concrete slab since the weight of the slab prevents unhindered curling and warping deformation from taking place.

The fully instrumented test-slab system was constructed as follows: a saw-cut joint was placed at the midslab location, where one half of the slab was cured with a standard curing compound and the other half was mat-cured. The concrete slab was 305 mm thick, with twelve 31×457 mm dowel bars placed at 305 mm, the subbase was 102 mm thick lean concrete.

The initial and final setting times of the concrete slab were determined to correspond well to the initiation point of slab curling and warping. The half of the slab cured with insulation mat had much less shrinkage and creep before final set compared with the other half under membrane curing. Because of the substantial amount of shrinkage and creep after mat removal, the mat-cured half had a larger magnitude of shift in tensile strain with time compared with the membrane-cured half. Drying shrinkage created a higher level of

tensile strain in the top of the slab, increasing the upward movement of the slab, while creep strain caused a shift in the strain cycles with respect to time.

The movement of slab was restrained at doweled joints resulting in bending moments in the dowel bars. Thus, the trends of the bending moments of dowel bars were similar to those of the joint displacements. There were obvious linear relationships among vertical corner displacements, concrete strain differences, and dowel bending moments. Equivalent temperature differences for shrinkage and creep effects were calculated by ISLAB 2000. Substantial increase of the equivalent temperature difference at 2 years after placement implies that the shrinkage significantly affects long-term warping behaviour of the slab.

2.7 Literature Review Summary - Key Concepts and Findings

Dowel jointed concrete pavement is a complex pavement system, that includes multiple parameters and is subjected to various actions. As such, different ways of modelling jointed pavement behaviour have been proposed, which has lead to various results and interpretations. This section is aimed at providing a summary of the key concepts and findings regarding concrete pavement that are needed for realistic modelling of its behaviour.

Two methods are currently in use for the placement of dowel bars in the concrete slabs: the basket-assembly method and the dowel-bar inserter method (DBI). Most studies conclude that with regards to dowel bar misalignment and joint damage, no significant difference exist between the two methods. Dowel bar misalignments are determined on the field by the use of a falling weight deflectometer (FWD) or the MIT-Scan device.

Three types of methods of measure of joint performance exist. The first method, which is widely used in field and experimental studies, is a visual observation of concrete distress or damage, in particular at the vicinity of the joint. The second method is a calculation of joint efficiency based on joint deflection or load transfer across the joint, and is mostly used in field studies employing an FWD. The third method uses numerical studies that rely mostly on the analysis of stress or strain levels in the concrete surrounding the dowel bar to evaluate

the possibility of failure.

Studies on dowel bar misalignment have all been based on a pull-out test or the numerical simulation of a pull-out test, and usually come to the same conclusion regarding fundamental joint behaviour: initial slip and debonding of the steel from the concrete characterized by a quick increase in the dowel bar axial force, followed by a slow increase in bar force as concrete inelastic behaviour appears and develops (the rate of pull-out being kept constant throughout). The studies on misalignment agree on a misalignment tolerance limit of approximately 25 mm per dowel length in most cases. 25 mm is also the lower limit for the rejection criterion for vertical misalignment used by MTO. The two major drawbacks of the studies based on a pull-out test are: (1) that to incur damage in the concrete, they apply joint openings that are much higher in comparison to what is experienced in real pavemements; and (2) that only axial behaviour is studied, while slab curling is neglected.

Slab curling is due to the non-linear strain profiles imposed to the concrete slab by shrinkage and thermal variations. Daily thermal variations are responsible for joint opening/closing and uplift/lowering, while shrinkage induces a permanent upward curling to the slab that stabilizes after one or two years. Slab friction plays here a role in counteracting the slab expansion and contraction. For accurate simulation of slab joint movements, it is hence necessary to model shrinkage and thermal loading using non-linear strain profiles.

Chapter 3

Choice of Model and Parameters

3.1 Objectives and Methodology

As mentioned in the literature review, a doweled pavement is subjected to multiple combined actions, from the environment (shrinkage), from thermal changes, from slab-base friction, from dowel-concrete interaction, and from traffic loads. The underlying mechanisms are understood on a separate basis, but usually have not been investigated when combining multiple phenomena. In particular, combined dowel action (friction and misalignment) and slab curling has not been really investigated; yet, real pavements undergo such actions.

The following conclusions have been made from the review of the available literature on the subject of doweled joints. The fundamental dowel-concrete interaction, including the effects of misalignment and dowel bar coatings, has often been studied by using a single pullout test, so there is a need to study the effects of cyclic results with simulated environmental loads. Moreover, laboratory setups only simulate the axial contribution from the thermal changes (joint opening and closing), and shrinkage is used only as a mean of providing contact pressure between the dowel and the concrete; in laboratory environment, the curing conditions are much different that real conditions and will most of the time lead to quasi-uniform shrinkage in the absence of a base under the slab, neglecting non-linear effects

occuring in the reality. Therefore, there is a need to investigate combined dowel action and slab curling. In particular, no study was found on environmental loading associated with the effects of dowel bar misalignment or coatings. Since environmental actions, which impose strains to the concrete slabs, and wheel loadings, which are pressures applied on the surface of the slab, have two distincts mechanisms of action, it is useful to the study first the fundamental slab response under environmental loading (and superimpose later wheel loadings). The fundamental behaviour of the doweled joint with slab curling has not been studied so far; besides, in most cases field studies will not be able to separate the effects of wheel loading from the effects of environemntal loading, making it impossible to isolate slab curling effects.

Therefore, to study the fundamental behaviour of the doweled joint, and gain insight on the interaction between the dowel bar and the concrete, a 3D-FEM model of a simplified pavement subjected to shrinkage and thermal loading was developed. Realistic loading conditions and contact parameters were selected for this matter. The commercial, general-purpose finite element analysis software, ABAQUS, was used to develop and analyze the models due to its ability to model concrete brittle damage (concrete damaged plasticity model).

Two different 3D-FEM models were developed: the Model 1 with a single dowel bar and the Model 2 with multiple dowel bars. The single bar model was used to study the fundamental interaction between between the dowel bar and the slab subjected to environmental loading. The multi-bar model was used primarily to verify that the calculated joint deflections were consistent with field surveys, thus ensuring the loading function and the parameters used in the single bar model were in a realistic range. The general and specific research objectives for Model-1 are the following:

- Determine the mechanisms that characterize the interaction between the dowel bar and the surrounding concrete, when the slabs are subjected to repeated environmental loading in combination with shrinkage;

- Determine the repercussions of local joint behaviour on joint deflections and dowel bar actions, as well as local damage of concrete;
- Carry out a parametric study on various parameters, most importantly misalignment configurations and the use of bond breakers (friction between dowel and concrete);
- Estimate the effects of the aforemontioned parameters on joint performance, based on criteria of load transfer efficiency and local concrete damage.

3.2 Model Geometries

The pavement system upon which the models are based was selected based on a typical PPC highway pavement designed for use in Canada. Two 4.2 m wide $\times$ 8.5 m long adjacent slabs are modeled, connected with 11 dowel bars placed at 300 mm center to center, at mid-height of the slab. The dowel bars are 32 mm in diameter and 450 mm in length, the slab thickness is 250 mm. An initial joint width of 10 mm is chosen; it is adequate because when the slabs are saw cut, a crack propagates from the cut to the bottom of the slab, and the resulting aggregate interlock is very weak at transferring loads. The slabs lie on top of a 125 mm-thick asphalt treated open graded drainage layer (OGDL), and a 600 mm thick subbase (including a possible extra granular base). The dimensions of the model are shown on Figure 3.1. For the analysis, the actual pavement is modeled with two different geometries: the first model consists of one half of one interior bar (Model 1), and the second model consists of five and a half bars representing half of the full pavement considered (Model 2).

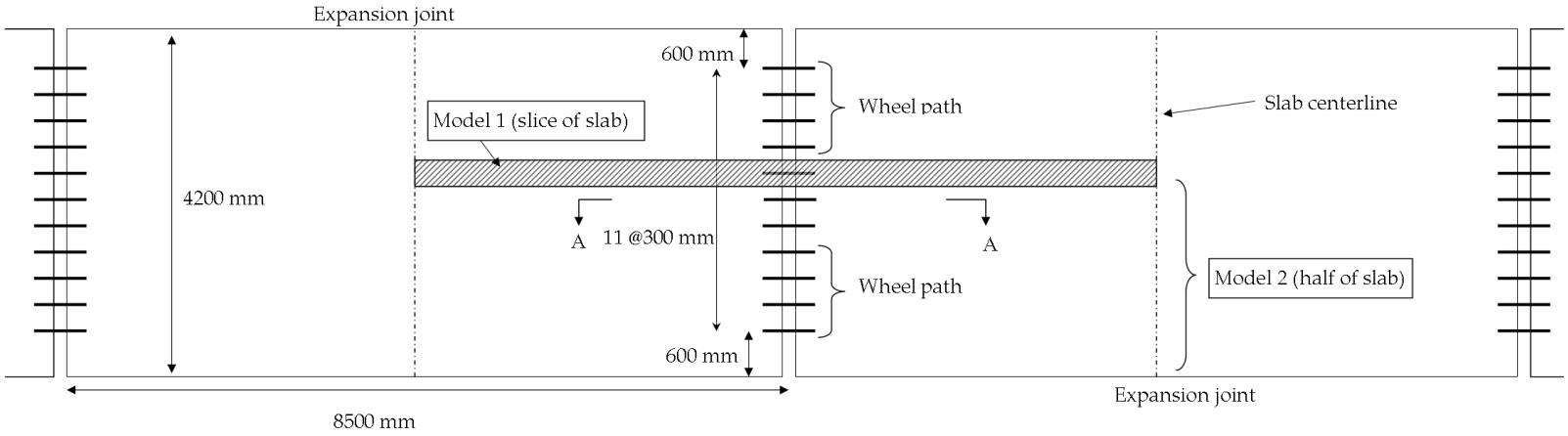

1. Plan view

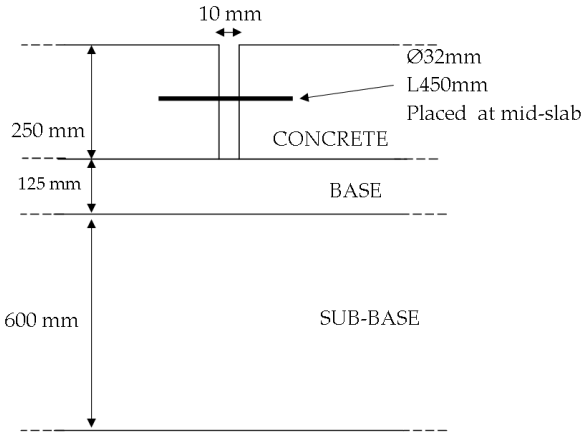

2. A-A section

Figure 3.1: Modelled pavement

3.3 Material Properties

3.3.1 Dowel Bar

The steel dowel was modeled using an isotropic linear elastic material. Table 3.1 summarizes the material characteristics of the dowel.

Table 3.1: Elastic and physical parameters for the dowels

Parameter	Value
Modulus of elasticity E_s	200,000 MPa
Poisson's ratio ν_s	0.3
Coefficient of linear thermal expansion α_s	$12 \times 10^{-6}/°C$
Density ρ_s	7800 kg/m^3

3.3.2 Concrete

General Parameters

The elastic and general characteristics of concrete are summarized in Table 3.2. The concrete compressive strength f_c' was chosen as 30 MPa, which is typical of a concrete pavement for use in Canada, and the modulus of elasticity approximated as $E_c = 22,500$ MPa.

Table 3.2: Elastic and physical parameters for the concrete

Parameter	Value
Modulus of elasticity E_c	22,500 MPa
Poisson's ratio ν_c	0.18
Coefficient of linear thermal expansion α_c	$11 \times 10^{-6}/°C$
Density ρ_c	2400 kg/m^3

Concrete Damaged Plasticity Model

The concrete was modeled using the concrete damaged plasticity model implemented in ABAQUS [40]. This is a general concrete model, capable of handling monotonic, cyclic and dynamic loading. The main failure mechanisms used in this model are tensile cracking and compressive crushing; the model consists of the combination of non-associated multi-hardening plasticity and isotropic damaged elasticity to describe the irreversible damage that occurs during the fracturing process.

Three parameters are required to define the flow potential and the yield surface behaviour: Ψ, σ_{bc} and K_c.

Ψ is the volumetric dilation angle, that is a measure in degrees of the dilation angle in the p–q plane at high confining pressure. If σ_{ij} is the effective stress and $s_{ij} = \sigma_{ij} + p\delta_{ij}$ is the effective stress deviator, then $p = -\frac{1}{3}\sigma_{kk}$ is the hydrostatic pressure stress and $q = \sqrt{\frac{3}{2}s_{ij}s_{ij}}$ is the Mises equivalent effective stress. Indices i, j, k vary from 1 to 3, $\delta_{ij} = 1$ if $i = j$ and $\delta_{ij} = 0$ if $i \neq j$.

σ_{bc} is the biaxial compression strength ratio, defined by $\sigma_{bc} = \sigma_{b0}/\sigma_{c0}$, where σ_{b0} is the initial equibiaxial compressive yield stress and σ_{c0} is the initial uniaxial compressive yield stress.

K_c is the ratio of the second stress invariant on the tensile meridian, q_{TM}, to that on the compressive meridian, q_{CM}, at initial yield for any given value of the pressure invariant p such that the maximum principal stress is negative, $\sigma_{max} < 0$. Additional background material can be found in the ABAQUS manual and the report by Buch et al. [5, 40]. The values of the three parameters are taken as the default recommended values in the ABAQUS manual [40].

Table 3.3: Parameters for the concrete damaged plasticity model

Parameter	Value
Volumetric dilation angle Ψ	15°
Biaxial compression strength ratio σ_{bc}	1.16
Ratio of tensile-to-compressive meridian K_c	0.667

The evolution of the yield surface is controlled by two hardening variables, ϵ_t^{pl} and ϵ_c^{pl} which are defined as the equivalent tensile (PEEQT) and compressive strains (PEEQ) related to the failure mechanisms in tension and compression respectively. PEEQT and PEEQ values at a given material point relate to the uniaxial inelastic stress-strain behaviour of the material, and are converted from the inelastic strains resolved in the multi-axial plastic strain tensor. These two variables will be used to establish damage criteria.

Compressive Behaviour

The model assumes that the uniaxial tensile and compressive response of concrete is characterized by damaged plasticity. Under uniaxial compression the response is linear until the value of initial yield, σ_{c0}. In the plastic regime the response is typically characterized by stress hardening followed by strain softening beyond the ultimate stress, σ_{cu} (Figure 3.2). This representation, although somewhat simplified, captures the main features of the response of concrete.

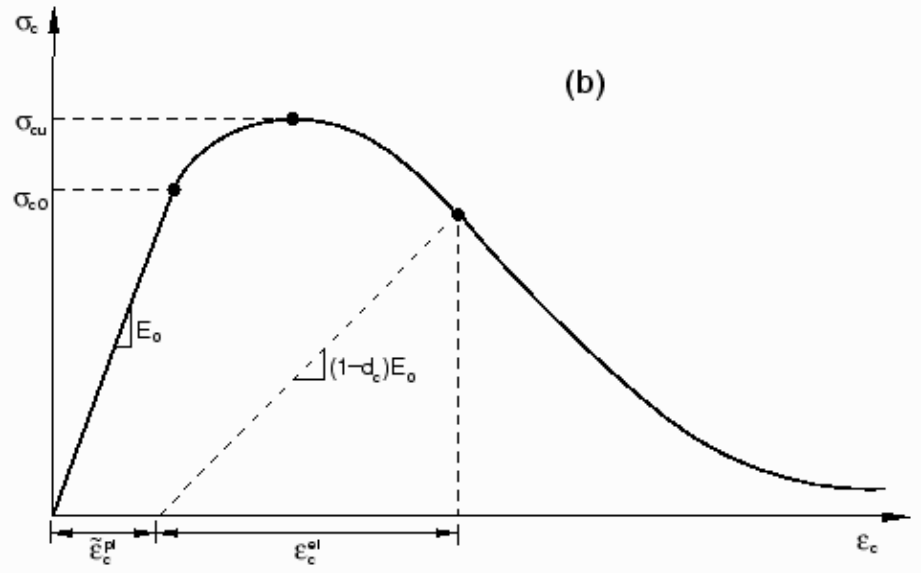

Figure 3.2: Response of concrete to uniaxial loading in compression (ABAQUS Manual [40])

The compression stress-strain formulation retained for this analysis is the one proposed by Collins, which is adequate for normal strength concrete [41]. The stress-strain relationship is expressed as follows:

$$\frac{\sigma_c}{f'_c} = \frac{n\eta}{n-1+\eta^{k\cdot n}} \tag{3.1}$$

with

$$\eta = \epsilon_c/\epsilon_{c1}$$

$$\epsilon_{c1} = 0.7(f'_c)^{0.31} = 0.002 \text{ for } f'_c = 30 \text{ MPa}$$

$$n = 0.8 + f'_c/17$$

$$k = \begin{cases} 1 & \text{for } \epsilon_c \leq \epsilon_{c1} \\ 0.7 + f_c'/20 & \text{for } \epsilon_c \geq \epsilon_{c1} \end{cases}$$

Tensile Behaviour

Under uniaxial tension the stress-strain response follows a linear elastic relationship until the value of the failure stress, σ_{t0}, is reached (Figure 3.3). The failure stress corresponds to the onset of micro-cracking in the concrete material. Beyond the failure stress the formation of microcracks is represented macroscopically with a softening stress-strain response, which induces strain localization in the concrete structure.

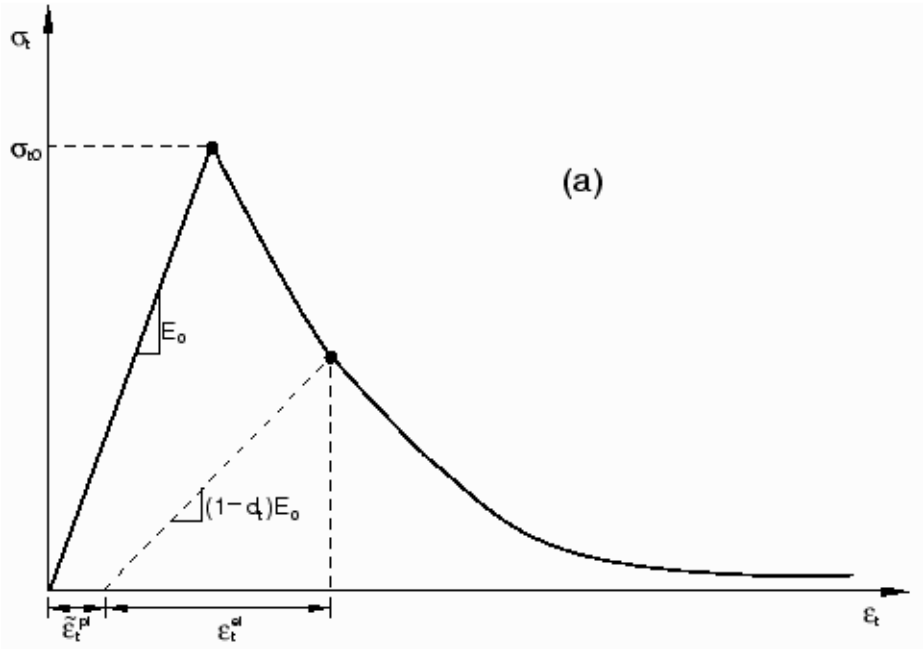

Figure 3.3: Response of concrete to uniaxial loading in tension (ABAQUS Manual [40])

However, for unreinforced concrete, the use of the fracture energy model defined by Hillerborg (1976) is more convenient because it allays a concern of unreasonable mesh sensitivity of the results. Hillerborg defines the energy required to open a unit area of crack, G_F, as a material parameter, using brittle fracture concepts. With this approach the brittle behaviour of concrete is characterized by a stress-displacement response rather

than a stress-strain response. The post-failure stress-fracture energy curve, represented on Figure 3.4, shows that when complete loss of strength takes place, the corresponding cracking displacement is $u_{t0} = 2G_F/\sigma_{t0}$.

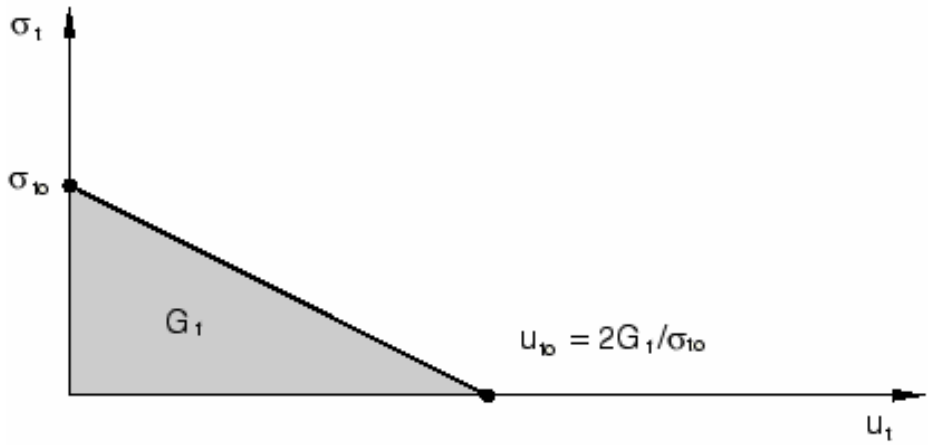

Figure 3.4: Postfailure stress-displacement energy curve (ABAQUS Manual [40])

To derive an adequate value for the fracture energy of concrete, we will use the formulation made by FIB [42], which showed that fracture energy depends primarily on concrete strength and aggregate size. FIB compared various formulations for an estimation of the fracture energy based on compressive strength and aggregate size. Equation 3.2 provides the best fit for the experimental data according to FIB:

$$G_F = G_{F0}\left(1 - 0.77 \cdot \frac{f'_{c0}}{f'_c}\right) \tag{3.2}$$

In Equation 3.2 G_F is the fracture energy in N/mm, f'_c is the concrete compressive strength, $G_{F0} = 0.18$ N/mm is the base value of fracture energy which would correspond to a concrete compressive strength $f'_{c0} = 10$ MPa. For 30 MPa concrete we obtain $G_F = 0.1338$ N/mm. A study on highway concrete by Jensen and Hansen [43] confirms that the order of magnitude for fracture energy ranges from 0.080 to 0.160 N/mm depending on aggregate size and type. The tensile strength of concrete $\sigma_{t0} = f'_t$ is taken equal to that derived by FIB [42]:

$$\sigma_{t0} = f'_t = 2.12\ln(1 + \frac{f'_c}{10}) \approx 3 \text{ MPa} \tag{3.3}$$

Damage in concrete is represented by a weakened loading/unloading stress-stress relationship. Reduction of the modulus of elasticity is accounted for using a degradation parameter, d, as

$$E = (1 - d)E_0$$

where E_0 is the initial (undamaged) modulus of the material. This expression is used for both the tensile and compressive sides of the cycle. The stiffness degradation parameter, d, is defined as a function of strain or displacement. Damage parameters in compression and tension are taken from sample values in the ABAQUS verification manual [40]. These values are commonly used in papers using concrete models in ABAQUS. A sensitivity analysis on this parameter is included in the present study (Chapter 4).

The degradation parameter in compression is defined as a function of inelastic (crushing) strain. The degradation parameter in tension was not included at first but was used for the sensitivity analysis.

Table 3.4: Concrete damage parameters in compression

Compression damage parameter d_c	Inelastic strain
0.0000	0.0000
0.1299	0.0004
0.2429	0.0008
0.3412	0.0012
0.4267	0.0016
0.5012	0.0020
0.5660	0.0024
0.7140	0.0036
0.8243	0.0050
0.9691	0.0100

Uniaxial cyclic behaviour is determined by weight factors w_c and w_t, which control the recovery of the tensile and compressive stiffness upon load reversal (see Figure 3.5). The experimental observation in most quasi-brittle materials, including concrete, is that the

compressive stiffness is recovered upon crack closure as the load changes from tension to compression. On the other hand, the tensile stiffness is not recovered as the load changes from compression to tension once crushing micro-cracks have developed. This behaviour, which corresponds to $w_t = 0$ and $w_c = 1$, is the default used by ABAQUS, and is the one used in this study.

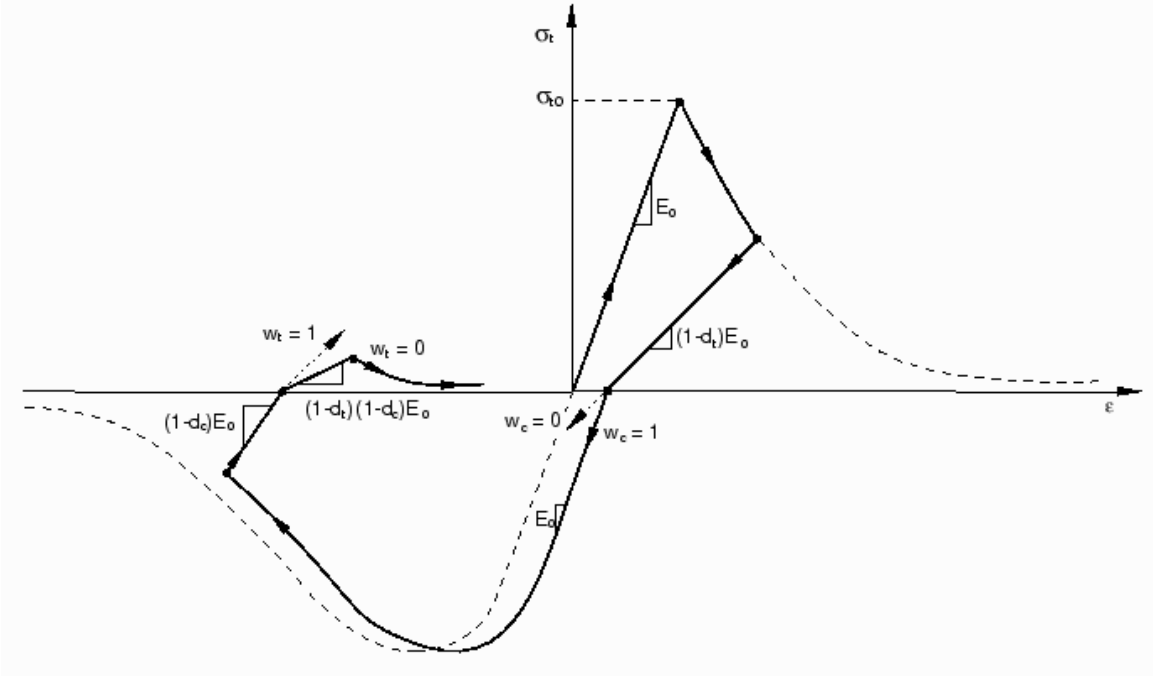

Figure 3.5: Uniaxial load cycle (tension-compression-tension) assuming default values for the stiffness recovery factors w_c and w_t [40]

3.3.3 Base and Subbase

The base and subbase are modeled as isotropic elastic materials. The material properties used are taken from Buch et al. [5].

Table 3.5: Base and subbase properties

	Parameter	Value
Base = OGDL	Modulus of elasticity	207 MPa
	Poisson's ratio	0.3
	Density	2100 kg/m^3
Subbase	Modulus of elasticity	103 MPa
	Poisson's ratio	0.3
	Density	2100 kg/m^3

3.4 Interfaces

3.4.1 Interaction Between Pavement Layers

For the current analysis, the following assumptions are regarding the interaction between pavement layers:

1. The bottom of the subbase layer is fully constrained. No spring foundation was added because the bottom of the subbase is far enough from the surface layers and no significant vertical response is expected from the model.

2. Tied contact constraint is provided between the base and the subbase.

3. Slab-base friction is provided based on the Lee model, discussed in the previous chapter [37]. The Lee model uses a correction factor to account for the type of base and transient or steady-state response. All calculations carried out, the following values for slab-base friction parameters are obtained for a granular base (no effect of slab thickness) and used subsequently in the current study.

$$\begin{aligned} \mu_{max} &= 0.965 \\ PD &= 0.0187 \text{ in} = 0.475 \text{ mm} \end{aligned} \tag{3.4}$$

where:

μ_{max} is the friction coefficient between the slab and the base

PD is the preliminary displacement which occurs before sliding due to elasticity between slab and base

3.4.2 Dowel-Concrete Contact Modelling

Summary of Previous Analytical Approaches

Experimental studies have shown that there is initial contact pressure between the dowel and the PCC [4, 23]; otherwise concrete would not show any resistance to the horizontal movement of perfectly aligned dowel bars, which contradicts the experimental results and common construction practice (use of bond breaking agent on one half of the bar).

Khazanovich et al. explained these initial stresses as a possible result of several factors [4]:

- PCC layer compaction
- Dowel resistance to PCC shrinkage contraction
- Mechanical bond between the PCC and the dowel
- Chemical adhesion

Khazanovich et al. presented three possibilities to model initial contact pressure [4]:

- Direct assignment of the external compressive forces at the dowel–PCC interface
- Assignment of negative change of PCC temperature
- Assignment of positive change of dowel temperature

The last option was retained by Khazanovich et al. as being more convenient to model than the second option and more numerically stable than the first one. A modified Coulomb friction model (Figure 3.6) was used with a friction coefficient of 0.3 and a shear stress limit of 2.1 MPa (300 psi) as it was found that it matched the experimental results.

Shoukry et al. [23] evaluated the friction coefficient μ between the concrete and the dowel from laboratory tests knowing the normal or clamping force F_{clamp} and the frictional or pulling force F_{pull} with the equation:

$$\mu = \frac{F_{pull}}{F_{clamp}} \tag{3.5}$$

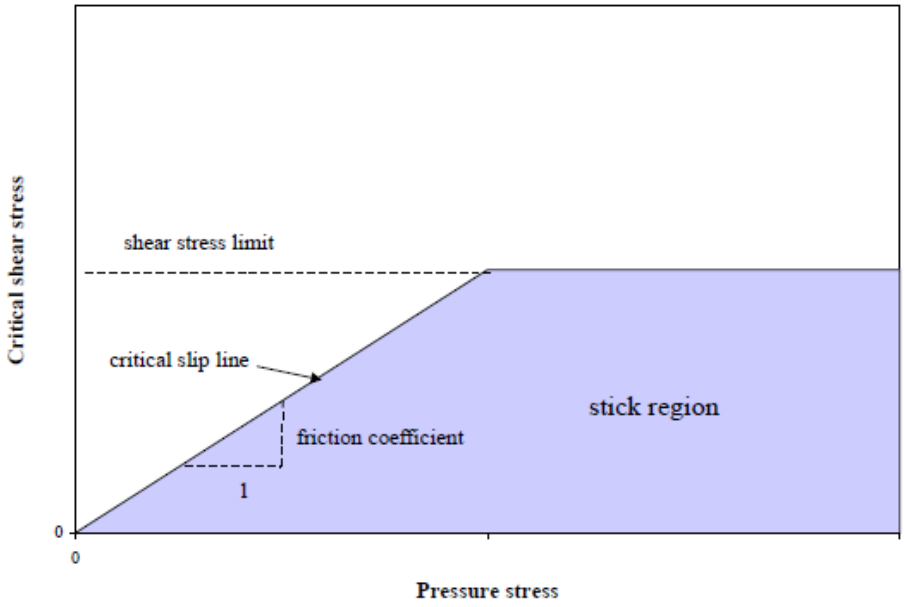

Figure 3.6: Modified Coulomb model [4]

The friction coefficients obtained from the analysis of clamping forces are reproduced in Table 3.6.

Table 3.6: Friction coefficient for 32 mm diameter dowel bar

Uncoated	0.383736
Silicon coated	0.092568
Tectyl coated	0.076293

To model dowel-concrete contact in the 3D-FEM models, Shoukry et al. [23] selected a sliding surface with a voids-type interface to account for voids at the dowel-concrete surface; the values for the friction coefficient were taken based on the bond-breaking agent applied on the dowel. The shrinkage of concrete was taken into account by defining a temperature drop throughout the concrete block. For the model with twelve dowel bars, the concrete slab underwent a temperature gradient of -10 °C (-18 °F) accompanied with a -33.3 °C (-60 °F) decrease in its mean temperature.

Buch et al. [5] modeled the contact between the steel and the concrete using two models:

- The first model focused on the longitudinal bond between the steel and concrete due to irregularities on the dowel surface and static friction. Spring elements were used and calibrated with the experimental results of pullout tests.
- The second model focused on the transverse interaction between the steel dowel and surrounding concrete resulting in large contact or bearing stresses and additional friction bond in the longitudinal direction due to the normal (bearing) stresses and Coulomb friction coefficients. For this purpose, special surface-to-surface elements were used to model hard contact behaviour with Coulomb friction. The friction coefficients for the idealized case were taken as 0.0 and 0.3 for the greased and ungreased sides of the dowels, respectively, and 0.076 and 0.384 for the case with measured parameters.

To activate the Coulomb friction model, Buch et al. [5] applied a gravity load to generate the appropriate contact forces and simulate the experimental behaviour of the tested specimens.

Contact Parameters Selection

In the current analysis, contact between the dowel and the surrounding concrete is modelled as follows, based on the review of existing models:

1. Steel-concrete contact is modelled as a hard contact with a modified friction Coulomb model and no separation between the surfaces.
2. The different friction coefficients were taken as 0.076 for the greased side and 0.384 for the uncoated side of the dowel based on the work of Shoukry et al. [23], with a shear stress limit of 2.1 MPa.
3. No longitudinal bond due to chemical or mechanical adhesion was considered in this analysis since it may be expected that this bond will break during the first thermal load cycle.

3.5 Loading

3.5.1 Shrinkage Load

As was mentioned previously, shrinkage is an important contributor to slab movements. It is therefore necessary to include it for a realistic physical modelling of the joint behaviour. Shrinkage of concrete is modelled by an application of a strain profile across the depth of the slab. The review of several models and experimental data shows that the shrinkage strain profiles at a given time are highly nonlinear, and consists of two parts: a constant, low strain at the bottom half of the slab, and an exponential increase of strain from mid-depth to the slab surface. Kim and Lee [27] showed that at any given time, a drastic reduction in shrinkage occurred below a concrete depth of 120 mm. The maximum shrinkage strain in the experimental study by Kim was about 350 microstrains with creep considered. We can note here that this is less than the lower end of the range recommended by ACI-209 [44] for ultimate shrinkage strain of 415 microstrains, and approximately half of the ultimate shrinkage strain for standard conditions, 780 microstrains. Altoubat and Lange [45] managed to separate creep strains from shrinkage strains in an experimental slab set-up. It was observed that the ratio of creep strain over shrinkage strain ($\epsilon_{creep}/\epsilon_{shrinkage}$) was approximately 0.5 to 0.6; since creep strains reduce shrinkage strains, this means that the total strain in the concrete (creep strains plus shrinkage strains) is 50% that of shrinkage strain alone. This confirms the findings made by Kim and Lee [27] concerning strain reduction due to creep. In the rest of this study, we will refer to combined shrinkage and creep strains simply as shrinkage strain, assuming creep strains have been included in the calculation.

For the current analysis, an ultimate shrinkage strain of 400 microstrains was assumed as representative of typical shrinkage strain occurring in normal concrete, based on the literature review discussed in the previous paragraph. To implement shrinkage in the model, it was considered that the center of the slab (far from the dowels) was submitted

to unrestrained shrinkage in the vertical direction; a shrinkage profile depending only on slab height was implemented in ABAQUS using an equivalent temperature distribution. Low shrinkage strains were assigned to the lower half of the concrete slab, and an exponential strain profile is used. Total shrinkage strain can be represented by Equation 3.6, similar to the function used by Kim and Lee [27] in Equation 2.6. A third parameter was added in the equation because it allows to modify the shape of the profile more easily, if ever it was needed to calibrate the shrinkage strain profile.

$$\epsilon_{sh}(y) = a + b \cdot e^{\lambda y} \tag{3.6}$$

where ϵ_{sh} is strain expressed in microstrains, y is slab height in mm and t is time in days. The conditions were initially assumed for ultimate strains to fit with the shrinkage strain profile derived by Kim and Lee [27]. No adjustments were necessary since there was good agreement between the deflections of the joint calculated by ABAQUS and joint deflections found in the literature (Chapter 5). Figure 3.7 represents the ultimate shrinkage profile as well as the shrinkage profiles at different times based on ACI-209 [44]; one can observe that the profile after 1 year is almost identical to the ultimate profile.

$$\epsilon_{sh,u}(y = 250) = 400$$

$$\epsilon_{sh,u}(y = 125) = 37.5$$

$$\epsilon_{sh,u}(y = 0) = 25$$

By fitting the three parameters a, b and λ from Equation 3.6 to the three values of shrinkage strain above, it comes: $a = 24.55$, $b = 0.4465$ and $\lambda = 0.0269$.

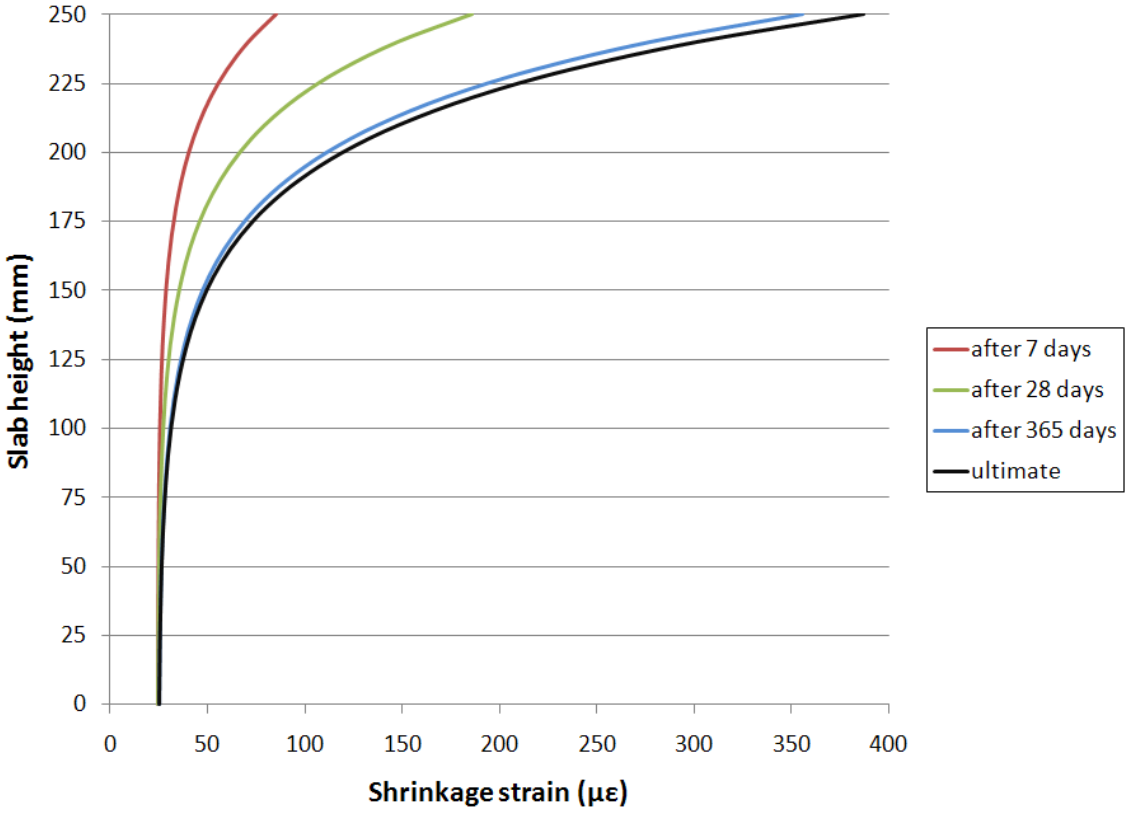

Figure 3.7: Variation of shrinkage strain profile across slab depth

In order to simulate the shrinkage strains in the 3D-FEM model, they are treated as thermal strains. Using the relation $\epsilon_{sh,u} = \alpha_c \times \Delta T_{sh,u}$, where $\epsilon_{sh,u}$ is the ultimate shrinkage strain, α_c the coefficient of thermal expansion of concrete and $\Delta T_{sh,u}$ the equivalent temperature variation, the shrinkage strain profile can be converted to a temperature profile (Equation 3.7).

$$T_{sh}(y,t) = (A + B \cdot e^{\lambda y}) \tag{3.7}$$

with $A = -2.232$, $B = -0.04059$, $\lambda = 0.0269$. The ultimate equivalent temperature gradient between slab top and bottom is then $\Delta(T) = -34.1°C$, which represents ultimate shrinkage strain condition.

3.5.2 Thermal Load

Temperature loading was also considered in the current analysis since thermal changes account for the daily variations in joint deflections (Chapter 2). Cyclic thermal loads were implemented in ABAQUS by imposing thermal strains to the slab, and added to the shrinkage strain.

A review of the literature was done in search of typical temperature profiles. Shoukry et al. [46] observed that the temperature profile as a function of the depth of the slab could be expressed as a parabolic function represented in Equation 3.8.

$$T_{temp}(y) = A + By + Cy^2 \tag{3.8}$$

Several studies have observed that the variation of pavement temperature between the top and the bottom of the slab ranged between 0 and plus or minus 10°C [36, 39, 46]. The study by Jeong and Zollinger [39] developed realistic temperature profiles for daytime and nighttime. In the study, the temperature at different heights in a 305 mm thick slab was recorded for the several days after casting of the slabs period. The measured temperature profile are presented in Figure 3.8. Note that the current study is not interested in absolute temperature values but rather the relative change in temperature undergone by each concrete fibre. As such, the data in Figure 3.8 are plotted relative to an initial zero temperature profile assumed to occur at time 10am. The maximum positive curling occurs at 5pm, and the maximum negative curling occurs at 6am.

Two temperature profiles are implemented in the current study, one for the daytime, T_{day} (Equation 3.9), and one for the nighttime, T_{night} (Equation 3.10). The daytime temperature is taken as the thermal profile at 5pm, while nighttime temperature is taken as the profile at 6am (Figure 3.8). The values of A, B and C in Equation 3.8 are calculated by fitting the quadratic curve with the top, bottom and midslab points. The calculated temperature profiles are represented in Figure 3.9.

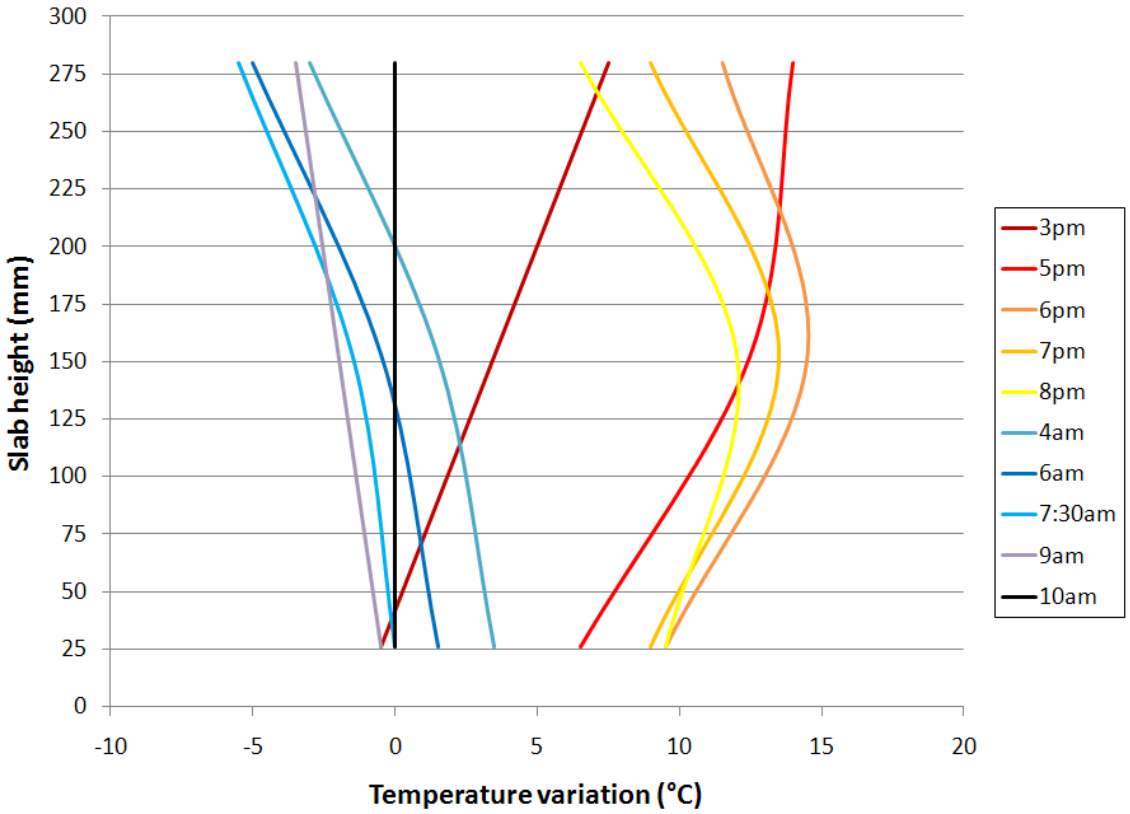

Figure 3.8: Temperature profiles in the slab, adapted from Jeong and Zollinger [39]

$$T_{day}(y = 250) = 14°\text{C}$$

$$T_{day}(y = 125) = 12°\text{C}$$

$$T_{day}(y = 0) = 5°\text{C}$$

$$T_{day}(y) = 5 + 0.076y - 1.6 \times 10^{-4} y^2 \tag{3.9}$$

$$T_{night}(y = 250) = -6°\text{C}$$

$$T_{night}(y = 125) = 0°\text{C}$$

$$T_{night}(y = 0) = 2°\text{C}$$

$$T_{night}(y) = 2 - 1.28 \times 10^{-4} y^2 \tag{3.10}$$

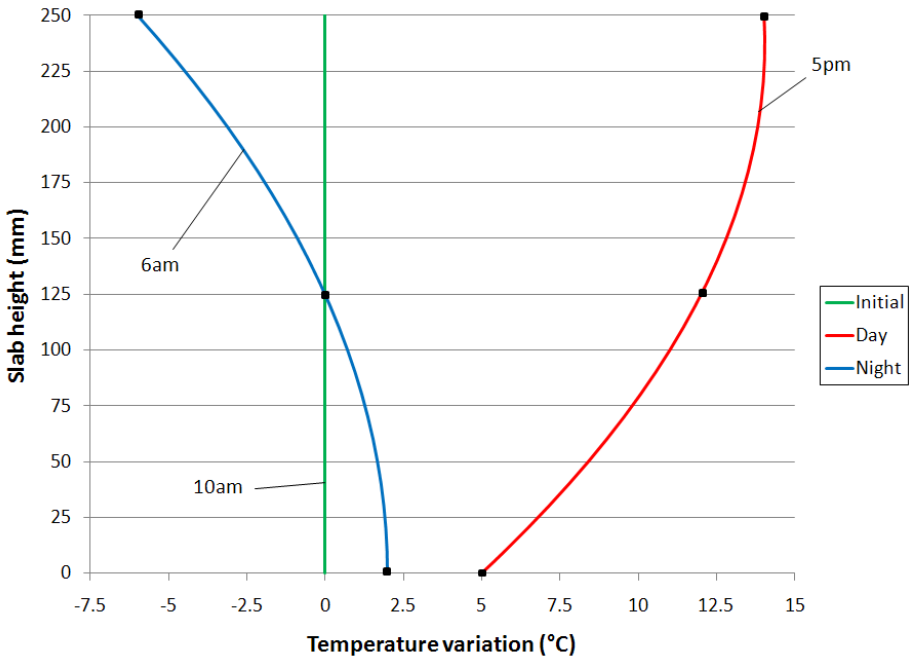

Figure 3.9: Temperature profiles implemented in ABAQUS in current study

3.5.3 Implementation in ABAQUS

The environmental loading function was implemented in two successive steps:

- Application of shrinkage to the concrete in a single step.
- Two temperature cycles applied to the concrete and the steel; two cycles were found to lead to an almost steady strain state.

The overall loading history is represented in Figure 5.1 in terms of strain applied to the concrete top fibre. The shapes of the strain profiles (relative to slab depth) are represented schematically for each of the steps.

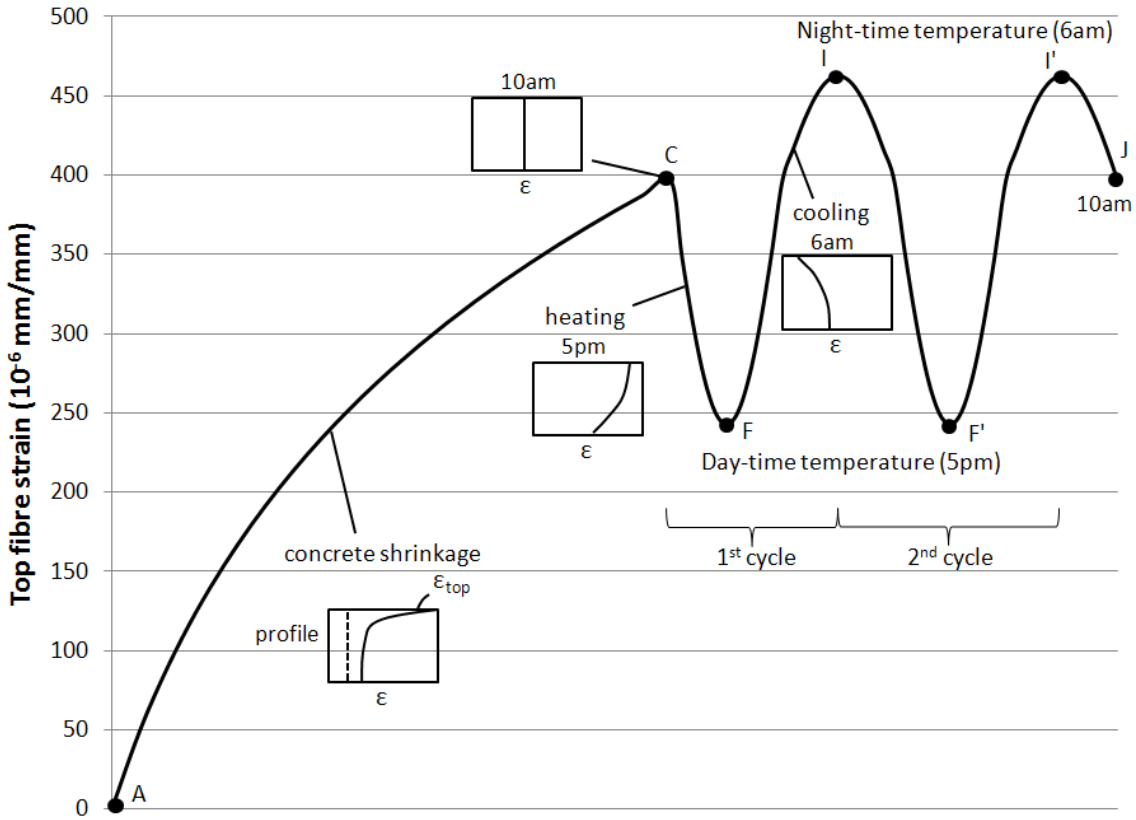

Figure 3.10: Loading history in terms of strain applied to the concrete top fibre

3.6 Summary

The 3D numerical modelling of a dowel jointed concrete pavement in ABAQUS has been presented, and the geometries for a single-bar model and a multi-bar model were described. The material properties for the dowel bars, the base and subbase were detailed, along with the non-linear damaged plasticity model for concrete. The interactions between the dowel bars and the concrete, and between the slab and the base, were modelled using modified Coulomb friction models. Finally, the choice of loading for shrinkage and temperature was exposed, and the subsequent strain profiles applied to the pavement were derived.

Chapter 4

Single Bar Model Development

4.1 Mesh and Boundary Conditions

The geometry for this model consists of a singe dowel bar embedded in a strip of concrete slab. The width of the strip was taken as the centre-to-centre distance between adjacent dowel bars. All other geometry and parameters are as described in Chapter 3. For symmetry considerations, only half of the bar and the concrete is modeled (Figures 4.1 and 4.2). The boundary conditions were chosen so as to simulate a central dowel bar: the transverse plane of symmetry is fixed in the tranverse direction x (rollers) while the east and west planes of symmetry are fixed in the longitudinal direction z (rollers). The bottom of the model is fully constrained as specified in the previous chapter.

The elements used for the model are eight node reduced integration elements (C3D8R) available in ABAQUS library; these elements are versatile and capable of being subjected to large deformations. Because this is a single bar model with a vertical plane of symmetry, only vertical misalignment configurations were analysed.

A mesh refinement study was carried out to ensure that the output obtained from the models was not an artefact of the chosen mesh size. Three different mesh configurations were experimented for the modelling of the concrete slab (Table 4.1). A model with 50 mm

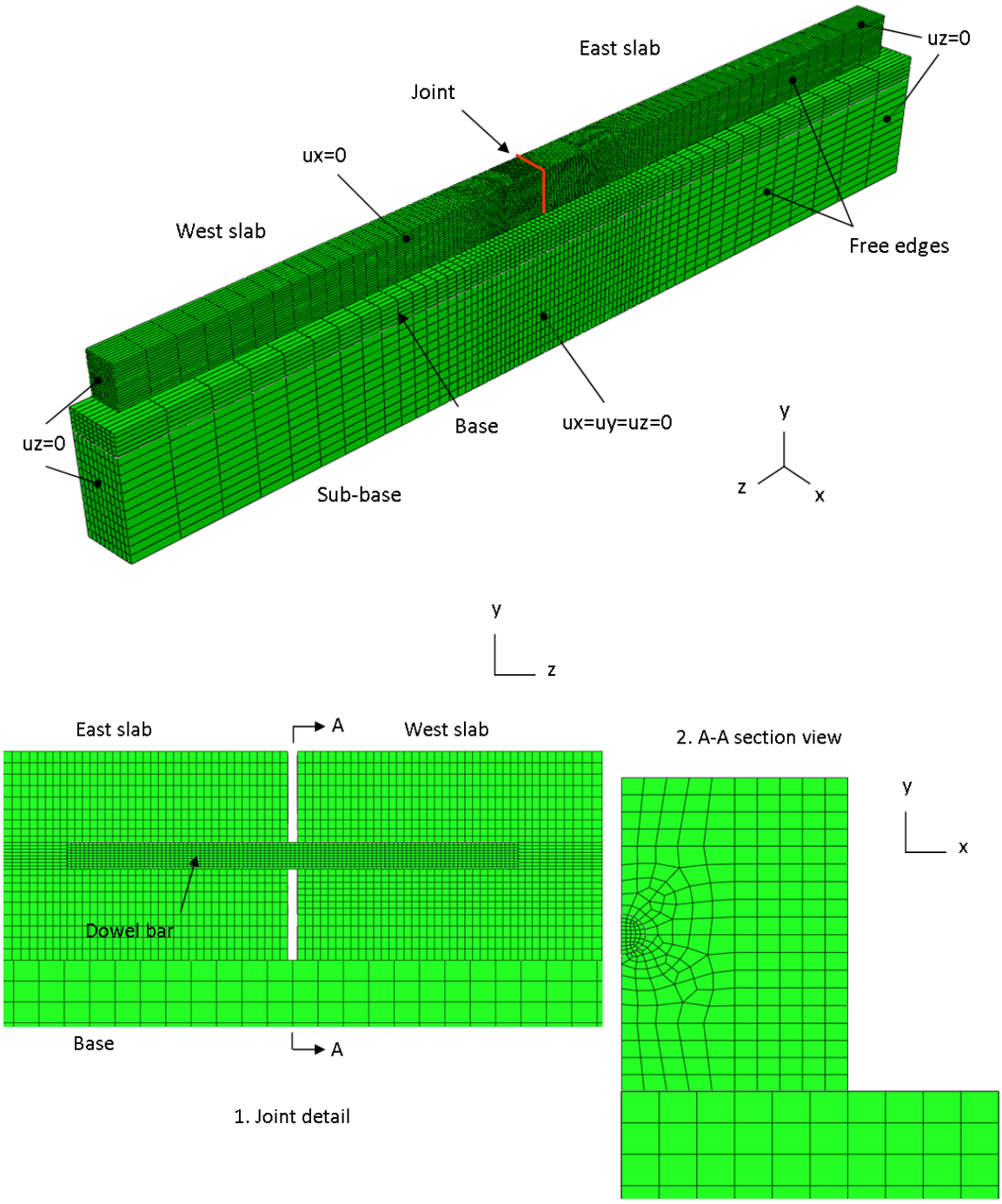

Figure 4.2: Mesh detail of dowel bar and joint

of angular misalignment (1V50) was chosen for this verification (Figure 2.4 shows the definition for vertical misalignment).

Table 4.1: Mesh characteristics for the 1V50 model

Mesh size	Number of slab elements (one slab)	Total number of elements[a]
Mesh I (Coarse)	8897	33391
Mesh II (Intermediate)	12604	41356
Mesh III (Refined)	19190	54904

[a]Includes slabs, dowel, base and subbase

Mesh refinement considerations are based on computing efficiency and precision. A single shrinkage step was applied to the concrete slab with a vertically misaligned bar (by 50 mm). The following characteristic parameters were compared to determine an adequate refinement of the mesh:

- Joint opening and vertical displacement
- Bar axial force
- Principal stress distribution

The bar axial force is estimated as the total frictional force acting at the concrete/dowel interface, in the direction of the bar axis. It can also be estimated using the axial strain in the dowel bar. Table 4.2 summarizes the results obtained for the three tested meshes. The difference in displacements and force are insignificant between Mesh II and Mesh III (less than 1 %). Figure 4.3 shows the variation of bar axial force as a function of joint opening.

Table 4.2: Effect of mesh refinement on various parameters

Mesh	Joint horizontal displacement	Joint vertical displacement	Bar axial force
Mesh I (Coarse)	0.689 mm	1.16 mm	6.68 kN
Mesh II (Intermediate)	0.683 mm	1.15 mm	8.40 kN
Mesh III (Refined)	0.683 mm	1.15 mm	8.41 kN

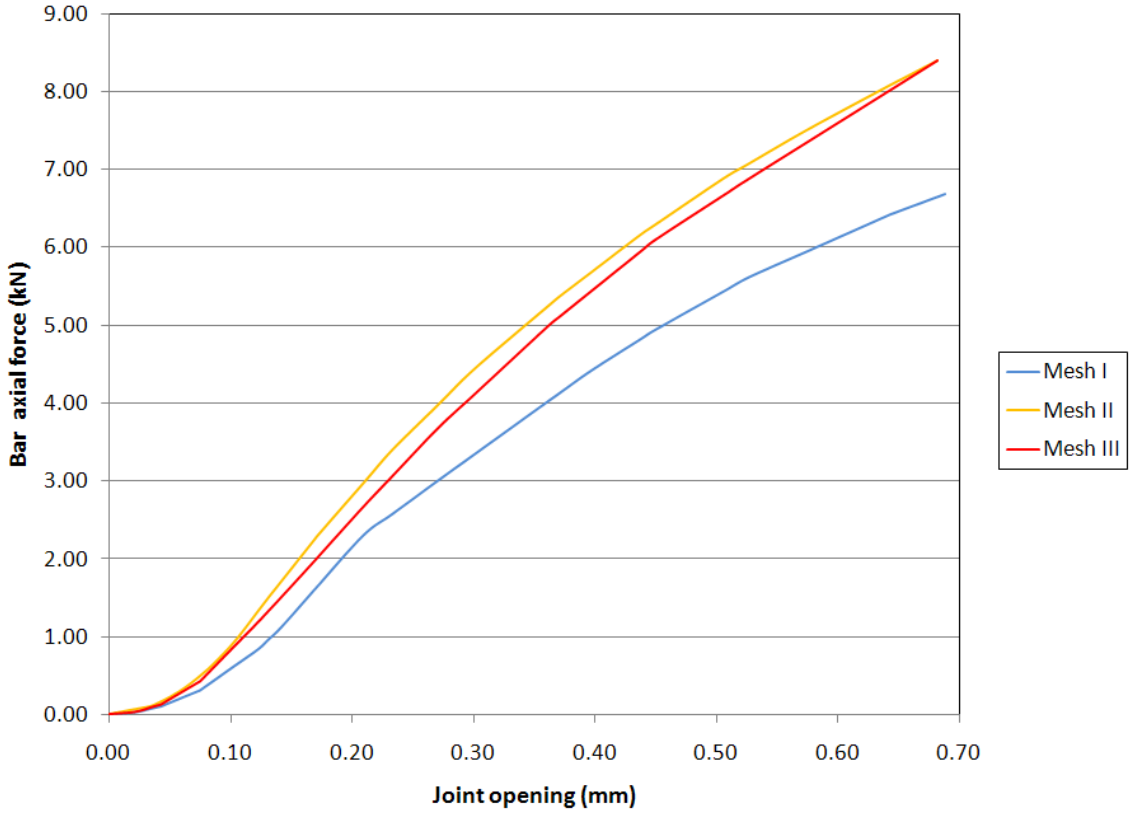

Figure 4.3: Comparison of axial force between the meshes

The distribution of the principal stresses in the concrete is fairly similar for all meshes as can be seen in Figures 4.4 and 4.5. The concrete maximum tensile stress of 3 MPa develops in the same manner for all three meshes. Maximum tensile stress is reached at the top of the slab as a result of shrinkage-induced slab bending, and at the steel/concrete interface close to the joint due to combined bending and joint opening. Figure 4.6 shows that the magnitude of tensile principal stresses around the dowel bar at the joint is very close except at the zero degree position (bottom of the bar). This discrepancy can probably be attributed to local sensitivity of the calculations to the mesh shape. However the maximum stresses are located approximately at the same place (90°). Given the similarity in results obtained from Meshes II and III, Mesh II was selected for the analysis of the single bar model.

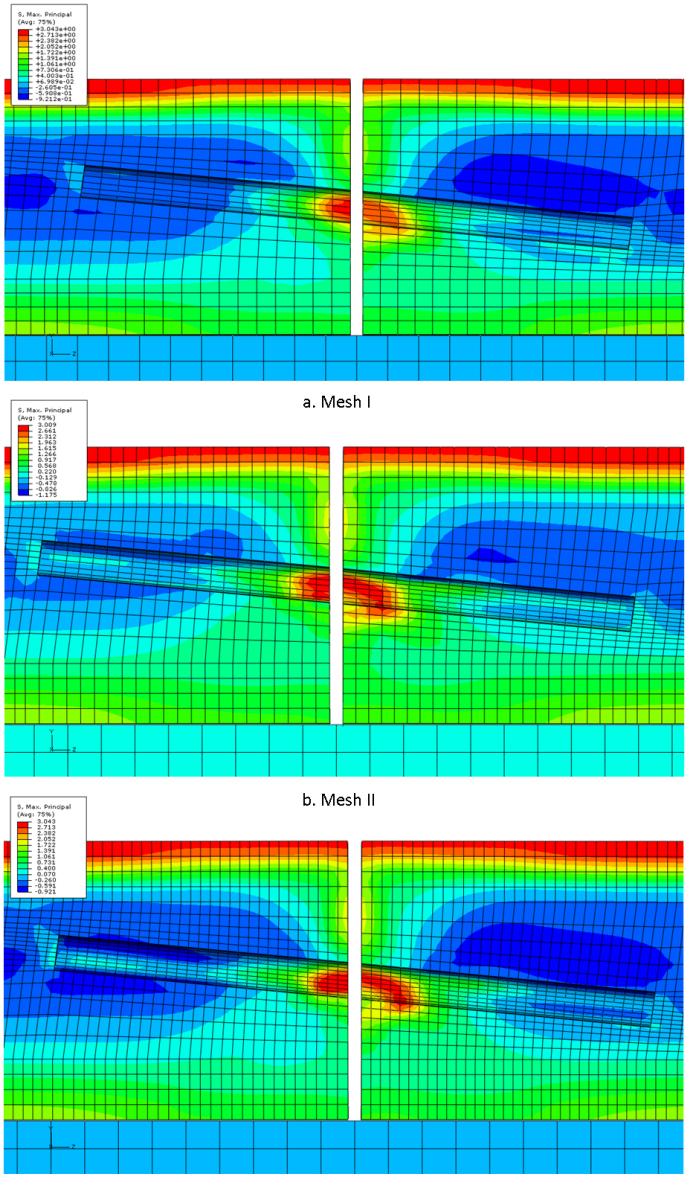

a. Mesh I

b. Mesh II

c. Mesh III

Figure 4.4: Maximum principal stresses in the yz plane

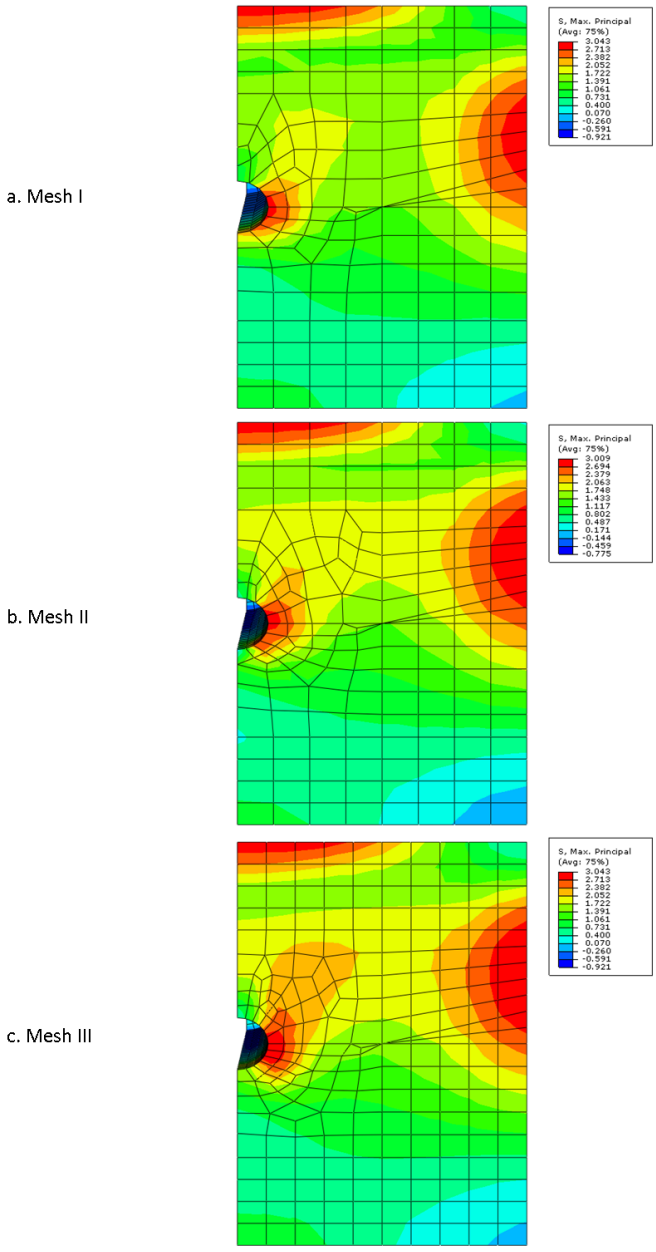

Figure 4.5: Maximum principal stresses in the xy plane

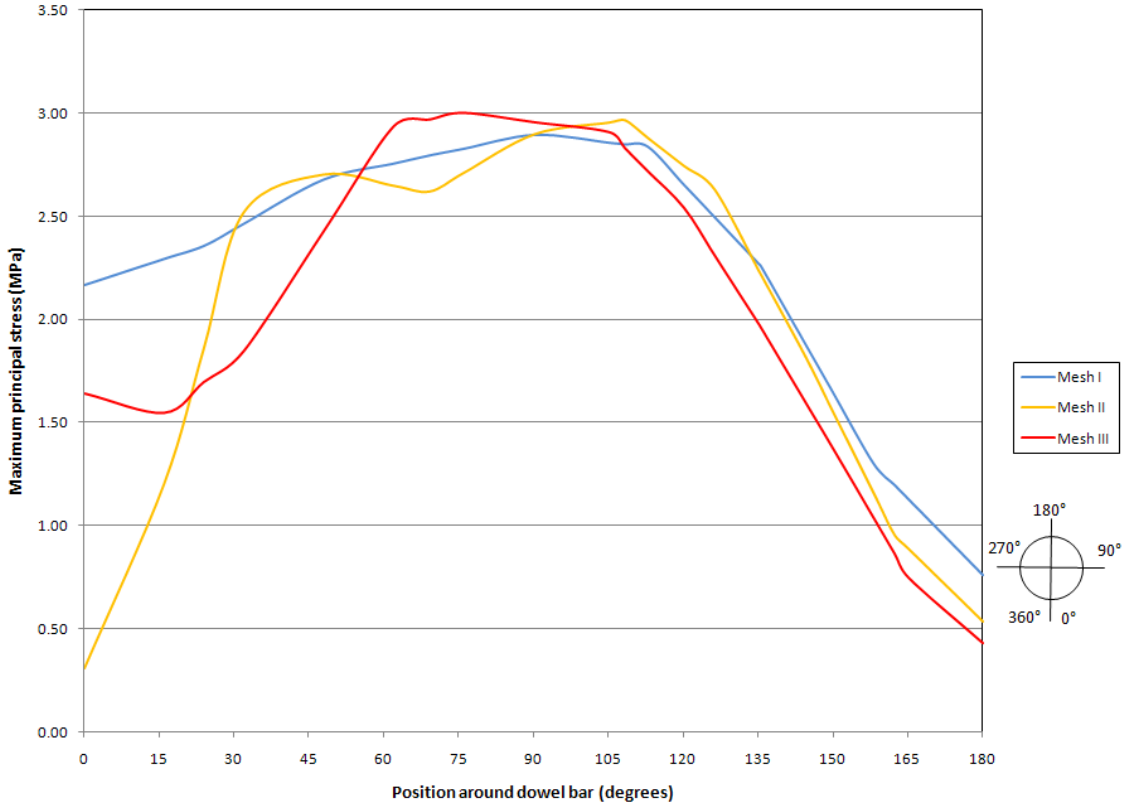

Figure 4.6: Maximum principal stresses around the dowel bar at the joint

4.2 Sensitivity Analysis

A sensitivity analysis was completed on several model parameters to study the sensitivity of the results to the choice of input parameters (coming from ABAQUS manuals or published literature). This allows the robustness of the modelling to be investigated, in particular with regards to parameters that exhibit great variability in the literature. The main objective is to study the outcome on the results of the choice of parameters within a realistic range of values.

4.2.1 Effect of Concrete Model Parameters

Effect of Fracture Energy

The effect of the concrete fracture energy parameter on the pavement behaviour was examined for the pavement subjected to a single shrinkage step ($\epsilon_{sh,u} = 400\ \mu\epsilon$). Jensen [43] observed that the fracture energy for highway concrete ranged from 0.080 to 0.160 N/mm; in the current analysis, a broader range of 0.040 N/mm to 0.200 N/mm was selected. The results, summarized in 4.3, show that the differences between joint displacements and bar axial forces are very small (less than 4 %). Therefore, for the chosen range of values for the fracture energy and the type of modelling done, the deflections and output forces are expected to stay constant. This suggests that as long as the concrete pavement does not experience the formation of large plastic zones (plastic strains remain highly localized), the effect of fracture energy does not have a strong outcome on the results.

Table 4.3: Effect of fracture energy (shrinkage only)

Fracture energy (N/mm)	Joint horizontal displacement	Joint vertical displacement	Bar axial force
0.040	0.675 mm	1.140 mm	12.72 kN
0.080	0.683 mm	1.174 mm	12.78 kN
0.1338	0.685 mm	1.180 mm	12.84 kN
0.200	0.686 mm	1.183 mm	12.80 kN

Effect of Damage Parameters

The influence of the concrete degradation parameters on the pavement behaviour was evaluated for a pavement subjected to a shrinkage strain of 400 $\mu\epsilon$. The damage parameter in tension is taken from the ABAQUS manual as a linear function of cracking strain as listed in Table 4.4. The damage parameter in compression is taken as described in Chapter 3. Results shown in Table 4.5 indicate that the effect of including the parameters is insignificant for a slab submitted only to shrinkage. This suggests that the zones of plasticity in tension and compression, remaining limited in volume, the damage parameters (weakened unloading

curve) do not have a strong effect on the global outcomes of the model.

Table 4.4: Tension damage parameter

Tension damage parameter d_t	Cracking displacement (mm)
0	0
0.9	$2\frac{G_F}{f_t'} = 0.0892$

Table 4.5: Effect of damage parameters (shrinkage only)

Damage selection	Joint horizontal displacement	Joint vertical displacement	Bar axial force
No compression damage, no tension damage	0.685 mm	1.180 mm	12.78 kN
Compression damage, no tension damage	0.685 mm	1.180 mm	12.84 kN
Compression damage, tension damage	0.685 mm	1.181 mm	12.79 kN

The influence of the recovery parameters in compression and tension was evaluated for a concrete pavement subjected to two different loading cases: a single shrinkage step and five temperature cycles. The temperature load used for that purpose were different than those used for the complete loading scenario described in Chapter 3; temperature profiles are shown on Figure 4.7. The recovery parameters in compression and tension are expected to have a minimal influence on the concrete pavement behaviour, as long as the points of non-linearity in the concrete material remains localized. Results for the influence of compression and tension recovery parameters due to shrinkage and cyclic temperature changes are respectively listed in Tables 4.6 and 4.7 and Tables 4.8 and 4.9. Standard values for compression and tension recovery parameters are respectively 1 and 0. The results confirm that the recovery parameters have no effect on the results from the chosen loading functions.

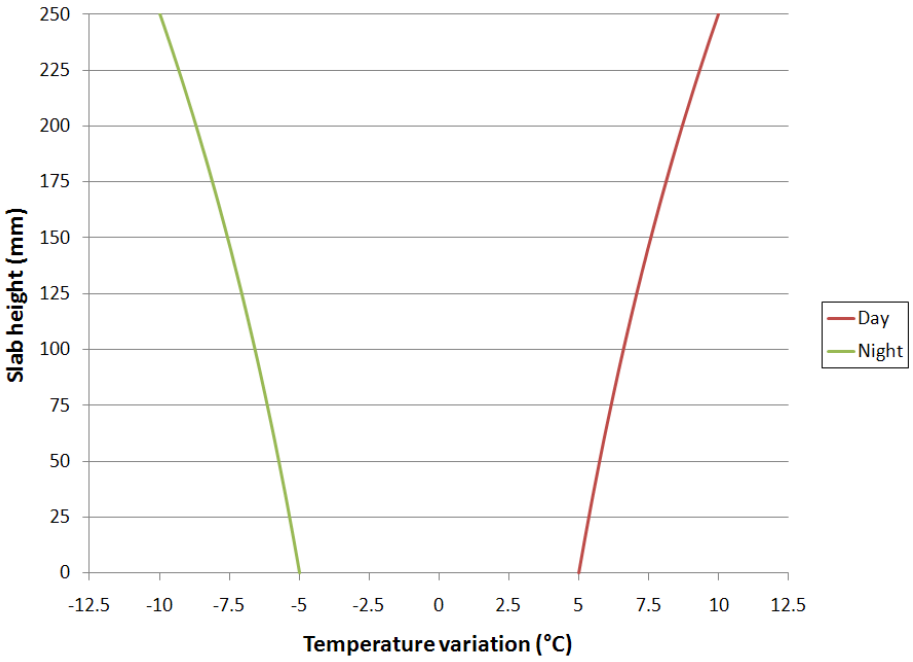

Figure 4.7: Temperature profiles for the sensitivity analysis

Table 4.6: Effect of compression recovery (shrinkage only)

Compression recovery	Joint horizontal displacement	Joint vertical displacement	Bar axial force
0	0.685 mm	1.180 mm	12.79 kN
0.5	0.685 mm	1.180 mm	12.79 kN
0.9	0.685 mm	1.181 mm	12.79 kN
1	0.685 mm	1.181 mm	12.84 kN

Table 4.7: Effect of tension recovery (shrinkage only)

Tension recovery	Joint horizontal displacement	Joint vertical displacement	Bar axial force
0	0.685 mm	1.180 mm	12.84 kN
0.1	0.685 mm	1.180 mm	12.79 kN
0.5	0.685 mm	1.181 mm	12.80 kN
1	0.685 mm	1.181 mm	12.80 kN

Table 4.8: Effect of compression recovery (cyclic temperature changes)

Compression recovery	Day joint deflection	Night joint deflection	Day bar force	Night bar force
0	-0.1 mm	0.05 mm	-36.4 kN	-12.5 kN
0.5	-0.1 mm	0.05 mm	-36.7 kN	-12.5 kN
1	-0.1 mm	0.05 mm	-36.4 kN	-12.5 kN

Table 4.9: Effect of tension recovery (cyclic temperature changes)

Tension recovery	Day joint deflection	Night joint deflection	Day bar force	Night bar force
0	-0.1 mm	0.05 mm	-36.4 kN	-12.5 kN
0.5	-0.1 mm	0.05 mm	-36.4 kN	-12.5 kN
1	-0.1 mm	0.05 mm	-36.6 kN	-12.5 kN

4.2.2 Effect of Slab-Base Friction

Different values were investigated for the coefficient of friction between the slab and the underlying base. This parameter was found to have no effect on the final results (Table 4.10). This makes sense since the contraction or expansion of the slab is accompanied by upward or downward deflection; hence slab-base contact is lost at the location where the greatest displacements occur.

Table 4.10: Effect of friction coefficient (shrinkage only)

Friction coefficient	Joint horizontal displacement	Joint vertical displacement	Bar axial force
0	0.685 mm	1.180 mm	12.79 kN
0.3	0.685 mm	1.180 mm	12.79 kN
0.6	0.685 mm	1.180 mm	12.79 kN
0.965	0.685 mm	1.180 mm	12.84 kN

4.2.3 Conclusion

The sensitivity analysis performed on the model showed little variance in the results obtained, mostly due to the fact that the stresses remain highly localized in the model. The model predictions can be considered robust for the parameters chosen, since the concrete model

parameters do not have a strong effect on the outcome of the different analyses performed. It is however necessary to include the parameters since most of them are required in the ABAQUS damaged plasticity model for concrete. Not specifying any value or variation law for a parameter comes down to assuming the default values for the parameter, since these values is required for the concrete model computations.

4.3 Summary

A single dowel bar model was developed in this chapter. The boundary conditions, the meshing technique and the mesh refinement considerations were detailed. A sensitivity analysis was performed to study the influence on the finite element model results of the parameters of the concrete damaged plasticity: fracture energy, damage parameters and recovery parameters, along with the effect of slab-base friction.

Chapter 5

Single Bar Model Results

5.1 Introduction

A parametric study was carried out on the single bar model, developed in the previous chapter to evaluate the influence of the following parameters on the slab behaviour:

- Angular misalignment of the dowel bar in a vertical plane: 0 mm (standard), 20 mm, 30 mm and 60 mm were used (see Figure 2.4 3.).
- Vertical displacement of the dowel bar: 0 mm and +25 mm (upward) were used (Figure 2.4 5.). 25 mm of vertical displacement corresponds to the limit of acceptability for dowel placement by MTO; more cases were run at this level of misplacement since it is expected to be more detrimental to joint performance.
- Dowel-concrete friction coefficient (use of bond breaker): the standard case is a friction coefficient of 0.384 (uncoated); coated bar has a friction coefficient of 0.076. Additionnally one case was run with one half of the bar coated and the other half uncoated, and a slightly corroded bar was simulated by doubling the friction coefficient of the standard case to 0.768.
- Concrete coefficient of thermal expansion: $11 \times 10^{-6}/°C$ (standard) and $8 \times 10^{-6}/°C$

were used.

- Concrete compressive strength: 30 MPa (standard) and 50 MPa were tested.

Table 5.1 summarizes the different variables used in the parametric study for the single bar model. The standard or control case is considered to be a non-misaligned, uncoated bar embedded in a concrete having coefficient of thermal expansion of $11 \times 10^{-6}/°C$ and a compressive strength of 30 MPa.

Table 5.1: Summary of parameters for the single bar model

Model ID	Angular misalignment (vertical)	Vertical displacement	Coating properties	Coefficient of thermal expansion	Concrete strength
1V0-Unc	0	0	Uncoated	11×10^{-6}	30 MPa
1V60-Unc	60 mm	0	Uncoated	11×10^{-6}	30 MPa
1V0-C	0	0	Coated	11×10^{-6}	30 MPa
1V0-Unc-α8	0	0	Uncoated	8×10^{-6}	30 MPa
1V0-D25-Unc	0	25 mm	Uncoated	11×10^{-6}	30 MPa
1V20-D25-Unc	20 mm	25 mm	Uncoated	11×10^{-6}	30 MPa
1V20-D25-C	20 mm	25 mm	Coated	11×10^{-6}	30 MPa
1V20-D25-Ceast	20 mm	25 mm	Coated east side, uncoated west side	11×10^{-6}	30 MPa
1V20-D25-Cwest	20 mm	25 mm	Coated west side, uncoated east side	11×10^{-6}	30 MPa
1V20-D25-Corr	20 mm	25 mm	Corroded	11×10^{-6}	30 MPa
1V20-D25-Unc-α8	20 mm	25 mm	Uncoated	8×10^{-6}	30 MPa
1V20-D25-Unc-50MPa	20 mm	25 mm	Uncoated	11×10^{-6}	50 MPa
1V30-D25-Unc	30 mm	25 mm	Uncoated	11×10^{-6}	30 MPa
1V60-D25-Unc	60 mm	25 mm	Uncoated	11×10^{-6}	30 MPa
1V60-D25-C	60 mm	25 mm	Coated	11×10^{-6}	30 MPa
1V60-D25-Corr	60 mm	25 mm	Corroded	11×10^{-6}	30 MPa
1V60-D25-Unc-α8	60 mm	25 mm	Uncoated	8×10^{-6}	30 MPa
1V60-D25-Unc-50MPa	60 mm	25 mm	Uncoated	11×10^{-6}	50 MPa

5.2 Results of 3D-FEM Models

In this section, the overall behaviour of the modelled pavement under shrinkage and thermal loads is examined for two different models: the straight bar, non-misaligned model 1V0-Unc, and the misaligned bar model 1V20-D25-Unc. The methods used to estimate pavement damage or loss of performance are presented. We will first discuss the implication of the variables on local events and possible damage to the concrete, then analyze the consequences in terms of performance of the pavement with two different measures of joint load transfer efficiency.

5.2.1 Overall Model Behaviour

Model 1V0-Unc

The behaviour of the slab-dowel system is dominated by two main actions: vertical (curling) and axial strains. The vertical component caused by slab curling induces potential damage at the dowel/concrete interface at the joint vicinity, while damage associated with the axial component is dictated by dowel/concrete friction and end bearing between the dowel and the concrete. Hence, the overall behaviour is illustrated using graphs of bar axial force as a function of joint opening, and bar bending moment as a function of joint uplift. The loading history is illustrated in terms of the strain applied to the top fibre of the concrete slab as a function of time (Figure 5.1). This load history represents concrete shrinkage and two temperature cycles (heating/cooling). The loading history is applied following application of the gravity load to the slab-dowel system.

The succession of events occurring in the pavement is illustrated on graphs of the bar axial force and bending moment as a function of joint uplift and joint opening respectively (Figures 5.2 and 5.3). The axial force and bending moment are estimated using the strains in the dowel and the characteristics of the dowel bar section; the final result is multiplied by two to account for the force or moment in the whole dowel bar since only half of the bar is

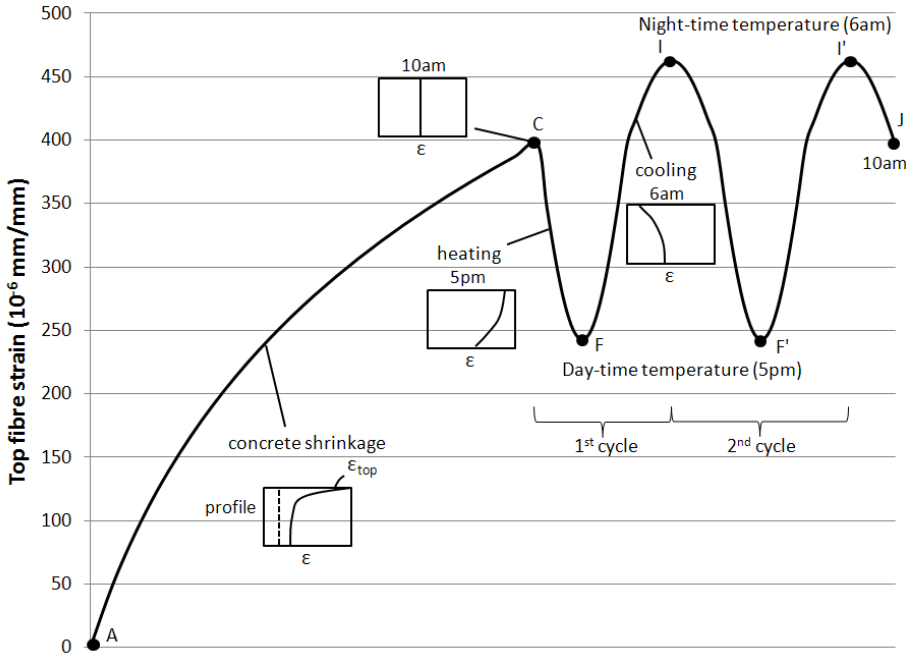

Figure 5.1: Loading history in terms of strain applied to the concrete top fibre being modelled (Equations 5.1 and 5.2).

$$F = \frac{\epsilon_b + \epsilon_t}{2} \cdot EA \times 2 \tag{5.1}$$

$$M = \frac{\epsilon_b - \epsilon_t}{2c} \cdot EI \times 2 \tag{5.2}$$

where:

F is the axial force in the dowel bar

M is the bending moment in the dowel bar

$c = 0.016$ m is the radius of the dowel bar

$A = \pi\frac{c^2}{2} = 4.02 \times 10^{-4}$ m^2 is the area of the half-section

$E = 200$ GPa is the modulus of elasticity of steel

$I = \frac{1}{8}\pi c^4 = 2.574 \times 10^{-8}$ m^4 is the second moment of area of the half-section

ϵ_b is the strain at the bottom of the bar

ϵ_t is the strain at the top of the bar

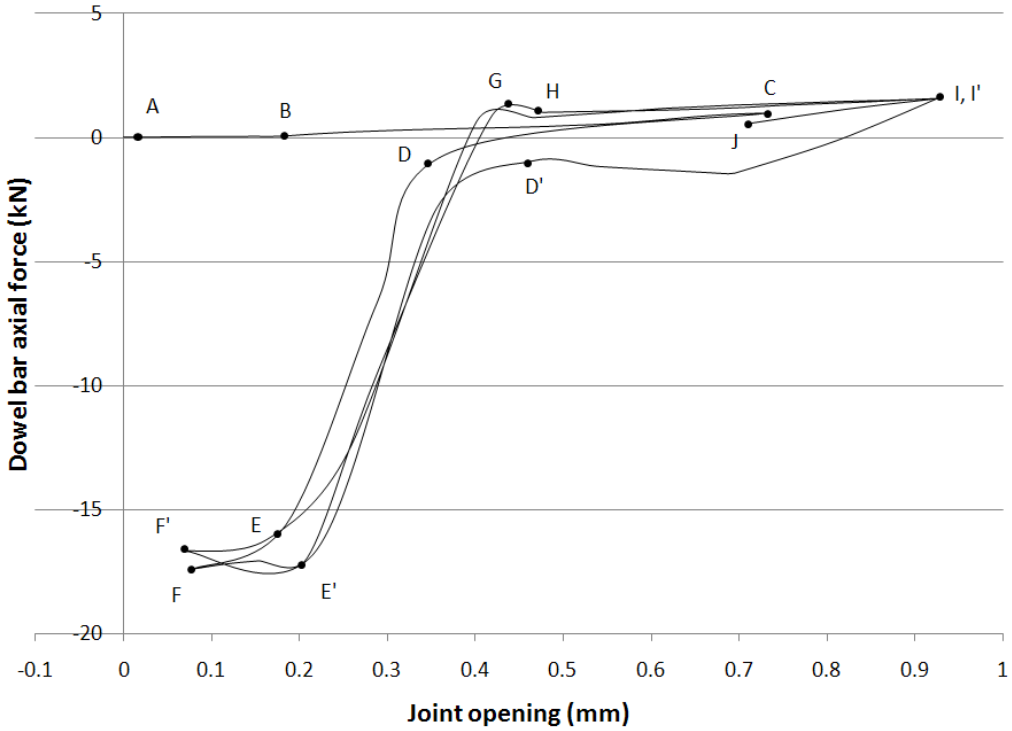

Figure 5.2: Bar force vs. joint opening for model 1V0-Unc

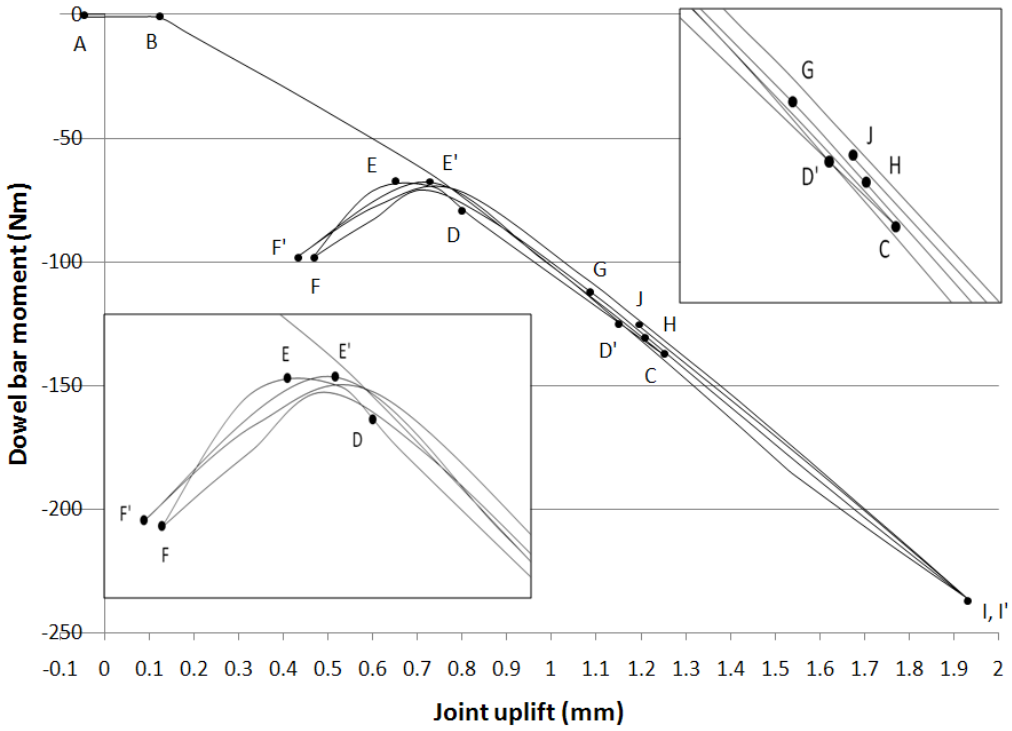

Figure 5.3: Bar moment vs. joint uplift for model 1V0-Unc

After the initial application of a gravity load, the following events take place:

1. Points A to C correspond to the initial shrinkage step, which causes upward curling of the slabs and joint uplift. The initial part (A to B) indicates that the shrinkage overcomes the strains caused by the gravity load on the slabs and dowel. From B to C, a linear relationship can be observed between bar moment and average joint uplift, and between bar force and joint opening. The shrinkage step causes the bar to bend and be pulled out of its pocket, as illustrated in Figure 5.4(1).

2. From C to F, daytime temperature (heating) is applied to the slabs and the dowel. From C to D, the application of daytime temperature tends to curl the slabs downward and push the dowel back into the pocket. Concrete-bar friction is the only action that takes place from C to D. At point D, the end of the bar is making contact with the concrete at the end of the pocket, causing the concrete to deform elastically (from D to E). This situation is represented in Figure 5.4(2). The contact between the concrete and the dowel bar happens before the slab returns to its undeformed state for two reasons: first, both the dowel bar and the concrete are heated in this step while in the previous step shrinkage was applied only to concrete; secondly, concrete and steel have approximately the same coefficient of thermal expansion. At point E, the magnitude of the strains in the concrete near the end of the pocket causes it to deform inelastically in compression and in tension. This is indicated by the development of non-zero plastic strains in compression (PEEQ) and tension (PEEQT) predicted by the 3D-FEM. The onset of inelastic behaviour coincides with sharp changes in the force-displacement plots (Figures 5.2 and 5.3) from E to F.

3. From F to I, night-time temperature profile (cooling) is applied to the pavement. During the first part (F to H) concrete elasticity is reversed while the bar is still bearing against the concrete at the end of the pocket. Moreover, upward curling of the slab induced by concrete cooling causes the bar bending moment to decrease following the same path. Point G marks the appearance of concrete inelastic plastic strains at

the joint vicinity around the dowel. At point H, the bar stops making contact with the concrete at the end of the pocket.

4. Points I through I' constitute the second temperature cycle. The path followed remains close to that of the first temperature cycle. We can observe the same events as for the first cycle. In particular, D' indicates that the bar end makes contact with the concrete at the end of the pocket, and E' reveals that the inelastic plastic strains in the concrete are further increased compared to point E.

5. From I' to J, the system slab-dowel goes back to a morning zero temperature gradient profile (with shrinkage remaining applied to the concrete). The maximum dowel bar moment reached after cooling is -236 Nm. The ultimate bar axial force is insignificant because the concrete and the dowel thermally contract at approximately the same rate.

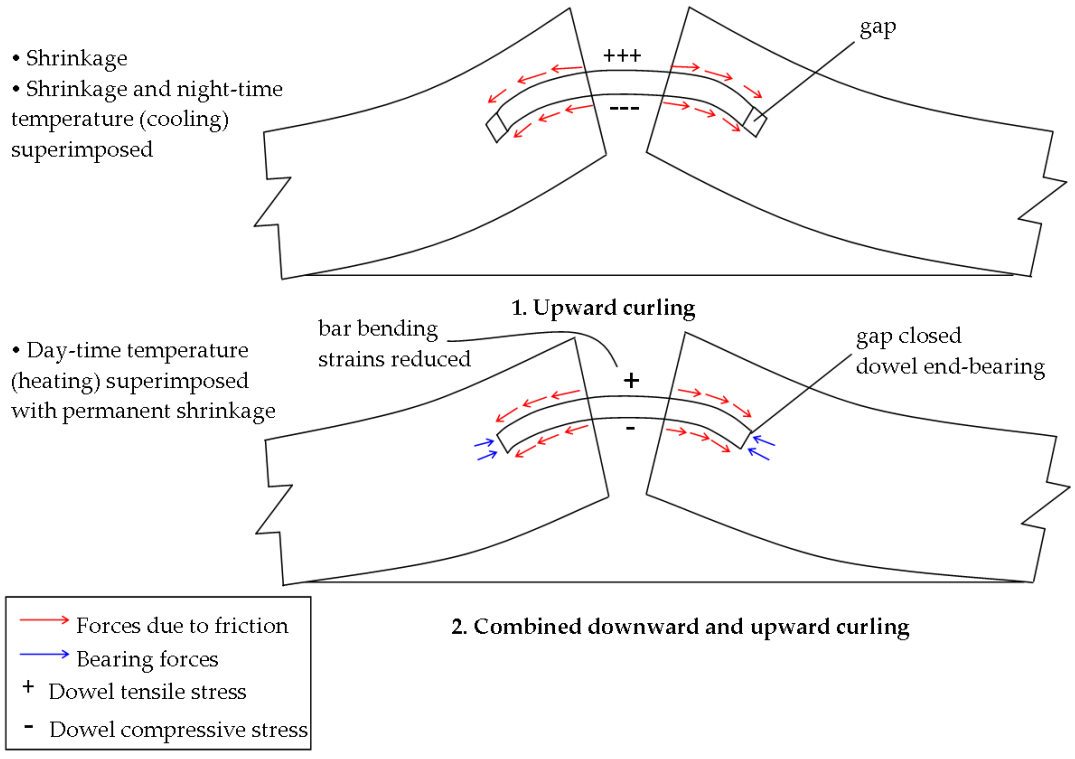

Figure 5.4: Representation of forces acting on the dowel bar during upward and downward curling

After the initial application of a gravity load, the following events take place, as illustrated on graphs of the bar moment and axial force as a function of joint uplift and joint opening (Figures 5.5 and 5.6), respectively:

1. From A to C, the shrinkage step is applied. An almost linear relationship can be observed between bar moment and average joint uplift, and between bar force and joint opening during the shrinkage step, once the effects of the initial gravity load application are reversed.

2. C to F, daytime temperature (heating) is applied. From C to D_1, the application of the first daytime temperature cycle induces the reversal of upward curling, in a linear manner. Concrete-bar friction is the only action that takes place from C to D_1; the bar bending moment stays almost constant because the bar and the surrounding concrete expand at approximately the same rate. At point D_1, only one end of the bar is making contact with the concrete at the end of the pocket, while at point D_2 the other end of the pocket also starts making contact with the concrete. This accounts for the bar axial force being constant from D_1 to D_2. From D_2 to F, the bar and concrete concurrent thermal expansion causes the concrete at the end of the pocket to compress, first elastically (D_2 to E), then inelastically (E to F).

3. From F to I, the night-time temperature profile (cooling) is applied to the pavement. The first part (F to H) is the reversal of concrete elasticity, then additional tension force to the bar is provided by the curling of the slab. Points G_1 and G_2 mark the onset of concrete plasticity around the dowel at the joint; two points are shown because the plastic strains develop at slightly different times on the east side and on the west side. The flat part from point H to I is due to the bar being pulled out of its pocket from one side only.

4. Points I through I' constitute the second temperature cycle. The path followed stays

close to the first cycle.

5. From I' to J, the system slab-dowel goes back to a morning zero temperature gradient profile (with shrinkage remaining applied to the concrete).

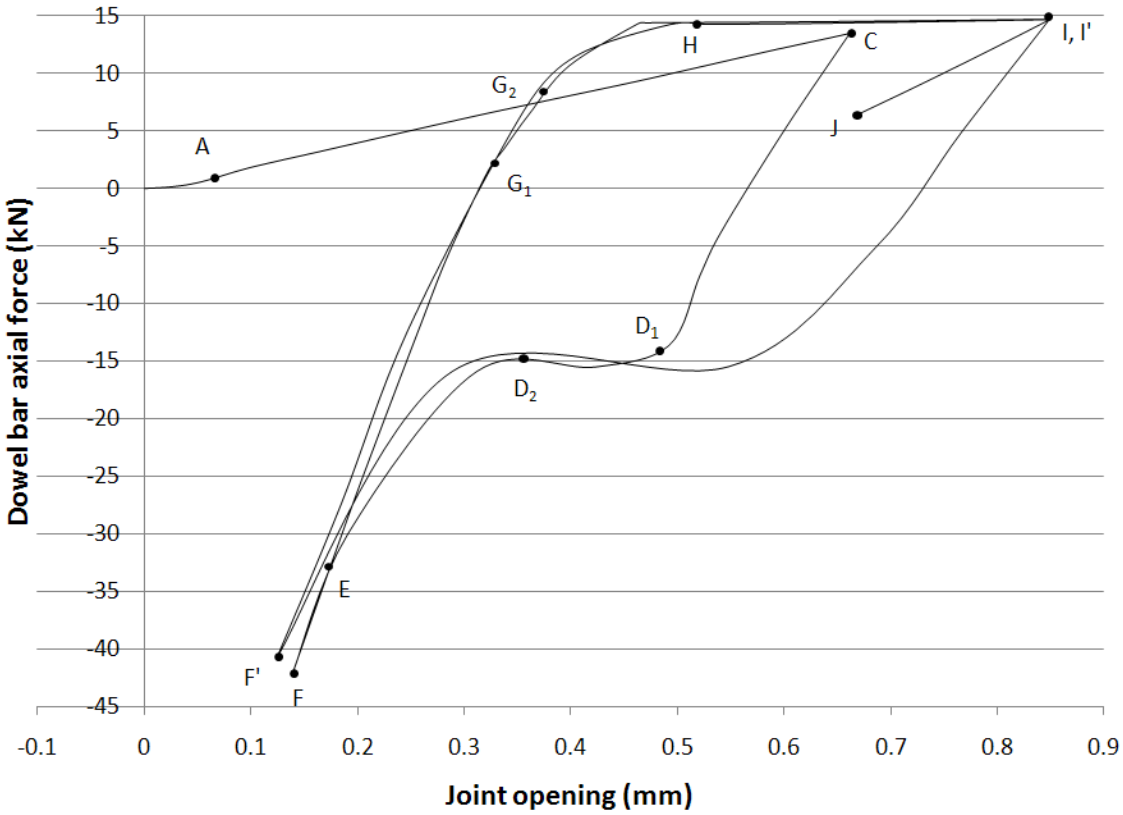

Figure 5.5: Bar axial force vs. joint opening for model 1V20-D25-Unc

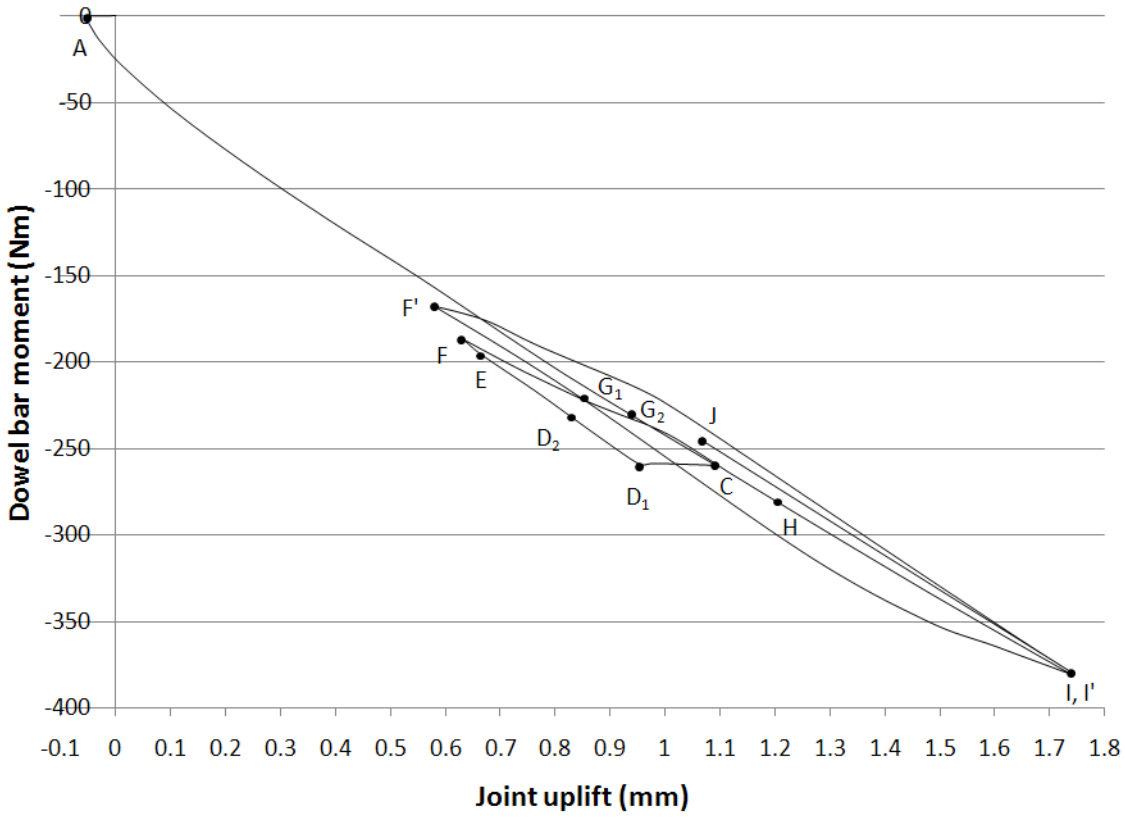

Figure 5.6: Bar bending moment vs. joint uplift for model 1V20-D25-Unc

Conclusion

It can be observed that in both models, the points corresponding to the end of the heating step (F and F'), and the points corresponding to a state where shrinkage only is applied (C and J), do not have exactly the same coordinates; this shift indicates that some plastic behaviour (damage) is occurring. The implication of the local events on the occurrence of plastic behaviour is discussed in the next section.

5.2.2 Description of Local Events

Internal Concrete Stresses Caused by the Loading Function

The 3D-FEM analysis predicts that internal stresses build up in the pavement due to internal shear induced by the shrinkage load, independently of the presence of dowel bars. This is due to the non-linear shrinkage strain profile that creates internal restraint stresses even when the slab is externally unrestrained. Figures 5.7 and 5.8 represent views of maximum principal tensile stresses and minimum principal compressive stresses in the concrete for model 1V0-Unc, respectively. Areas in red in Figure 5.7 indicate large zones where the splitting tensile strength of the concrete is reached. The high tensile stresses on top on the slab are due to the shape of the shrinkage strain profile, which as per Chapter 3, has a very steep gradient towards the surface of the pavement. Hence, shearing stresses develop in both directions of curling, longitudinal (z) and transversal (x), which explains that the higher stresses occur at the top of the slab close to the centerline and the transversal symmetry line. Yet, in a 3-dimensional stress-strain state, this situation does not necessarily imply cracking of the concrete. The maximum inelastic strains in this zone are approximately 150 $\mu\epsilon$ for equivalent inelastic plastic strain in tension (PEEQT) and 2 $\mu\epsilon$ for equivalent inelastic plastic strain in compression (PEEQ). The inelastic strain values in compression are insignificant, while the inelastic strain values in tension are of the order of magnitude of the cracking strain (133 $\mu\epsilon$) which is low.

The inelastic strains remain relatively constant regardless of the position of the bar or other modifications made to the concrete properties. These results suggest that cracking (fine crack pattern) due to surface shrinkage will occur regardless of the presence and mis-alignment of the dowel bar. These cracks may or may not appear in the field depending on the quality or the curing of the concrete.

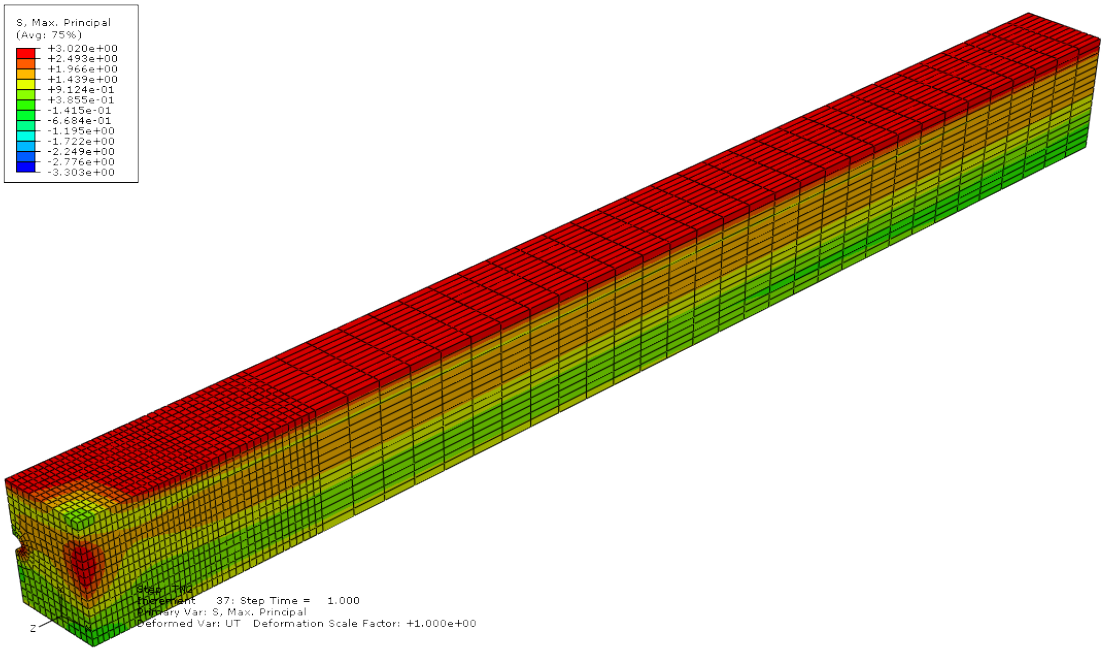

Figure 5.7: Tensile principal stresses in concrete for 1V0-Unc model

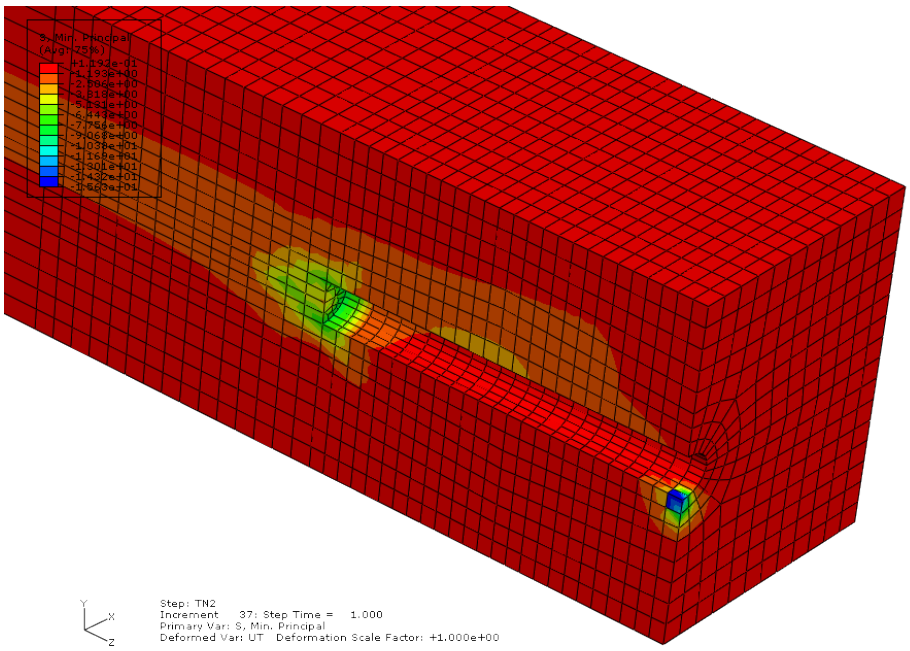

Figure 5.8: Compressive principal stresses in concrete for 1V0-Unc model

The second zone where high stresses occur is at the longitudinal free edge away from the dowel bar; those stresses are caused by the absence of restraint at this edge, and are mainly a result of the vertical stresses at this location. The distribution of tensile and compressive vertical stresses expected is shown in Figure 5.9: bearing stresses just below the dowel bar at the joint, and tensile stresses at the sides of the dowel. Those expectations are confirmed by the results obtained from ABAQUS (Figure 5.10). The plastic strains in this zone stay very low compared to the failure criteria.

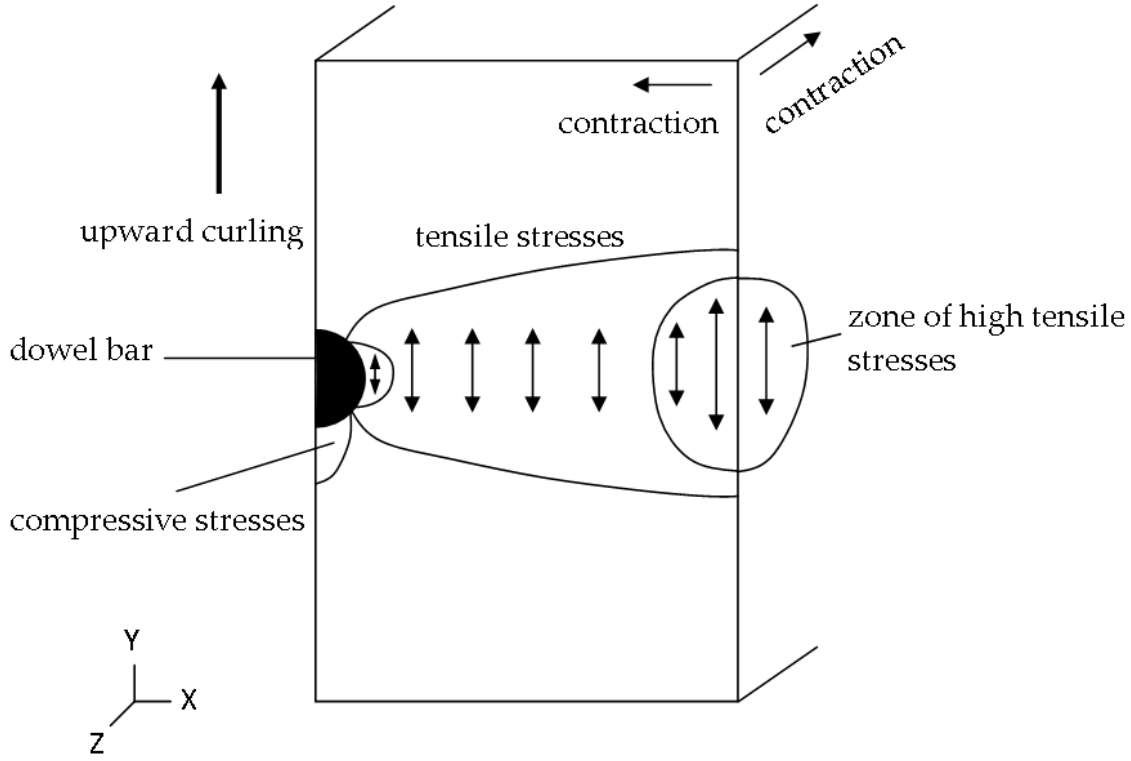

Figure 5.9: Expected tensile and compressive vertical stresses at the joint vicinity

To conclude, the strains occurring at the top surface and at the edge of the slab will not be considered as regions of interest in this analysis since they are low and fairly constant from one model to anothe. Furthermore, they do not account for the changes observed in the overall behaviour of the joint expressed either in terms of dowel bar axial force functions of joint opening or dowel bar bending moment functions of joint uplift. The latter changes are caused by the damage occurring around the dowel bar.

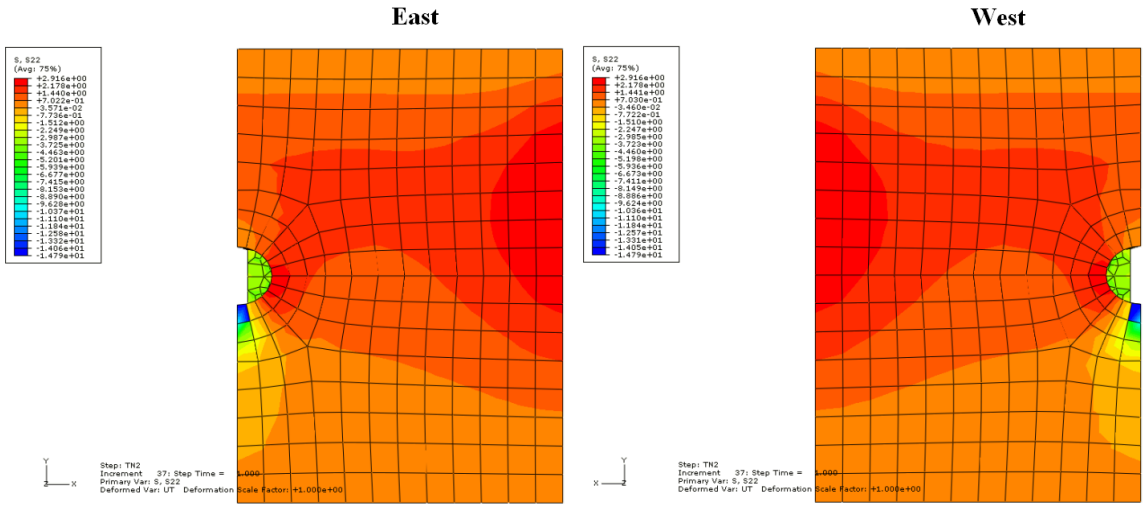

Figure 5.10: Stresses in the vertical (y) direction from ABAQUS for model 1V0-Unc

Concrete Strains Around the Dowel Bar and Damage Criteria

Strains and stresses develop in the concrete around the bar in two distinct zones: near the end of the concrete pocket and around the bar at the joint vicinity. Theses stresses are caused by the axial actions on the bar (friction, end bearing) and the bending of the bar.

In order to interpret the strains occurring around the dowel, damage criteria that have some physical relevance were developed. The two modes of failure considered in this analysis are concrete tensile cracking and compressive crushing. For concrete tensile cracking, a damage criterion is set using the equivalent plastic strain in tension, PEEQT. PEEQT represents the tensile equivalent plastic strain at the material point and is related to the uniaxial stress-strain behaviour of the material. Significant cracking is estimated to occur when the plastic strain in tension, PEEQT, exceeds approximately ten times the initial cracking strain. Since the cracking strain is $\frac{f_t'}{E_0} = \frac{3\ MPa}{22{,}500\ MPa} = 0.000133$, significant cracking would occur when PEEQT=0.00133. In a multiaxial strain state, PEEQT=0.00133 corresponds to the same magnitude of inelastic cracking strain state in uniaxial tension.

For concrete crushing, a similar criterion is established using the equivalent inelastic

plastic strain in compression, PEEQ. Significant crushing is assumed to occur when the total uniaxial strain in compression reaches 0.005. This value corresponds to PEEQ=0.00474 for a compressive strength of 30 MPa and PEEQ=0.00156 for a compressive strength of 50 MPa. The values of PEEQ are obtained based on the stress-strain response of the concrete in uniaxial compression and the unloading data provided in terms of compressive damage curves (Table 3.4).

The forces exerted by the dowel bar on the concrete at the end of the pocket cause high localized stresses and strains in the surrounding concrete. Tensile equivalent plastic strains (PEEQT) for model 1V0-Unc can be seen on Figure 5.11. These strains, though indicative of concrete significant plastification (PEEQT=0.00205), remain very localized and are not a concern for the performance of the pavement, being far from the joint. However, the modification of the concrete strain state can have repercussions on the behaviour of the concrete at the joint.

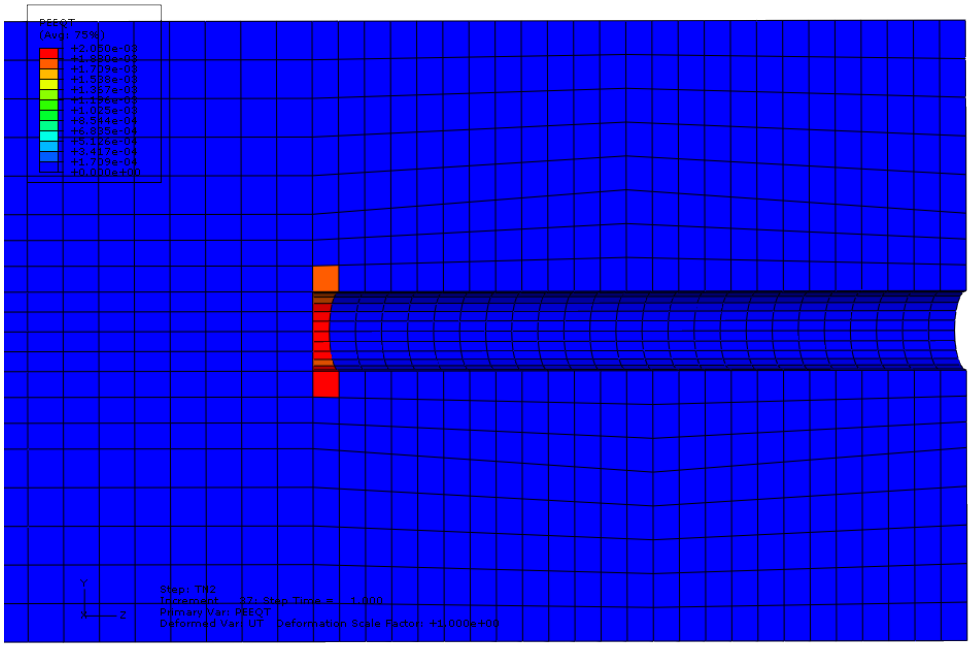

Figure 5.11: Side view of tensile plastic strains at the end of the pocket

The application of shrinkage ($\epsilon_{sh,u} = 400\mu\epsilon$) and two temperature cycles causes inelastic and cracking strains to develop around the dowel bar at the joint vicinity. Plastic strains in compression (PEEQ) and tension (PEEQT) are shown in Figures 5.12 and 5.13. For the 1V0-Unc model, they develop during the application of the first night-time temperature cycle, while for the 1V20-D25-Unc model, they develop during the shrinkage step. The final values for average peak PEEQ and PEEQT are 274 $\mu\epsilon$ and 223 $\mu\epsilon$ respectively for the 1V0-Unc model, which is low compared to failure strains in compression (0.002775) and tension (0.00133). For the 1V20-D25-Unc model, the end values for plastic strains are PEEQ=553$\mu\epsilon$ and PEEQT=630$\mu\epsilon$, which is higher than for the 1V0-Unc model but still below the failure strains in compression and tension. Although the mis-alignment clearly has an effect on the pavement, there is no damage according to our criteria.

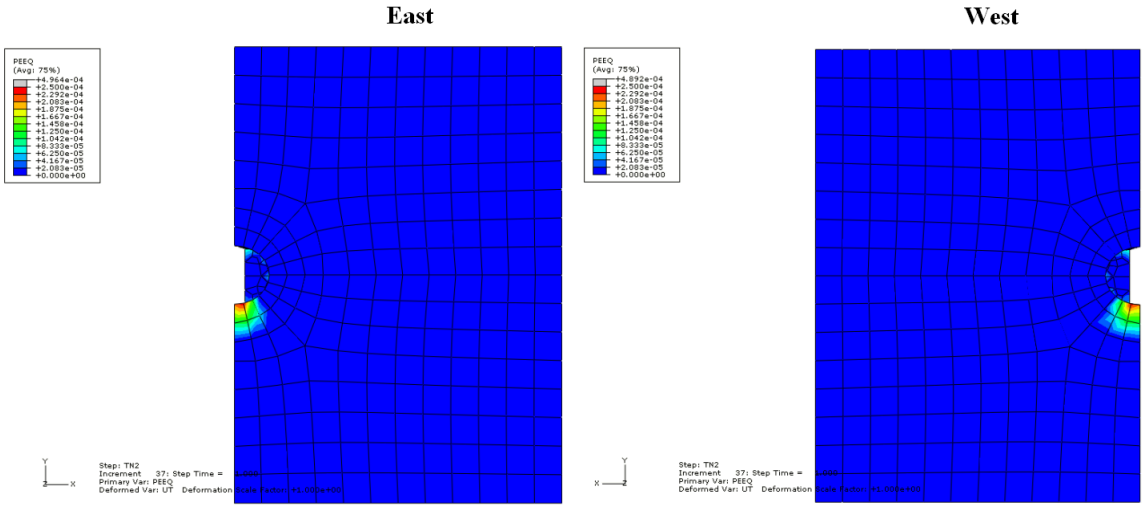

Figure 5.12: Plastic strains in compression for model 1V0-Unc

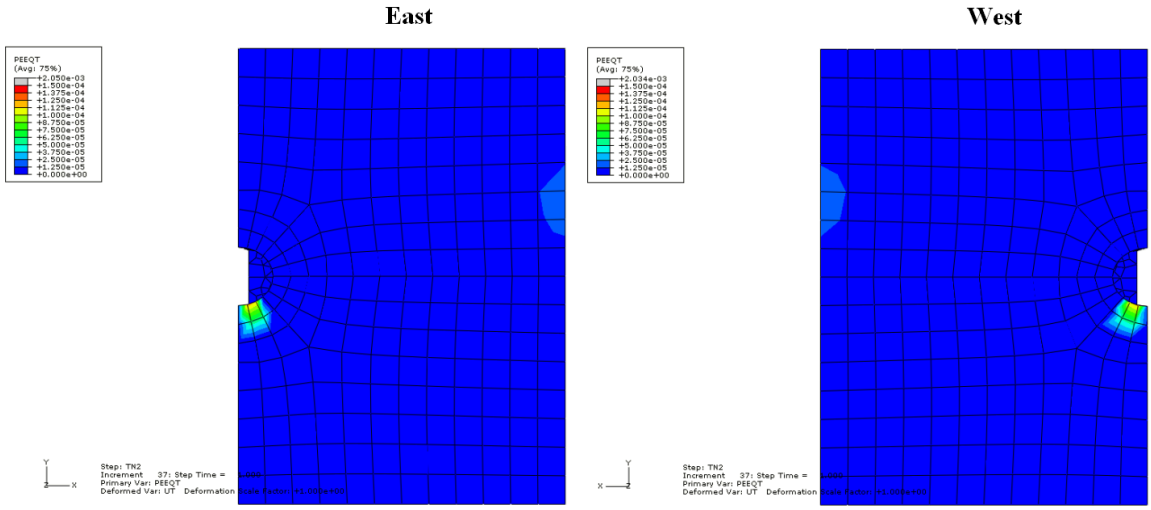

Figure 5.13: Plastic strains in tension for model 1V0-Unc

5.2.3 Load Transfer Efficiency

For each case, two measures of the load transfer efficiency of the joint are used. The first one is the deflection-based load transfer efficiency (LTEδ or simply LTE), which was evaluated by simulating an FWD drop onto one side of the joint, over the dowel bar location. The formula utilized was shown previously (Equation 2.1). FWD loads generally range from 40 to 70 kN, and are applied with a circular loading plate of diameter 300 mm. In the current analysis, the shape of the loading surface is rectangular for simplicity of modelling. To simulate an FWD load in the 3D-FEM model, a 35 kN (=70 kN/2) was applied monotonically from zero to the final value at the end of the second temperature cycle, that is at 10am; the initial magnitude of slab curling determined by the time of the day has an effect on the results; the LTE is expected to be higher during the night than during the day. This is due to the the slab being less curled up during the day, which causes the slab to make contact with the base earlier when the FWD load is applied, allowing more of the load to be transferred to the ground and less through the dowel bar. For models with angular misalignment, LTE is taken as the average between LTE obtained with an FWD load applied to each side of the joint.

The second measure of joint efficiency is the transferred load efficiency (TLE), and was

done by comparing the vertical shear force in the dowel bar (total vertical force transmitted by the dowel at the joint) to the load applied by the FWD. The shear force is estimated using Equation 5.3.

$$V = \frac{3}{4} G A \gamma \tag{5.3}$$

where:

V is the vertical shear force in the dowel

$G = 76,923$ MPa is the shear modulus of the dowel

$A = 8.04 \times 10^{-4}$ m^2 is the area of the section of one-half of the bar

γ is the shear strain at the middle of the bar determined from ABAQUS model

The following results were obtained for the models analyzed in the previous section. For 1V0-Unc, final load transfer efficiency is 84.6 % while transferred load efficiency is 26.7 %. For 1V20-D25-Unc, load transfer efficiency is 89.2 % while transferred load efficiency is 31.3 %. The difference observed between the values from model to model will be discussed in the upcoming parametric study. The difference between the two measures of joint performance can be explained by the fact that the majority of the load is borne by the concrete and transferred to the subgrade. The high LTE also indicates that the dowel bar is effectively transferring the deflections accross the joint.

5.3 Parametric Study

5.3.1 Introduction

The parametric study is carried out using the parameters described in Table 5.1. The analysis consists of comparing the overall behaviour with the bar axial force – joint opening graphs, examining local damage that may occur, and comparing load transfer efficiency. The possibility of significant damage and subsequent loss of performance of the joint are discussed as well.

5.3.2 Influence of Bar Vertical Displacement

The influence of mis-placement of the bar was studied with an uncoated dowel bar. The two types of mis-placement that are examined are the bar vertical displacement and vertical misalignment in a vertical plane. The effect of vertical displacement of the dowel bar is studied with two angular misalignment values of 0 mm (non-misaligned) and 60 mm. For a straight bar (no angular misalignment), models 1V0-Unc and 1V0-D25-Unc are compared. A summary of output values are shown in Table 5.2. Figures 5.14 and 5.15 are comparative plots of the bar axial force as a function of joint opening and the bar bending moment as a function of joint uplift.

The bar force and moment, and the joint deflections, are all greater for the 1V0-D25-Unc model compared to the 1V0-Unc model. When the bar is placed higher, upward curling (shrinkage and cooling) causes more bending in the bar because the slab curls more at the top. Thus, the dowel bar is pulled farther out of the slab, which increases the axial tension force acting on the bar due to friction. The increased axial force on the bar induces a larger slip surface between the steel and the concrete, which is consistent with the slightly higher joint deflections for the 1V0-D25-Unc model compared to the 1V0-Unc model. When the day-time temperature cycle is applied for the 1V0-D25-Unc model, the bar takes longer to go back in a situation of end-bearing with the concrete at the end of the pocket. Therefore,

Table 5.2: Influence of bar vertical displacement on joint behaviour (no angular misalignment)

Model ID	1V0-Unc	1V0-D25-Unc
Maximum joint opening (mm)	0.925	0.931
Maximum joint uplift (mm)	1.932	2.028
Maximum bar force, tension (kN)	1.56	3.95
Minimum bar force, compression (kN)	-17.4	-29.9
Maximum bar moment (Nm)	-236	-349.7
Initiation of plastic behaviour at the joint	First cooling cycle; $\Delta T \approx 5^{\circ}C$	Shrinkage step; $\epsilon_{sh} \approx 310\mu\epsilon$
PEEQ at the joint ($\mu\epsilon$)	274	394
PEEQT at the joint ($\mu\epsilon$)	223	445
PEEQ end of pocket ($\mu\epsilon$)	493	534
PEEQT end of pocket ($\mu\epsilon$)	2043	1333
LTE (%)	84.6	88.8
TLE (%)	26.7	29.0

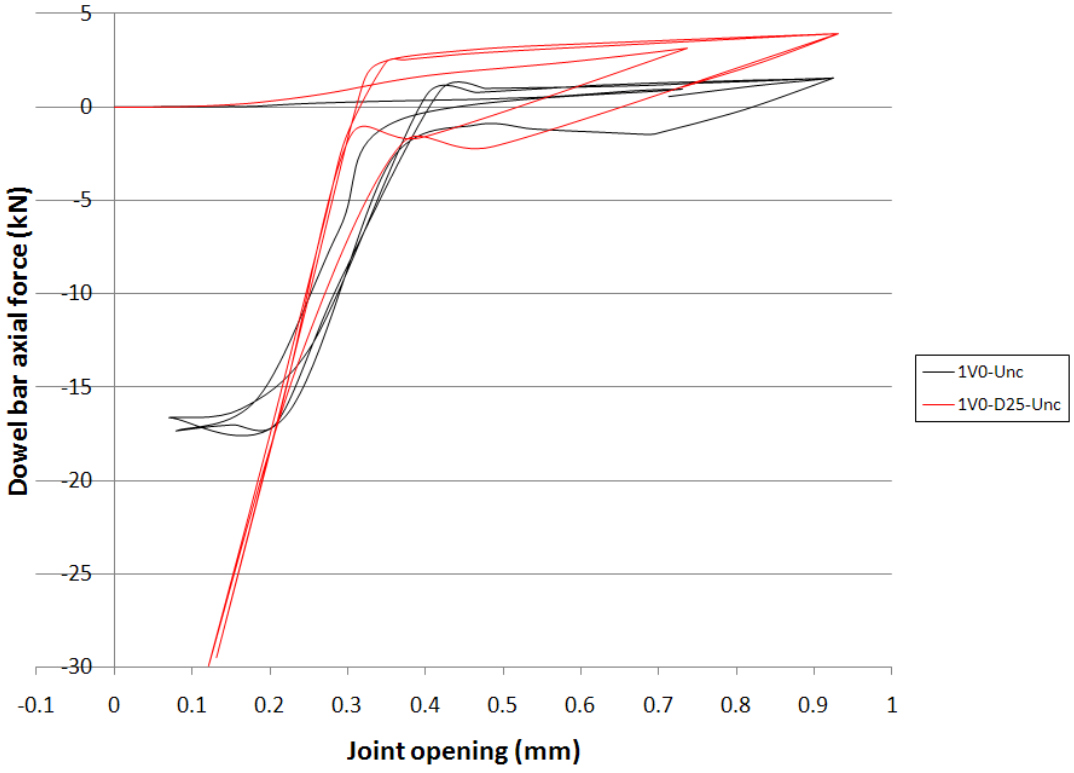

Figure 5.14: Comparison of dowel bar axial force vs. joint opening for models 1V0-Unc and 1V0-D25-Unc

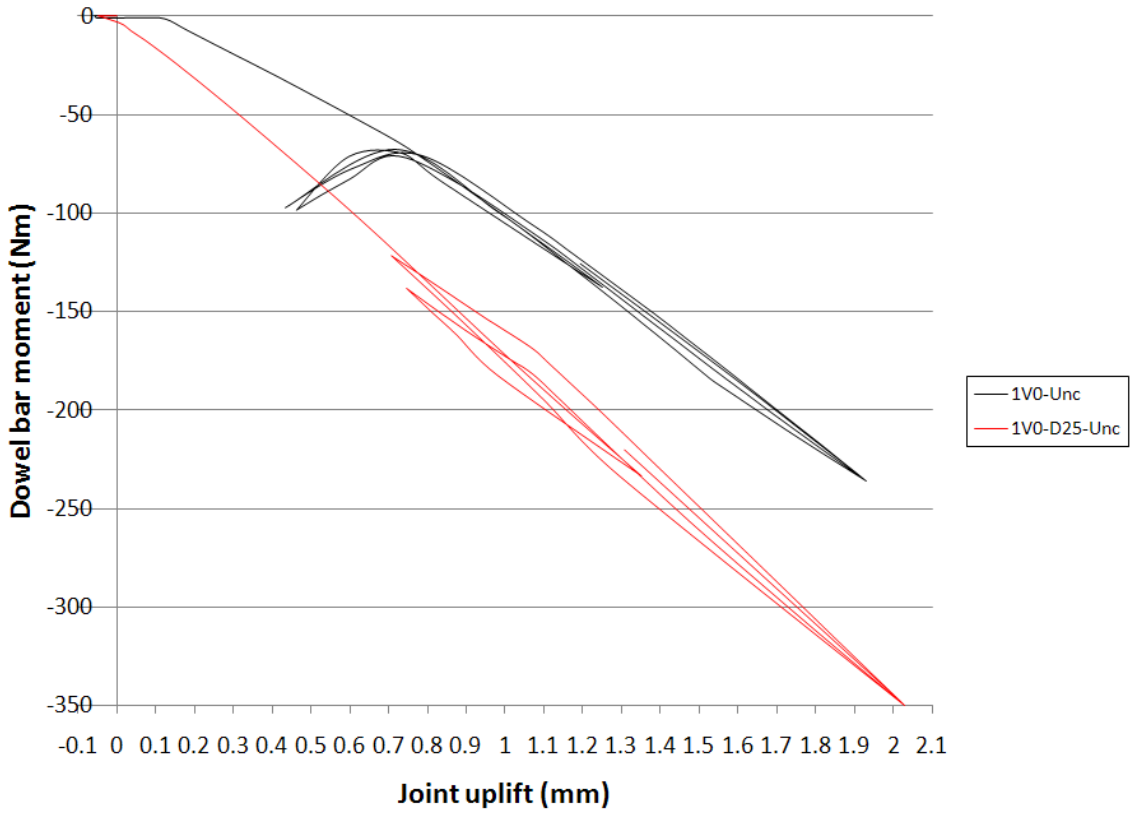

Figure 5.15: Comparison of dowel bar bending moment vs. joint uplift for models 1V0-Unc and 1V0-D25-Unc

less plastic damage is induced by end bearing of the dowel against the concrete, this can be seen in the plastic strains in tension in the concrete at the end of the bar: for 1V0, PEEQT=0.00205, whereas for 1V0-D25-Unc, PEEQT=0.00133, which means that the zone has just started to become significantly plastic.

The local concrete plastic strains around the dowel at the joint increase when the bar is placed higher. For a misalignment displacement of +25 mm, PEEQ increases by 44 %, while PEEQT increases by 100 % in comparison to the non-misaligned case. Moreover the plastic strains already develop during the shrinkage step for the 1V0-D25-Unc model while they develop only during the night-time temperature step for the 1V0-Unc model. The increased bending of the bar and consequent shearing of the concrete beneath the bar account for these increased strains. Yet, the absolute values of the equivalent plastic strains remain

limited and well bellow the concrete failure criteria, suggesting damage is not significant.

Finally, the two measures of joint performance, LTE and TLE, are higher in the 1V0-D25-Unc model; when the bar is placed higher, it bears more of the applied FWD load. Assuming that the FWD load is distributed within a cone of a certain angle, more force is transmitted to the dowel bar when it is placed higher in the slab since the dowel bar intercepts more lines of influence of a higher stress level. This concept is illustrated on Figure 5.16, and the predicted vertical stresses due to the FWD load are shown on Figure 5.17.

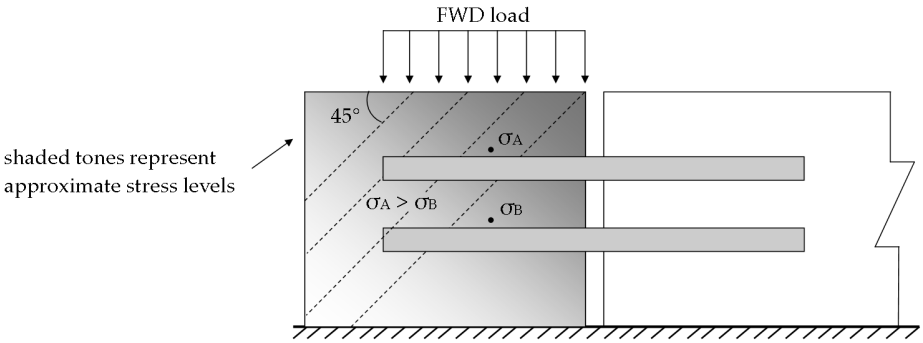

Figure 5.16: FWD force transfer in the concrete for two different bar heights

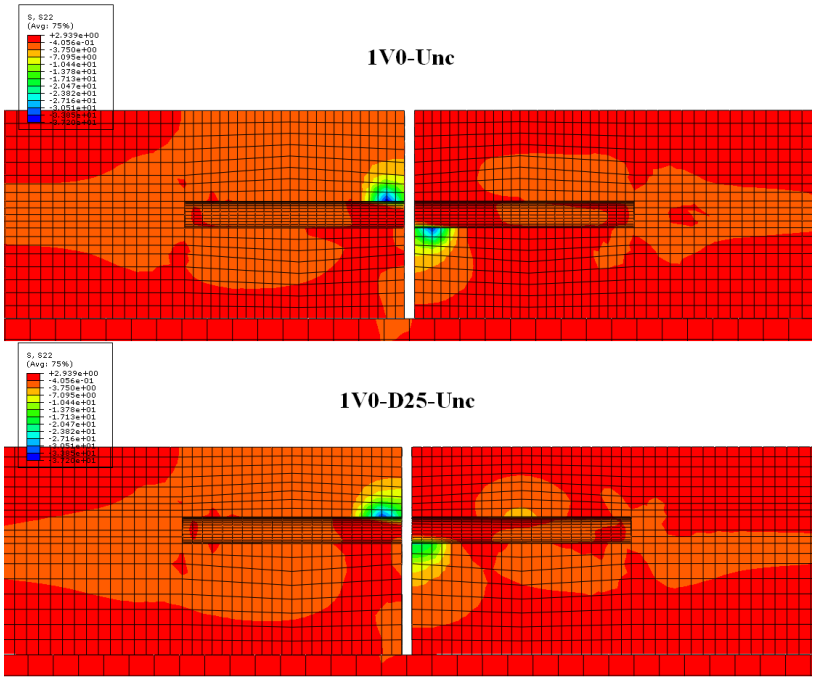

Figure 5.17: Vertical stresses in the concrete for models 1V0-Unc and 1V0-D25-Unc (bar removed)

The influence of bar vertical displacement was also considered for misaligned cases, for models 1V60-Unc and 1V60-D25-Unc. The results are summarized in Table 5.3. The vertical displacement of the bar results in bar axial forces a little higher, and bending moment approximately similar. On the east side of the joint (up side), the predicted plastic strains in compression and tension are lower or equal, while on the west side, the plastic strains in compression PEEQ are reduced and the plastic strains in tension PEEQT are higher. Globally, the joint load tranfer efficiency measures indicate slightly better performance of the model 1V60-D25-Unc.

Table 5.3: Influence of bar vertical displacement on joint behaviour (misaligned bar)

Model ID	1V60-Unc	1V60-D25-Unc
Maximum joint opening (mm)	0.886	0.860
Maximum joint uplift (mm)	1.859	1.767
Maximum bar force, tension (kN)	11.0	12.2
Minimum bar force, compression (kN)	-28.5	-33.2
Maximum bar moment (Nm)	-390	-386
Initiation of plastic behaviour at the joint	Shrinkage step; $\epsilon_{sh} \approx 190\mu\epsilon$	Shrinkage step; $\epsilon_{sh} \approx 230\mu\epsilon$
PEEQ at the joint, east side ($\mu\epsilon$)	264	195
PEEQ at the joint, west side ($\mu\epsilon$)	953	741
PEEQT at the joint, east side ($\mu\epsilon$)	434	433
PEEQT at the joint, west side ($\mu\epsilon$)	717	796
PEEQ end of pocket, east side ($\mu\epsilon$)	189	200
PEEQ end of pocket, west side ($\mu\epsilon$)	0	0
PEEQT end of pocket, east side ($\mu\epsilon$)	688	695
PEEQT end of pocket, west side ($\mu\epsilon$)	1160	674
LTE (%)	88.9	89.3
TLE (%)	30.3	31.4

5.3.3 Influence of Bar Angular Misalignment

The results described in the previous section showed that a bar placed at a higher height was likely to be more detrimental for joint performance than a bar set at proper depth (midslab). Hence the influence of the dowel bar angular misalignment will be prinarily evaluated with a bar set 25 mm higher than slab mid-height.

For a bar placed at midslab, models 1V0-Unc and 1V60-Unc are compared (Table 5.4 and Figures 5.18 and 5.19). The misaligned bar places more restraint on joint opening and uplift, with increases in compressive axial force and bending moment of 64 % and 65 %, respectively. Plastic zones at the joint develop much more rapidly with the misaligned bar, since the plastic strains in compression and tension become non-zero on both sides of the joint during the shrinkage step. The peak plastic strains are higher when the bar is misaligned, in particular on the west side (low side), but stay within the limits of the damage criteria for this study, suggesting significant damage has not occurred. The LTE and TLE values are higher in the 1V60-Unc model, which indicates two things: first, the misaligned bar position is slightly more advantageous with regards to FWD load transfer. Secondly, the damage that occurs when shrinkage and two temperature cycles are applied is not significant enough to cause a decrease in joint load tranfer efficiency.

Table 5.4: Influence of bar angular misalignment on joint behaviour (bar at mid-depth)

Model ID	1V0-Unc	1V60-Unc
Maximum joint opening (mm)	0.925	0.886
Maximum joint uplift (mm)	1.932	1.859
Maximum bar force, tension (kN)	1.56	11.0
Minimum bar force, compression (kN)	-17.4	-28.5
Maximum bar moment (Nm)	-236	-390
Initiation of plastic behaviour at the joint	First temperature cycle; $\Delta T \approx 5^{\circ}C$	Shrinkage step; $\epsilon_{sh} \approx 190\mu\epsilon$
PEEQ at the joint, east side ($\mu\epsilon$)	272	264
PEEQ at the joint, west side ($\mu\epsilon$)	276	953
PEEQT at the joint, east side ($\mu\epsilon$)	220	434
PEEQT at the joint, west side ($\mu\epsilon$)	226	717
PEEQ end of pocket, east side ($\mu\epsilon$)	496	189
PEEQ end of pocket, west side ($\mu\epsilon$)	489	0
PEEQT end of pocket, east side ($\mu\epsilon$)	2051	688
PEEQT end of pocket, west side ($\mu\epsilon$)	2034	1160
LTE (%)	84.6	88.9
TLE (%)	26.7	30.3

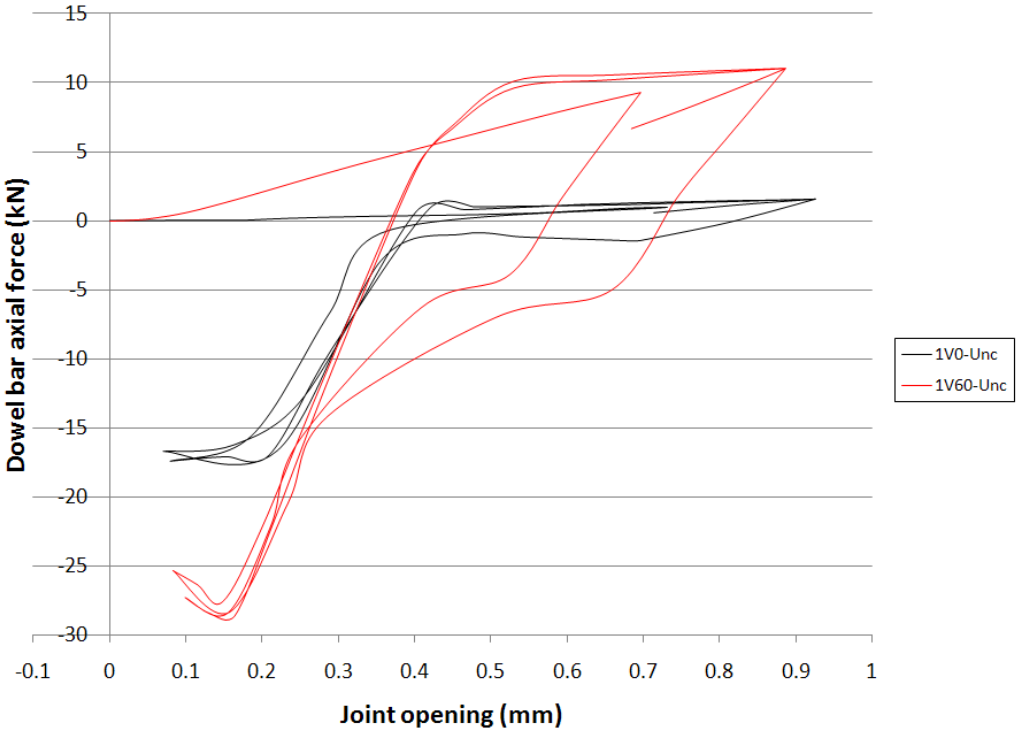

Figure 5.18: Comparison of dowel bar axial force vs. joint opening for models 1V0-Unc and 1V6(

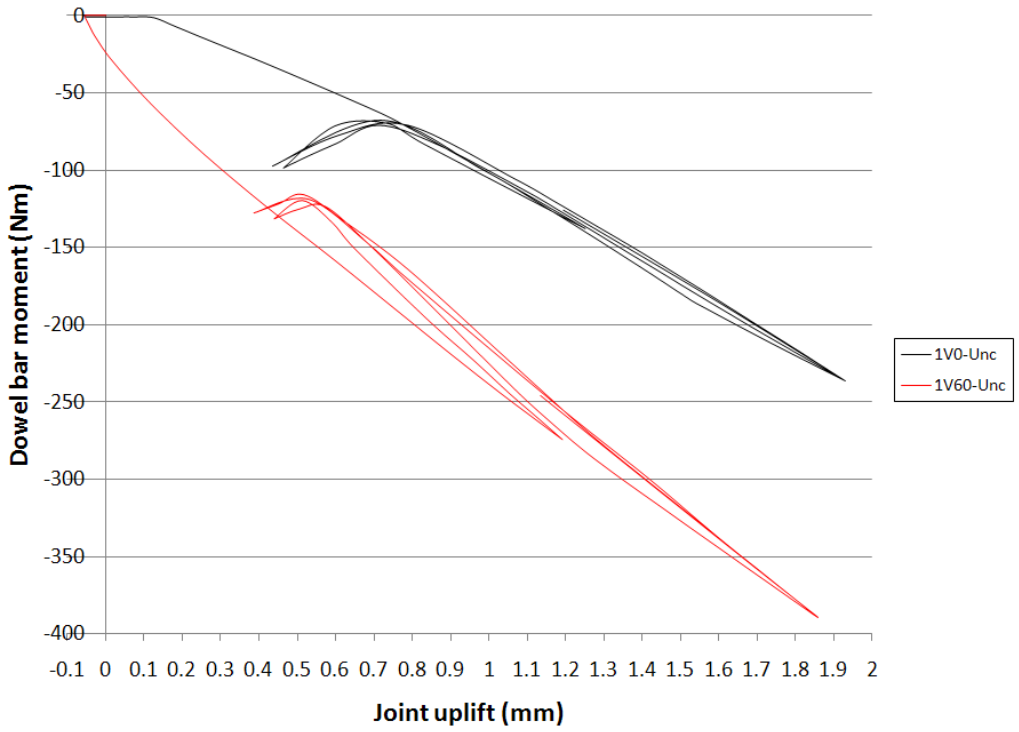

Figure 5.19: Comparison of dowel bar bending moment vs. joint uplift for models 1V0-Unc and 1V60-Unc

The influence of bar vertical angular misalignment was studied more extensively with a bar displaced 25 mm upwards. Angular misalignment values of 0, 20, 30 and 60 mm were used; Table 5.5 summarizes the results. As in the previous case, the presence of misalignment causes more restraint to joint movement and the dowel bar has to to bear further axial force and bending moment. Globally, the highest plastic strains, on the order of magnitude of 800 microstrains, develop with the highest degree of misalignment (60 mm). However, while these strains are increasing on the west side of the joint (down side), they are actually a decreasing function of vertical misalignment on the east side (up side). This non-symmetrical behaviour is illustrated on Figure 5.20; the bar is resisting the curvature of the slab more on the west side than on the east side, causing increased damage on the west side, and less damage on the east side compared to the straight bar model. Hence, the angular position of the bar with regards to the global displacement vectors is such that an angle which minimizes plastic strains on one side will at the same time maximize plastic strains on the other side.

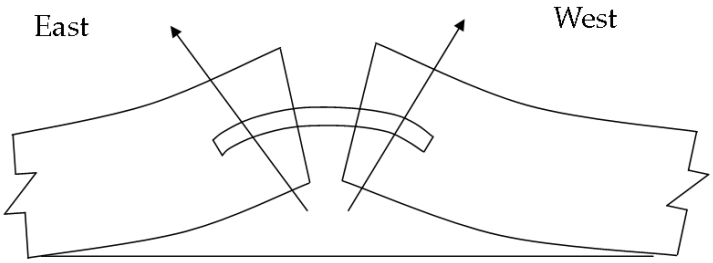

1. Non-misaligned bar

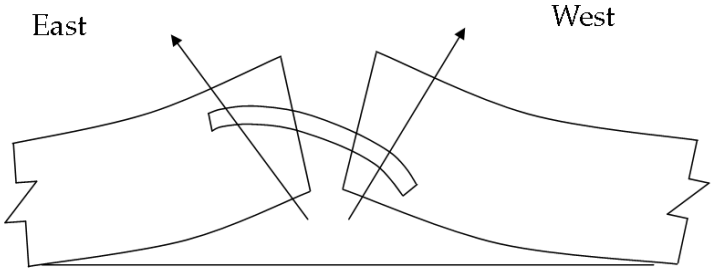

2. Misaligned bar

Figure 5.20: Displacement vectors due to slab curling for non-misaligned and misaligned bars

Table 5.5: Influence of bar angular misalignment on joint behaviour (bar vertically displaced 25 mm)

Model ID	1V0-D25-Unc	1V20-D25-Unc	1V30-D25-Unc	1V60-D25-Unc
Maximum joint opening (mm)	0.931	0.849	0.858	0.860
Maximum joint uplift (mm)	2.028	1.741	1.761	1.767
Maximum bar force, tension (kN)	3.95	14.7	13.0	12.2
Minimum bar force, compression (kN)	-30.0	-42.0	-35.7	-33.2
Maximum bar moment (Nm)	-350	-381	-381	-386
Initiation of plastic behaviour at the joint	Shrinkage step; $\epsilon_{sh} \approx 310\mu\epsilon$	$\epsilon_{sh} \approx 190\mu\epsilon$	$\epsilon_{sh} \approx 270\mu\epsilon$	$\epsilon_{sh} \approx 230\mu\epsilon$
PEEQ at the joint, east side ($\mu\epsilon$)	416	326	245	195
PEEQ at the joint, west side ($\mu\epsilon$)	380	553	671	741
PEEQT at the joint, east side ($\mu\epsilon$)	463	630	629	433
PEEQT at the joint, west side ($\mu\epsilon$)	421	605	643	796
PEEQ end of pocket, east side ($\mu\epsilon$)	520	113	150	200
PEEQ end of pocket, west side ($\mu\epsilon$)	549	94	116	0
PEEQT end of pocket, east side ($\mu\epsilon$)	1482	269	617	695
PEEQT end of pocket, west side ($\mu\epsilon$)	1183	406	608	674
LTE (%)	88.8	89.2	89.1	89.3
TLE (%)	29.0	31.3	31.3	31.4

5.3.4 Influence of Bar Coating

The effect of concrete–dowel friction values and the presence of a bond breaker were studied for three different bar misalignments, using models 1V0, 1V20-D25 and 1V60-D25.

For the straight non-misaligned bar model (control case), the bar forces and moment are higher when a bond breaker is used rather than not (Table 5.6). The reason lies in the fact that when the coefficient of friction is lower, from the shrinkage step onwards the contact shear stress at the steel/concrete interface reaches the critical slip line quicker. That is, more slippage of the bar occurs, resulting in more bending and more pullout forces acting on the bar. This leads to further damage around the dowel at the joint, in particular in compression, where PEEQ increases by 85 to 89 % when a bond breaker is applied. During the heating step, the bar comes back into the pocket but does not compress the concrete as much as when the bar is uncoated; thus, tensile damage at the end of the pocket is decreased (PEEQT=0.00165 for 1V0-C whereas PEEQT=0.00205 for 1V0-Unc). Furthermore, by the bar not bearing against the concrete as quickly as in the uncoated bar case, the reversal of the bending of the bar is not as pronounced (point E to F in Figure 5.3). This has the effect of reducing the loss of contact between the dowel bar and the concrete, resulting in slightly improved joint efficiency.

In the case of misaligned bar models 1V20-D25 and 1V60-D25, the effect of bar misalignment modifies the findings (Tables 5.7 and 5.8). The presence of a bond breaker reduces the axial forces in the bar while increasing the bending moment. This is due to the bar being pulled out from the east side (up side) because of reduced friction, and staying in the pocket on the west side (down side). A lesser length of the bar is able to resist joint uplift, resulting in increased bending in the bar. As can be seen in Table 5.7, plastic strains in compression are higher on the east side of the joint for 1V20-D25-C (increased bending), while the plastic strains in tension are lower on both sides (increased slip).

The simulation of a slightly corroded dowel bar (model 1V20-D25-Corr) gives the opposite predictions: an increase in the bar axial force and a reduction in the bar bending moment

Table 5.6: Influence of bar coating on joint behaviour (1V0)

Model ID	1V0-Unc	1V0-C
Maximum joint opening (mm)	0.925	0.906
Maximum joint uplift (mm)	1.932	1.870
Maximum bar force, tension (kN)	1.56	4.4
Minimum bar force, compression (kN)	-17.4	-33.5
Maximum bar moment (Nm)	-236	-398
Initiation of plastic behaviour at the joint	First temperature cycle; $\Delta T \approx 5°C$	Shrinkage step; $\epsilon_{sh} \approx 200\mu\epsilon$
PEEQ at the joint, east side ($\mu\epsilon$)	272	515
PEEQ at the joint, west side ($\mu\epsilon$)	276	506
PEEQT at the joint, east side ($\mu\epsilon$)	220	382
PEEQT at the joint, west side ($\mu\epsilon$)	226	384
PEEQ end of pocket, east side ($\mu\epsilon$)	496	153
PEEQ end of pocket, west side ($\mu\epsilon$)	489	157
PEEQT end of pocket, east side ($\mu\epsilon$)	2051	1645
PEEQT end of pocket, west side ($\mu\epsilon$)	2034	1400
LTE (%)	84.6	88.7
TLE (%)	26.7	30.6

are observed, while PEEQ is lower on the east side, and PEEQT is higher on both sides, but remains controlled at about 60 % of PEEQT at failure. For model 1V60-D25-Corr, PEEQT reaches 0.0011, which represents 83 % of PEEQT at failure; this situation could become critical if a large number of temperature cycles were applied to the pavement, should a crack form and expand in the concrete surrounding the dowel. To explore this possibility, additional temperature cycles were run on the 1V60-D25-Corr model, for a total of ten cycles. The results of this study are discussed in a subsequent section.

Table 5.7: Influence of bar coating on joint behaviour (1V20-D25)

Model ID	1V20-D25-Unc	1V20-D25-C	1V20-D25-Corr
Maximum joint opening (mm)	0.849	0.899	0.806
Maximum joint uplift (mm)	1.741	1.846	1.641
Maximum bar force, tension (kN)	14.7	4.4	23.6
Minimum bar force, compression (kN)	-42.0	-32.9	-47.8
Maximum bar moment (Nm)	-381	-412	-362
Initiation of plastic behaviour at the joint	Shrinkage step; $\epsilon_{sh} \approx 190\mu\epsilon$	Shrinkage step; $\epsilon_{sh} \approx 210\mu\epsilon$	Shrinkage step; $\epsilon_{sh} \approx 190\mu\epsilon$
PEEQ at the joint, east side ($\mu\epsilon$)	326	382	239
PEEQ at the joint, west side ($\mu\epsilon$)	553	470	507
PEEQT at the joint, east side ($\mu\epsilon$)	630	403	768
PEEQT at the joint, west side ($\mu\epsilon$)	605	509	780
PEEQ end of pocket, east side ($\mu\epsilon$)	113	155	0
PEEQ end of pocket, west side ($\mu\epsilon$)	94	92	22
PEEQT end of pocket, east side ($\mu\epsilon$)	269	1124	0
PEEQT end of pocket, west side ($\mu\epsilon$)	406	1056	89
LTE (%)	89.2	89.0	88.8
TLE (%)	31.3	30.7	31.3

Table 5.8: Influence of bar coating on joint behaviour (1V60-D25)

Model ID	1V60-D25-Unc	1V60-D25-C	1V60-D25-Corr
Maximum joint opening (mm)	0.860	0.902	0.827
Maximum joint uplift (mm)	1.767	1.853	1.692
Maximum bar force, tension (kN)	12.2	4.44	18.9
Minimum bar force, compression (kN)	-33.2	-31.4	-31.8
Maximum bar moment (Nm)	-386	-407	-373
Initiation of plastic behaviour at the joint	Shrinkage step; $\epsilon_{sh} \approx 230\mu\epsilon$	Shrinkage step; $\epsilon_{sh} \approx 270\mu\epsilon$	Shrinkage step; $\epsilon_{sh} \approx 170\mu\epsilon$
PEEQ, east side ($\mu\epsilon$)	195	298	265
PEEQ, west side ($\mu\epsilon$)	741	576	801
PEEQT, east side ($\mu\epsilon$)	433	594	270
PEEQT, west side ($\mu\epsilon$)	796	515	1100
PEEQ end of pocket, east side ($\mu\epsilon$)	200	162	87
PEEQ end of pocket, west side ($\mu\epsilon$)	0	88	91
PEEQT end of pocket, east side ($\mu\epsilon$)	695	1328	237
PEEQT end of pocket, west side ($\mu\epsilon$)	674	1167	452
LTE (%)	89.3	88.7	89.1
TLE (%)	31.4	30.7	31.4

5.3.5 Influence of Concrete Coefficient of Thermal Expansion

The effect of the concrete coefficient of thermal expansion on joint performance was evaluated with model 1V0, 1V20-D25 and 1V60-D25 (Tables 5.9, 5.10 and 5.10). The predicted 3D-FEM results show that the during the heating step, a coefficient $\alpha = 8 \times 10^{-6}/°C$ means that the concrete does not expand as much as when $\alpha = 11 \times 10^{-6}/°C$, so that the bar makes contact with the concrete at the end of the pocket later. Hence, the bar undergoes lower axial compressive forces, and the concrete at the end of the pocket does not experience any plastic strain state (no E point). This can be seen on Figure 5.21, where the curve does not deviate between points D and F for 1V0-Unc-α8 as it does for 1V0-Unc (Figure 5.2). Similarly, during the cooling step, the slabs contract less than the case with a higher coefficient of thermal expansion, explaining the lower bending moment in the dowel bar. As a consequence, plastic damage occurring at the joint is reduced. The LTE and TLE values are very close in both cases so the effect of a lower coefficient of thermal expansion on joint load transfer performance is negligible.

When the bar is misaligned, the effect of a lower coefficient of thermal expansion is more pronounced. When the concrete expands, the bar makes contact with the concrete at the end of the pocket only on one side for the models with reduced α. Furthermore, the axial compressive forces on the bar are lower, and the concrete at the end of the pocket experience plastic strain change only on one side when α is reduced. This can be seen on Figures 5.22 and 5.23, the curve does not deviate between points E and F for the models with $\alpha = 8 \times 10^{-6}/°C$, as it does for $\alpha = 11 \times 10^{-6}/°C$, as in Figure 5.5. Similarly, the dowel bar undergoes a lower bending moment when the slabs cool down, and the plastic damage occurring at the joint is reduced for models with lower α. The joint efficiency values are very close in all cases so the effect of a lower coefficient of thermal expansion on joint performance can be considered negligible.

Table 5.9: Influence of coefficient of thermal expansion on joint behaviour (bar at mid-depth)

Model ID	1V0-Unc	1V0-Unc-α8
Maximum joint opening (mm)	0.925	0.872
Maximum joint uplift (mm)	1.932	1.743
Maximum bar force, tension (kN)	1.56	1.38
Minimum bar force, compression (kN)	-17.4	-15.7
Maximum bar moment (Nm)	-236	-211
Initiation of plastic behaviour at the joint	First temperature cycle; $\Delta T \approx 5^{\circ}C$	First temperature cycle; $\Delta T \approx 5^{\circ}C$
PEEQ at the joint, east side ($\mu\epsilon$)	272	160
PEEQ at the joint, west side ($\mu\epsilon$)	220	156
PEEQT at the joint, east side ($\mu\epsilon$)	276	161
PEEQT at the joint, west side ($\mu\epsilon$)	226	156
PEEQ end of pocket, east side ($\mu\epsilon$)	496	23
PEEQ end of pocket, west side ($\mu\epsilon$)	489	22
PEEQT end of pocket, east side ($\mu\epsilon$)	2051	425
PEEQT end of pocket, west side ($\mu\epsilon$)	2034	422
LTE (%)	84.6	84.7
TLE (%)	26.7	26.6

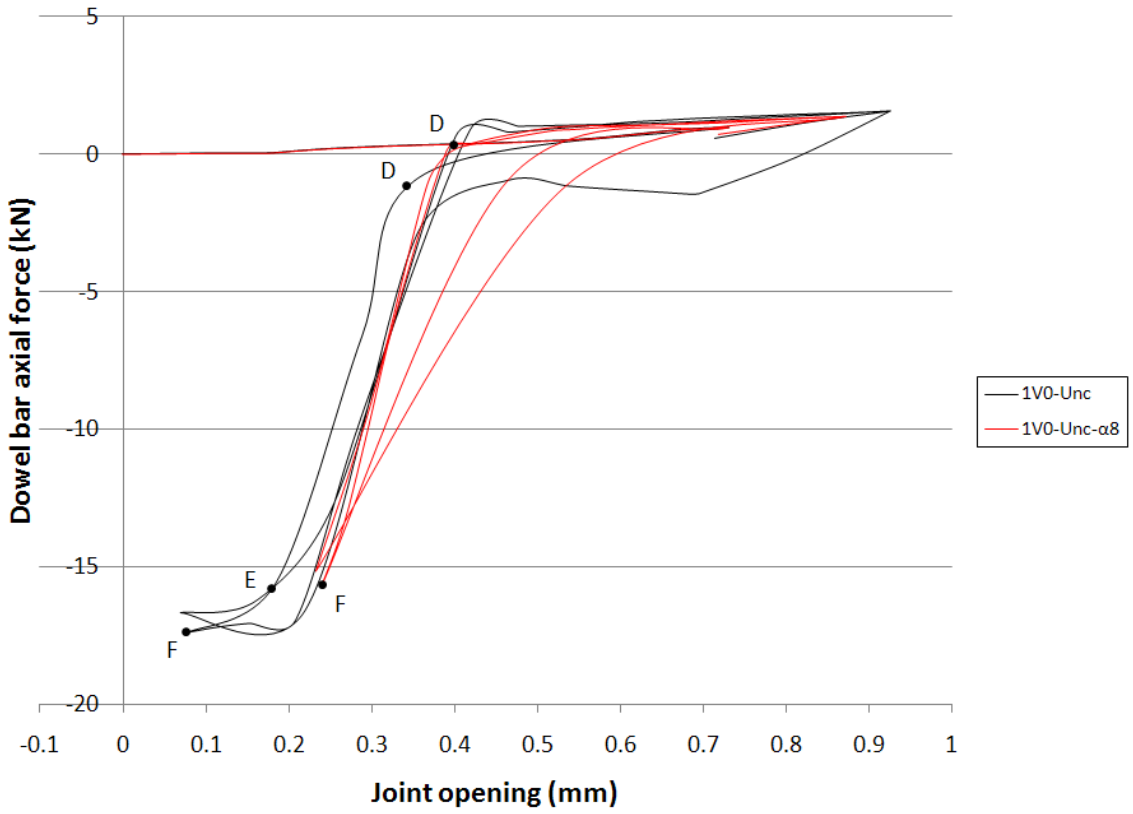

Figure 5.21: Comparison of dowel bar axial force vs. joint uplift for models 1V0-Unc and 1V0-Unc-α8

Table 5.10: Influence of coefficient of thermal expansion on joint behaviour (1V20-D25)

Model ID	1V20-D25-Unc	1V20-D25-Unc-α8
Maximum joint opening (mm)	0.849	0.872
Maximum joint uplift (mm)	1.741	1.743
Maximum bar force, tension (kN)	14.7	1.38
Minimum bar force, compression (kN)	-42.0	-15.7
Maximum bar moment (Nm)	-381	-211
Initiation of plastic behaviour at the joint	Shrinkage step; $\epsilon_{sh} \approx 190\mu\epsilon$	Shrinkage step; $\epsilon_{sh} \approx 190\mu\epsilon$
PEEQ at the joint, east side ($\mu\epsilon$)	326	263
PEEQ at the joint, west side ($\mu\epsilon$)	553	488
PEEQT at the joint, east side ($\mu\epsilon$)	630	570
PEEQT at the joint, west side ($\mu\epsilon$)	605	531
PEEQ end of pocket, east side ($\mu\epsilon$)	113	0
PEEQ end of pocket, west side ($\mu\epsilon$)	94	0
PEEQT end of pocket, east side ($\mu\epsilon$)	269	0
PEEQT end of pocket, west side ($\mu\epsilon$)	406	0
LTE (%)	89.2	87.8
TLE (%)	31.3	30.7

Table 5.11: Influence of coefficient of thermal expansion on joint behaviour (1V60-D25)

Model ID	1V60-D25-Unc	1V60-D25-Unc-α8
Maximum joint opening (mm)	0.860	0.809
Maximum joint uplift (mm)	1.767	1.588
Maximum bar force, tension (kN)	12.2	12.4
Minimum bar force, compression (kN)	-33.2	-17.1
Maximum bar moment (Nm)	-386	-357
Initiation of plastic behaviour at the joint	Shrinkage step; $\epsilon_{sh} \approx 230\mu\epsilon$	Shrinkage step; $\epsilon_{sh} \approx 230\mu\epsilon$
PEEQ at the joint, east side ($\mu\epsilon$)	195	156
PEEQ at the joint, west side ($\mu\epsilon$)	741	607
PEEQT at the joint, east side ($\mu\epsilon$)	433	457
PEEQT at the joint, west side ($\mu\epsilon$)	796	669
PEEQ end of pocket, east side ($\mu\epsilon$)	200	0
PEEQ end of pocket, west side ($\mu\epsilon$)	0	0
PEEQT end of pocket, east side ($\mu\epsilon$)	695	0
PEEQT end of pocket, west side ($\mu\epsilon$)	674	0
LTE (%)	88.3	89.4
TLE (%)	31.4	31.4

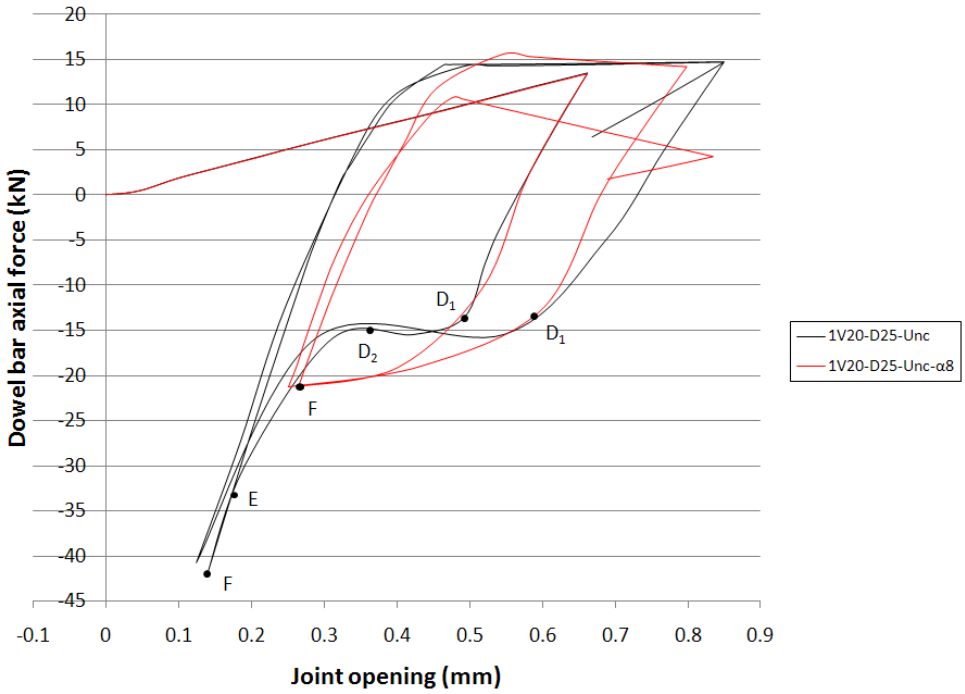

Figure 5.22: Comparison of dowel bar axial force vs. joint uplift for models 1V20-D25-Unc and 1V20-D25-Unc-α8

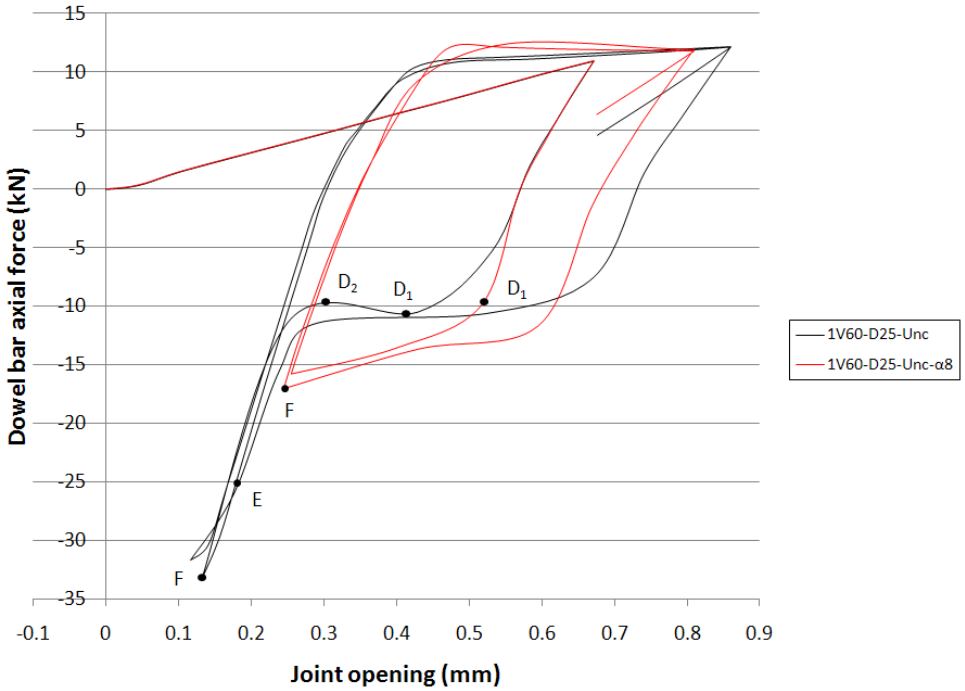

Figure 5.23: Comparison of dowel bar axial force vs. joint uplift for models 1V60-D25-Unc and 1V60-D25-Unc-α8

5.3.6 Influence of Concrete Compressive Strength

The influence of two different concrete compressive strength, 30 MPa and 50 MPa, were studied with models 1V20-D25 and 1V60-D25. The results are shown in Tables 5.12 and 5.13 and Figures 5.24 and 5.25. Slightly higher bar axial forces and moments are predicted by ABAQUS when the concrete strength is increased. The most significant difference with higher strength concrete is the increase in PEEQ on the west side, but not up to a point where crushing is going to occur. The values of PEEQ=0.00124 (model 1V20-D25-Unc-50MPa) and PEEQ=0.00132 (model 1V60-D25-Unc-50MPa) are below the crushing plastic strain for 50 MPa concrete, PEEQ=0.00156. Finally, increased compressive strength results in only an insignificant increase in joint load transfer efficiency.

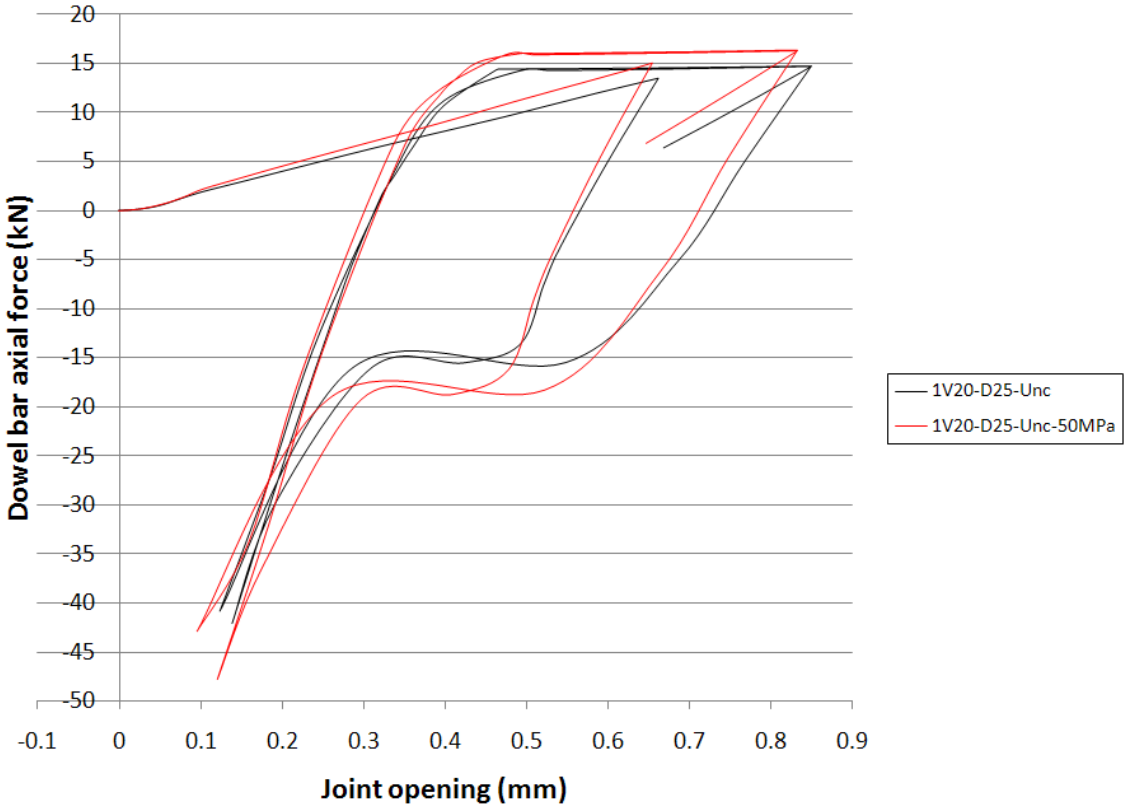

Figure 5.24: Comparison of dowel bar axial force vs. joint uplift for models 1V20-D25-Unc and 1V20-D25-Unc-50MPa

Table 5.12: Influence of concrete strength on joint behaviour (1V20-D25)

Model ID	1V20-D25-Unc	1V20-D25-Unc-50MPa
Maximum joint opening (mm)	0.849	0.833
Maximum joint uplift (mm)	1.741	1.722
Maximum bar force, tension (kN)	14.7	16.4
Minimum bar force, compression (kN)	-42.0	-47.7
Maximum bar moment (Nm)	-381	-388
Initiation of plastic behaviour at the joint	Shrinkage step; $\epsilon_{sh} \approx 190\mu\epsilon$	Shrinkage step; $\epsilon_{sh} \approx 170\mu\epsilon$
PEEQ at the joint, east side ($\mu\epsilon$)	326	495
PEEQ at the joint, west side ($\mu\epsilon$)	553	1240
PEEQT at the joint, east side ($\mu\epsilon$)	630	455
PEEQT at the joint, west side ($\mu\epsilon$)	605	541
PEEQ end of pocket, east side ($\mu\epsilon$)	113	177
PEEQ end of pocket, west side ($\mu\epsilon$)	94	136
PEEQT end of pocket, east side ($\mu\epsilon$)	269	376
PEEQT end of pocket, west side ($\mu\epsilon$)	406	500
LTE (%)	89.2	89.7
TLE (%)	31.3	32.4

Table 5.13: Influence of concrete strength on joint behaviour (1V60-D25)

Model ID	1V60-D25-Unc	1V60-D25-Unc-50MPa
Maximum joint opening (mm)	0.860	0.845
Maximum joint uplift (mm)	1.767	1.754
Maximum bar force, tension (kN)	12.2	13.5
Minimum bar force, compression (kN)	-33.2	-34.4
Maximum bar moment (Nm)	-386	-393
Initiation of plastic behaviour at the joint	Shrinkage step; $\epsilon_{sh} \approx 230\mu\epsilon$	Shrinkage step; $\epsilon_{sh} \approx 190\mu\epsilon$
PEEQ at the joint, east side ($\mu\epsilon$)	195	190
PEEQ at the joint, west side ($\mu\epsilon$)	741	1320
PEEQT at the joint, east side ($\mu\epsilon$)	433	363
PEEQT at the joint, west side ($\mu\epsilon$)	796	752
PEEQ end of pocket, east side ($\mu\epsilon$)	200	255
PEEQ end of pocket, west side ($\mu\epsilon$)	0	136
PEEQT end of pocket, east side ($\mu\epsilon$)	695	737
PEEQT end of pocket, west side ($\mu\epsilon$)	674	0
LTE (%)	89.3	89.7
TLE (%)	31.4	32.4

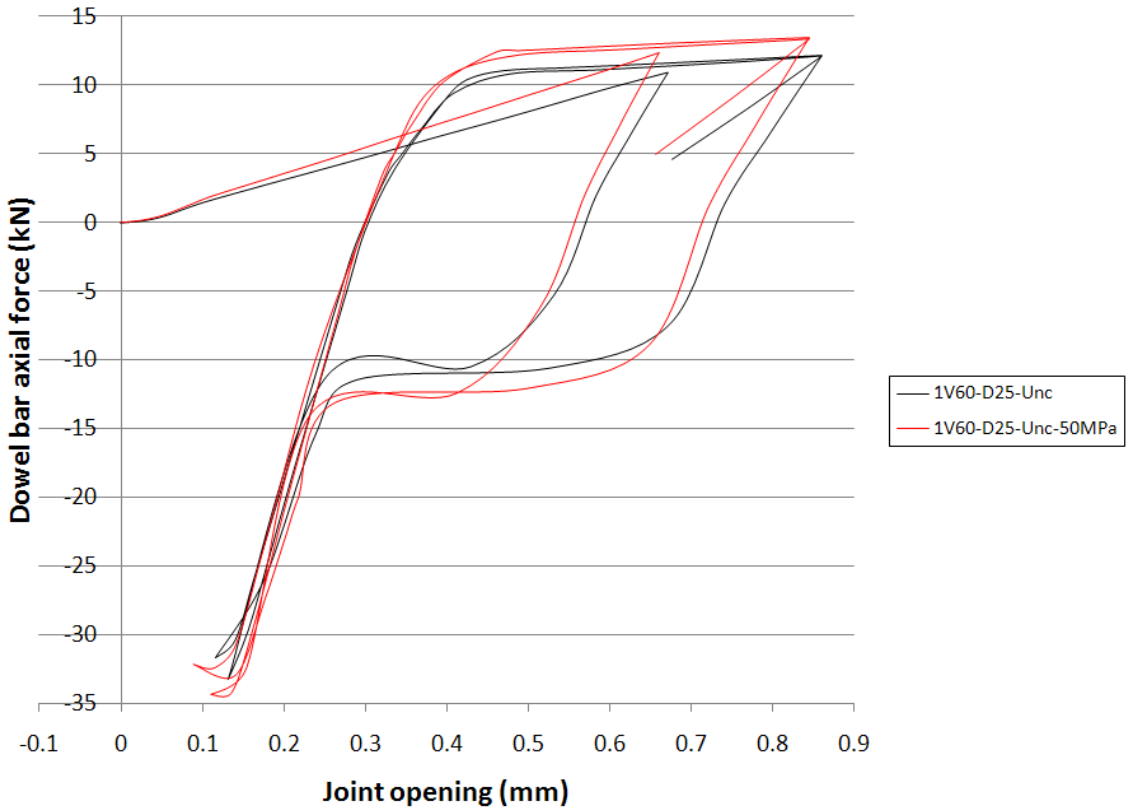

Figure 5.25: Comparison of dowel bar axial force vs. joint uplift for models 1V60-D25-Unc and 1V60-D25-Unc-50MPa

5.4 Model Verification

5.4.1 Introduction

The results obtained from the single bar finite element models were compared with the results of published data of field studies to ensure proper order of magnitude of the studied effects. A model representing half of the slab was developed for ease of comparison with published data (Model 2 in Figure 3.1). The model, containing five and half dowel bars, is represented in Figure 5.26 with the associated boundary conditions. Figure 5.27 represents a detail of the mesh at the joint, showing the dowel bars. For this model, the loading function is the same as for the single bar model (shrinkage step followed by two temperature cycles) and a coarser mesh was selected because the calculations were inefficient on a full size model.

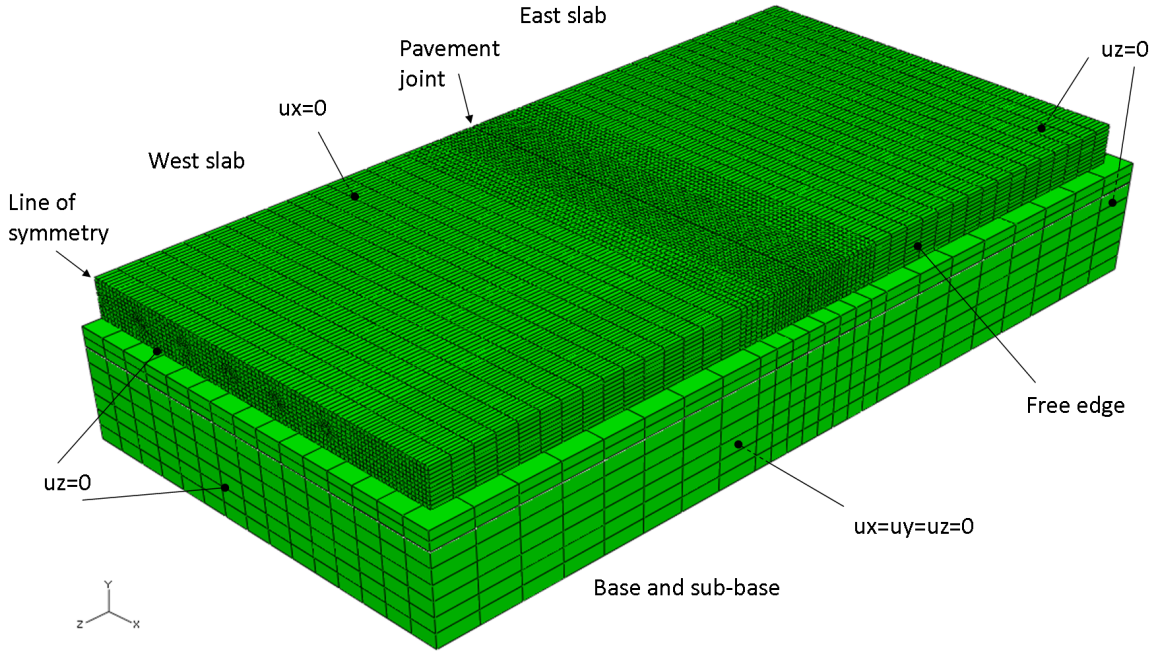

Figure 5.26: Half-slab geometry and boundary conditions

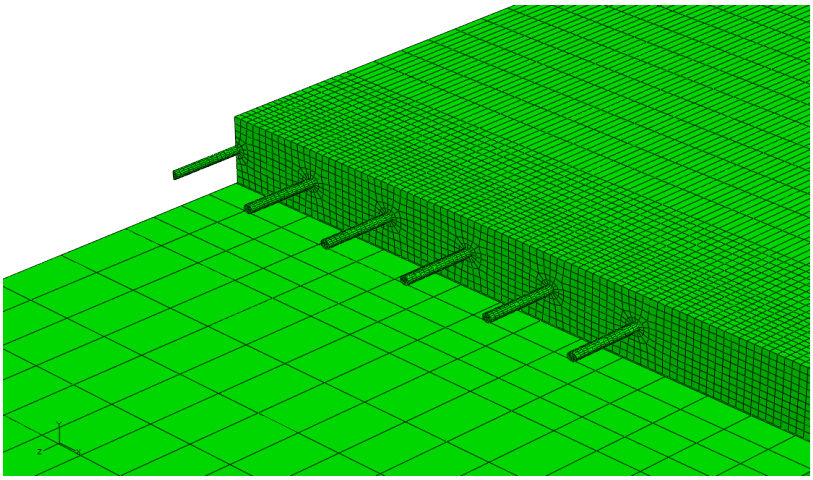

Figure 5.27: Detail of the half-slab model at the joint

5.4.2 Shrinkage Step Verification

The shrinkage function effect on the slab behaviour was compared to the results published by Jeong and Zollinger (Early-Age Curling and Warping Behaviour [39]). In the cited study, the slab corner rise was recorded after two years, which represents more than 95 % of the ultimate shrinkage depending on the curing conditions. Table 5.14 compares the characteristics of the constructed pavement from Jeong [39] to the pavement modelled in the current study. The value of the corner rise is taken at the free edge of the slab along the joint, where the displacement is at its greatest when a negative temperature gradient (cooling) is applied.

As can be seen in Table 5.14, the pavement parameters including the dowel placement and characteristics, the coefficient of thermal expansion of the concrete, and the shrinkage loading applied to the concrete slab are similar. However, the slab dimensions differ (the modelled slab is wider, less thick and shorter), which could affect deflections. Likewise, the concrete modulus of elasticity is globally lower in the modelled pavement, which would induce more curling. Nevertheless, the measured and predicted corner rises for each slab system are very close (2.62 mm and 2.70 mm). Thus, it can be concluded that the shrinkage step applied to the pavement is a good approximation of slab shrinkage in actual concrete pavements.

Table 5.14: Pavement parameters for the pavement by Jeong [39] and the current modelled pavement

Parameter	Early-Age Curling and Warping Behaviour [39]	Current pavement system
Number of dowels Dowel spacing Dowel diameter Dowel length	12 305 mm 31 mm 457 mm	11 300 mm 32 mm 450 mm
Slab length Slab width Slab thickness	9.15 m 3.66 m 305 mm	8.5 m 4.2 m 250 mm
Concrete modulus of elasticity	18.0 GPa tested on day 1 25.0 GPa tested on day 3 27.2 GPa tested on day 6 29.8 GPa tested after 2 years ($f_c' = 43.1$ MPa)	22.5 GPa ($f_c' = 30$ MPa)
Concrete coefficient of thermal expansion	$11.3 \times 10^{-6}/°C$	$11.0 \times 10^{-6}/°C$
Applied shrinkage	Back-calculated temperature difference -34.3°C	Equivalent temperature difference applied -34.1°C
Corner rise	2.62 mm	2.70 mm

5.4.3 Temperature Steps Verification

The temperature function results could not be verified using the study by Jeong (used to verify shrinkage), because the effects of temperature variations were recorded only for the first 7 days after the concrete was cast, in the field study. At early-age, the response of the pavement is different than at maturity because of the curing of the concrete.

As outlined in the previous chapter, a similar approach to the simulation of shrinkage has been used to model the effects of daily temperature variations. The temperature gradients of $+9°C$ (day) and $-8°C$ from top to bottom falls in the 0 to 12°C range of frequently observed gradients in the field [36, 46]. Since measurements in the field will always include a shrinkage contribution and seasonal temperature variations, only approximate verification is possible. Heath [28] reports field vertical slab displacements due to temperature variations of approximately 2.5 mm. Table 5.15 displays the displacements predicted by the 3D-

FEM model; the reference for the relative displacement measurement is the slab corner minimum displacement, which is in the day-time. The maximum relative displacement obtained during the night-time is slightly higher than the reported field values, however the slabs instrumented in the study by Heath were shorter slabs (3.66 m $\times$ 3.96 m $\times$ 200 mm). Overall, the order of magnitude of slab deflections is consistent with typical field measurements.

Table 5.15: Predicted slab corner displacements for the multi-bar model

Step	Absolute displacement	Relative displacement
End of shrinkage	2.70 mm	1.58 mm
Day	1.12 mm	0 mm
Night	3.95 mm	2.83 mm

5.4.4 Conclusion

Overall, the results obtained in this research were consistent with published data and the current finite element model concerning shrinkage application. Temperature modelling could not be verified as accurately, though the order of magnitude concurs with field measurements.

5.5 Discussion

5.5.1 Damage Criteria and Propagation of Damage

The loading function used in this study was chosen and verified to reflect realistic shrinkage and thermal loading on pavements. For this, non-linear shrinkage and temperature strain profiles were implemented in ABAQUS. Damage criteria were developed to interpret the data provided by the program. Under these realistic conditions, the damage criteria were not reached. This suggests that the range of parameters investigated likely will not cause damage. Other reasons could include some simplifications made in the numerical modelling of the pavement.

The application of simulated environmental loading resulted in the onset of concrete damage, though the plastic strain values did not reach the failure criteria, as mentioned

previously. Figure 5.28 represents dowel bar axial force as a function joint opening of the case that was found to be the more detrimental with regards to concrete damage (model 1V60-D25-Corr). It shows a combined elastic-inelastic hysteresis behaviour: energy is lost in the form of plastic damage in the concrete. The linear-elastic component is due to elastic behaviour of the dowel and the concrete, while the inelastic, non-linear behaviour is due to concrete inelasticity. The shift observed from the first cycle to the second could be detrimental to pavement peformance since it is indicative of progressive damage occurring at the joint.

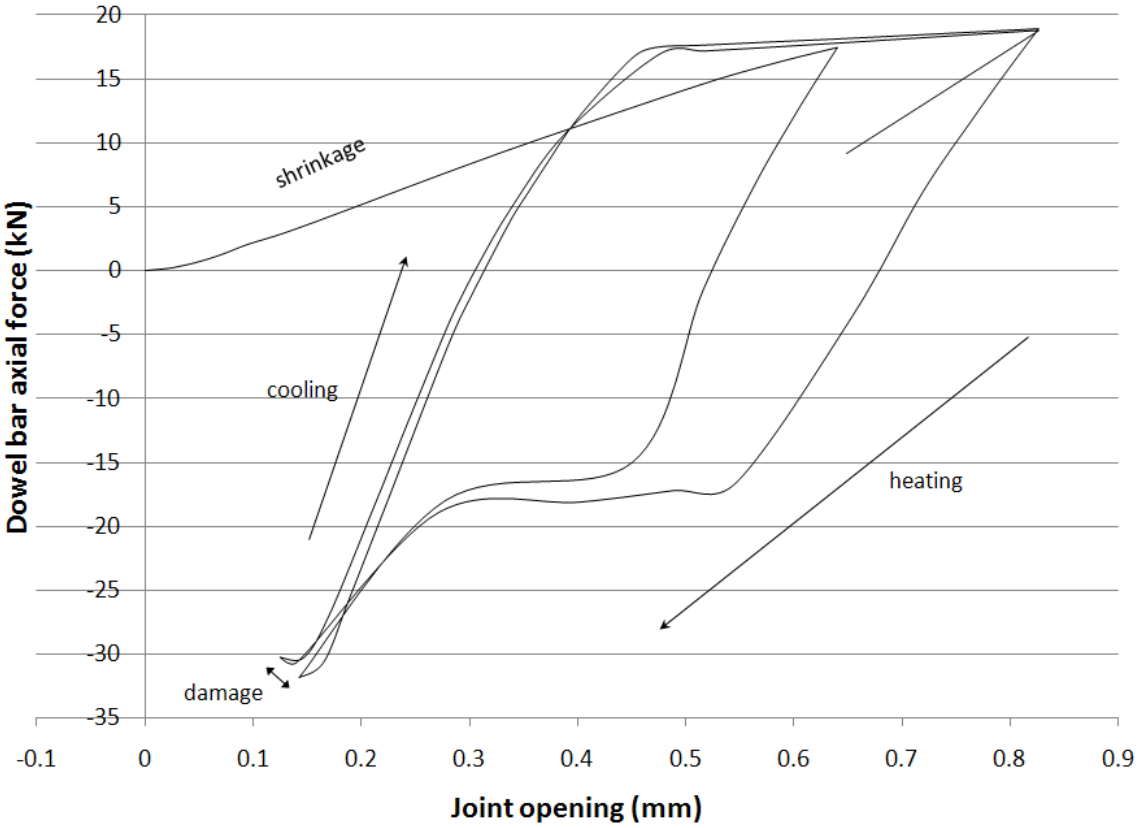

Figure 5.28: Bar force-joint opening behaviour for model 1V60-D25-Corr

To study the effect of additional thermal cycles, a total of 10 cycles was applied to the 1V60-D25-Corr model. The results are represented in Figures 5.29 and 5.30. The first figure, which is a force-opening plot, shows that the additional cycles did not significantly

deviate the shape of the curve. After two cycles, a steady-state is reached. The second figure represents the variation of PEEQ and PEEQT as a function of the loading history, and it is clear from this figure that the plastic strain state stays constant after two cycles. As well, the zone of damaged concrete around the dowel at the joint or at the end of the pocket does not expand after the application of additional thermal cycles, and remains fairly small. Damage stagnates at a specific location, therefore it can be concluded that even the worst case scenario exhibited damage levels below the damage criteria used in this study; damage will not occur.

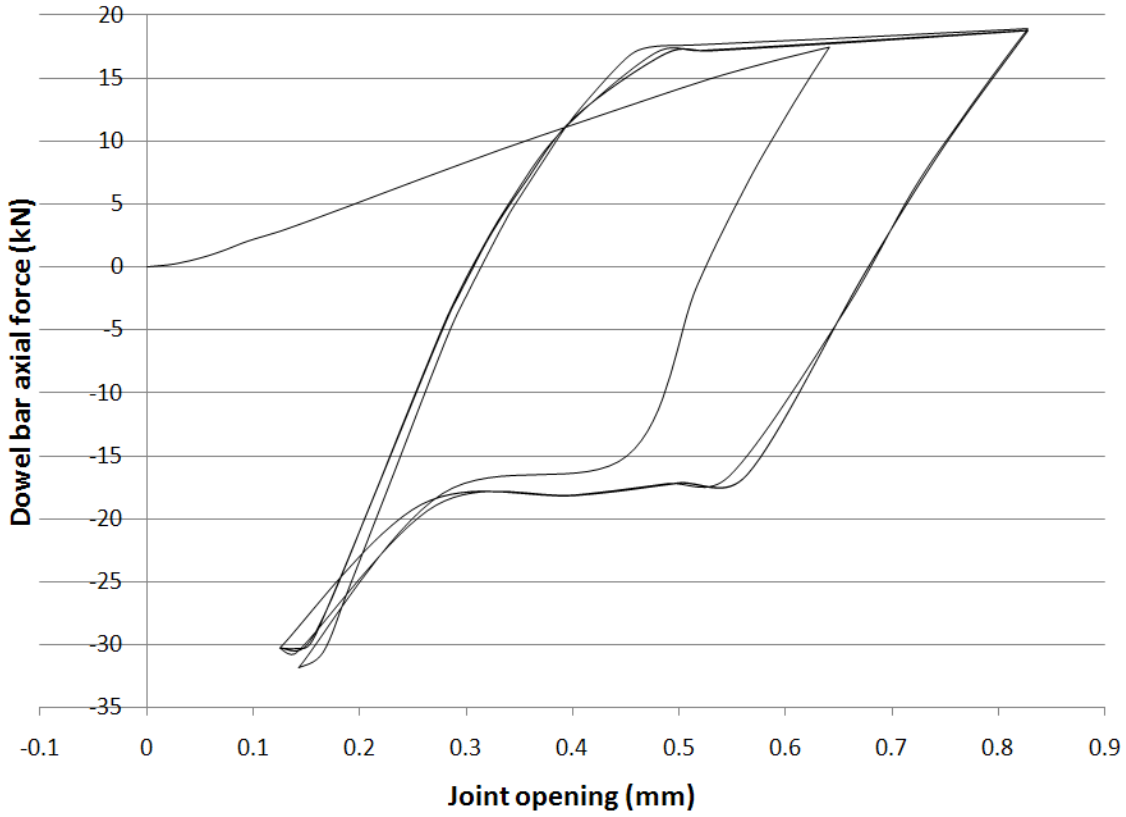

Figure 5.29: Bar force-joint opening behaviour for model 1V60-D25-Corr, 10 temperature cycles total

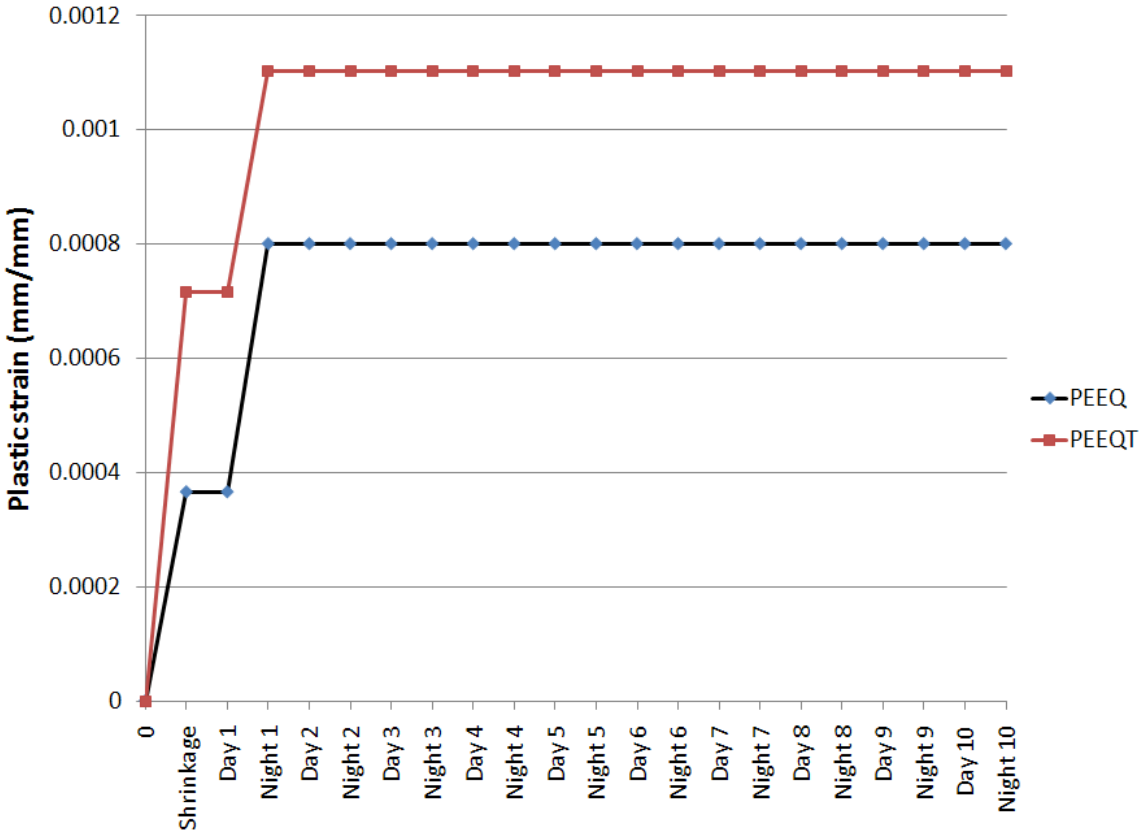

Figure 5.30: Variation of maximum plastic strains for model 1V60-D25-Corr, 10 temperature cycles total

5.5.2 Load Transfer Efficiency

In the last chapter, two important measures of joint load transfer efficiency were presented and used as a comparison tool between the different models. The values obtained from the 3D-FEM analysis for LTE and TLE range from 84.6 % to 89.7 % and from 26.6 % to 32.4 %, respectively. In Shoukry et al. [14], for the same FWD load and dowel bar diameter, averaged field results for LTE and TLE ranged from 77.0 % to 89.4 % and from 8.3 % to 19.0 %, respectively. The variability in results is due to the fact that the FWD testing was done at different locations along the joint. Comparing the 3D-FEM load transfer results from the current study with the field results from Shoukry et al. suggest that the 3D-FEM results are consistent with actual LTE results. For TLE, the 3D-FEM predicts higher values than

those reported by Shoukry et al. This difference may be because only one bar is modelled and thus, all of the load has to be transferred by the concrete and the dowel below the FWD location. This is in contrast to the actual pavement where some of the load in transferred through the adjacent concrete and dowels. Overall, the comparison of the 3D-FEM results and field data suggests that the model is a close representation of true behaviour. The high values of load transfer efficiency for all of the models in the current study suggest that all the models performed well at transferring the load across the joint, and that local damage of concrete had a negligible effect on joint efficiency.

5.5.3 Model Shortcomings and Limitations

Some simplifications and assumptions were made to carry out the 3D-FEM analysis. The range of the conclusions made is therefore limited to the idealized conditions considered in this study. Those limitations could be addressed by future research.

- The single bar model was simplified to focus on the fundamental behaviour of one bar embedded in concrete; this prevents from observing the effects of combined misalignment of dowel bars.
- The properties of materials were chosen as being not dependent on: (1) time, and (2) temperature. Hence, early-age behaviour cannot be simulated with this choice of parameters; temperature-dependent data could require to make some adjustments to the outcomes of the current analysis.
- Dowel bar looseness (gaps between the dowel and surrounding concrete caused by poor construction) was not modelled.
- Repetitive traffic loading was not included.
- Multiple (more than 2) thermal cycles were not considered, except for one extreme case, which exhibited no accumulation of damage in the concrete.

5.6 Conclusions

The analysis of the single bar model has provided valuable insight on the behaviour of the slab-dowel system when subjected to shrinkage and temperature loading. Shrinkage and cooling (night) primarily have consequences on the occurrence of damage around the dowel bar at the joint since both phenomena tend to cause the slab to curl upwards. The heating process (day) causes dowel-concrete end-bearing behaviour, but it was shown that the damaged zone remained restricted to a small area around the dowel.

The following conclusions were made based on the analysis of the single bar model:

- For a non-misaligned bar, the bar forces and moments and the joint deflections increase as the bar is displaced vertically by 25 mm upwards; concrete damage around the dowel at the joint is increased. For a misaligned bar, the bar forces and moments are comparable, while the joint deflections are reduced; damage is reduced in compression and increased in tension. This is due to the effects of slab curling, which leads to a non-symmetrical behaviour of the dowel and concrete interaction. For misaligned and non-misaligned cases, as the vertical displacement increases, joint load transfer efficiency is improved.

- For a bar placed at midslab, as angular misalignment in a vertical plane increases, the joint deflections are reduced, and the bar forces and moments increase. Load transfer efficiency is improved by misalignment, due to joint locking effects. As angular misalignment increases, concrete damage becomes significantly more severe, although it does not reach the failure criteria used in this study. Since LTE and TLE increase, this suggests that the damage occuring at the joint is not serious enough to influence joint load transfer, and that the joint locking effects have a stronger impact on joint load transfer than concrete damage.

- For a bar vertically displaced by + 25 mm, no clear trend could be determined concerning the effects of angular misalignment on joint deflections and bar forces, as

the model with the smallest amount of angular misalignment exhibited the highest bar forces. Yet, the bar moment increases as the angular misalignment increases. Concrete damage at the joint increases but not on both sides: it increases on the side of the joint where the bar is lower while it decreases on the side of the joint where the bar is higher. This non-symmetrical behaviour is caused by the combined upward curling and shortening of the slab, which induces higher concrete bearing stresses on the side of the joint where the bar is lower and a more pronounced slip of the bar against the concrete on the other side compared to a less misaligned case. This may explain why the bar forces and joint deflections do not reveal a clear trend in their variations with bar misalignment.

- Models with different friction coefficients between the dowel and the concrete were tested; a low coefficient of friction simulates the application of a bond breaker, a medium friction corresponds to an uncoated bar, and a high friction simulates a corroded bar. For a non-misaligned bar placed at mid-height of the slab, a decrease in the coefficient of friction induces a decrease in the joint deflections and an increase in the bar force and moment. Reducing the friction coefficient leads to more damage in the concrete, while at the same time improves the joint load transfer efficiency.

- For misaligned bars, an increase in the coefficient of friction causes an increase in the joint deflections and a decrease in bar force, whereas bar moment increases. As the friction coefficient is reduced, concrete damage is reduced, and load transfer efficiency is slightly reduced.

- A reduction in the coefficient of thermal expansion of the concrete causes a reduction is joint deflections when the bar is place at midslab, and an increase in joint deflections when the bar is vertically displaced (+ 25 mm). In all the cases, as the coefficient of thermal expansion decreases, the bar force and moment are reduced, and concrete damage is reduced as well; LTE is comparable or reduced.

- An increase in the compressive strength of concrete is accompanied by a reduction in

joint deflections but an increase in bar force and moment; the compressive strains in the concrete as increased without reaching failure while concrete damage in tension is reduced.

Chapter 6

Conclusions and Recommendations for Future Research

This chapter presents a summary and conclusions from the numerical investigations. Recommendations and future work advice are also provided.

6.1 Summary

A comprehensive study was conducted on the dowel bar-concrete interaction effect on a rigid pavement joint behaviour. A 3D finite element model representing one bar was subjected to shrinkage and thermal loading (two thermal cycles applied). The influence of the following parameters were studied:

- Dowel bar placement (vertical displacement and angular misalignment in a vertical plane);
- Use of a bond breaker;
- Concrete coefficient of thermal expansion;
- Concrete compressive strength.

The model was verified using relevant case studies found in the literature.

The current study included non-linear effects of shrinkage and thermal loading, combined with a non-linear concrete behaviour capable or representing damage. This is a development in a realistic numerical modelling of pavement behaviour, and in particular joint behaviour, since most of the studies on dowel bar misalignment so far simply replicate a laboratory pullout test, without consideration of slab curling. Moreover, in experimental conditions, high values of joint opening are obtained compared to realistic daily joint openings: Leong et al. used 14 mm, Buch et al. used 12.7 mm [3, 5]. Therefore, the current study is expected to provide a more realistic representation of slab behaviour and the effect of variables.

6.2 Conclusions

The following observations were made based on the 3D-FEM models results:

- For a non-misaligned bar, the bar forces and moments and the joint deflections increase as the bar is displaced vertically by 25 mm upwards; concrete damage around the dowel at the joint is increased. For a misaligned bar, the bar forces and moments are comparable, while the joint deflections are reduced; damage is reduced in compression and increased in tension. Joint load transfer efficiency is improved when the bar is placed up higher.

- For a bar placed at midslab, as the angular misalignment increases, the joint deflections are reduced while the bar forces, moments and the damage in the concrete are increased. However, the concrete strains do not reach failure. Joint locking effects cause load transfer efficiency to improve with increasing angular misalignment.

- For a bar vertically displaced by + 25 mm, a non-symmetrical behaviour is observed with increasing angular misalignment, due to slab curling: concrete damage at the joint increases on the side where the bar is lower while it decreases on the other side. Joint deflections, bar forces and moment are not linear functions of bar angular

misalignment.

- Models with different friction coefficients between the dowel and the concrete were tested; a low coefficient of friction simulates the application of a bond breaker, a medium friction corresponds to an uncoated bar, and a high friction simulates a corroded bar. For a non-misaligned bar placed at mid-height of the slab, a reduction in the friction coefficient causes a decrease in the joint deflections and an increase in the bar force and moment, and causes more damage in the concrete, while at the same time improves the joint load transfer efficiency.

- For misaligned bars, as the coefficient of friction increases, the joint deflections and the bar moment increase while the bar force decreases. A lower friction coefficient reduces concrete damage but slightly decreases load transfer efficiency.

Based on the observations from the 3D-FEM models, the following conclusions were drawn:

- None of the models showed signs of significant damage after the application of shrinkage and two thermal cycles. Analyses with up to ten thermal cycles did not indicate progressive accumulation of damage, suggesting that two thermal cycles are sufficient to study slab behaviour.

- As expected, models with bars placed higher in the slab and bars with angular misalignment exhibited more damage than the non-misaligned models. However, even the model with a level of angular misalignment of 60 mm (higher than the greatest level of misalignment observed in the field by Leong [15]) did not reach the damage criteria used in this study. For realistic pavement deflections under environmental and thermal loading, no significant damage could be found in any of the models. The models did not exhibit the amount of damage reported in the studies having used pull-out tests; note that the pull-out tests simulated large joint openings but did not include slab curling. This is a finding suggesting that the the severity of some misalignment toler-

ances guidelines could be reconsidered, assuming impeccable pavement construction practice.

- A high coefficient of friction between the dowel and the concrete, simulating dowel bar corrosion, proved to be the most detrimental to joint integrity. Equivalent tensile plastic strains as high as 83 % of the failure plastic strain used in this study were estimated. However, no significant difference could be found between uncoated and coated dowel bars models. This suggests that the use of a specific bond breaker material (grease or oil) is unneeded in normal conditions; furthermore, the use of corrosion-protective coating (epoxy, tectyl) already provides some bond-breaking ability.

- A low coefficient of thermal expansion can be beneficial by limiting thermal strains, thereby reducing joint movements and damage at the joint.

- Increasing the compressive strength of the concrete did not provide a significant advantage regarding the joint behaviour under environmental loading.

6.3 Future Research

Based on the conclusions of the current research, some future work is needed to gain further insight on the behaviour of rigid pavement with dowel bars. This includes:

- Cyclic thermal analysis on a full width, multi-bar pavement model. This would be very helpful to determine if for combined dowel bar misalignment, cyclic thermal loading creates damage propagation and accumulation that would have an effect on joint performance and durability.

- Combined axle loading and cyclic thermal analysis. Studying the superposition of wheel loads to thermal and shrinkage loads is needed to determine how well a pavement will perform on the field.

- Development of performance and life cycle cost models which incorporate the damage.

References

[1] FHWA. *Best Practices for Dowel Placement Tolerances*. Concrete Pavement Technology Program, TechBrief, Federal Highway Administration, Washington, D.C., 2007. 2, 12, 13

[2] Shiraz D. Tayabji. *Dowel Placement Tolerances for Concrete Pavement*. Transportation Research Record No. 1062, Transportation Research Board, Washington, D.C., 1986. 2, 4, 5, 11, 12, 22

[3] Patrick Leong, Susan Tighe, Leo Rothenburg, and David Hein. *Effect of Pavement Variables on Average Joint Deflections in Experimental Concrete Pavement*. Transportation Research Record No. 1946, Transportation Research Board, Washington, D.C., 2006. 2, 25, 138

[4] Lev Khazanovich, Neeraj Buch, and Alex Gotlif. *Evaluation of Alignment Tolerances for Dowel Bars and their Effects on Joint Performance*. Final Report RC-1395, Michigan State University, Pavement Research Center of Excellence, June 2001. 2, 23, 24, 62, 63

[5] Neeraj Buch, Amit H. Varma, and Milind L. Prabhu. *A Laboratory Evaluation of Alignment Tolerances for Dowel Bars and their Effects on Joint Opening Behavior*. Report RC-1487, Michigan State University, February 2007. 2, 26, 27, 28, 29, 55, 60, 64, 138

[6] Neeraj Buch, Amit H. Varma, and Milind L. Prabhu. *Analytical Investigation of the Effects of Aligned Dowel Bars Coated with Corrosion Protective Systems on Initial Dowel*

Concrete Bond Stresses. Report RC-1488, Michigan State University, February 2007. 2, 29, 30

[7] Mourad Y. Riad. *Stress Concentration around Dowel Bars in Jointed Rigid Concrete Pavement*. Master's thesis, West Virginia University, Department of Civil and Environmental Engineering, Morgantown, WV, 2001. 2, 20, 21

[8] James L. Burati, Michael G. Beeson, and Hoke S. Hill. *Comparative Analysis of Dowel Placement in Portland-Cement Concrete Pavements*. Transportation Research Record No. 1684, Transportation Research Board, Washington, D.C., 1983. 2, 11

[9] MoDOT. *Investigation of Dowel Bar Placement Accuracy with a Dowel Bar Inserter*. RDT 03-009/RI01-049, Missouri Department of Transportation, 2003. 2, 12

[10] *Pavement Guide Interactive*. University of Washington, 2005. http://training.ce.washington.edu/PGI/. 6, 7, 8, 9, 10

[11] FHWA. *Concrete Pavement Joints*. Technical Advisory T 5040. 30, Federal Highway Administration, Washington, D.C., November 1990. http://www.fhwa.dot.gov/legsregs/directives/techadvs/t504030.htm. 6, 7

[12] FHWA. *Long-Life Concrete Pavements in Europe and Canada*. Federal Highway Administration, Washington, D.C., 2007. http://international.fhwa.dot.gov/pubs/pl07027/index.cfm. 6, 9

[13] Anastasios M. Ioannides and George T. Korovesis. *Analysis and Design of Doweled Slab-on-Grade Pavement Systems*. Journal of Transport Engineering, Vol. 118, No. 6, November/December 1992, pages 745-768. 8, 9

[14] Samir N. Shoukry, Gergis W. William, and Mourad Y. Riad. *Evaluation of Load Transfer Efficiency Measurement*. Report No. WVU-2002-04, West Virginia University, Department of Civil and Environmental Engineering, Morgantown, WV, July 2005. 8, 19, 132

[15] Patrick K. K. Leong. *Analysis of Effect of Dowel Bar Misalignment on the Performance of Concrete Pavement Joints*. Master's thesis, University of Waterloo, Department of Civil Engineering, Ontario, Canada, 2005. 9, 13, 139

[16] GOMACO. *GOMACO World 28.3: Step by Step: IDBI*. December 2000. http://www.gomaco.com/resources/worldstories/world28_3/idbistepbystep.html. 10

[17] Paul A. Okamoto. *Field Evaluation of Dowel Placement Along a Section of Interstate 45 in Texas*. Transportation Research Record No. 1186, Transportation Research Board, Washington, D.C., 1988. 12

[18] FHWA. *Distress Identification Manual for the Long-Term Pavement Performance Program*. FHWA-RD-03-031, Federal Highway Administration, Washington, D.C., June 2003. 14, 15, 16

[19] Andrew Bodocsi, Issam A. Minkarah, Rajagopal S. Arudi, Mahesh Bhupalam, and Anurag Kak. *Effect of Pavement Variables on Average Joint Deflections in Experimental Concrete Pavement*. Transportation Research Record No. 1449, Transportation Research Board, Washington, D.C., 1994. 17

[20] Syam S. Mannava, Thomas D. Bush, and Anant R. Kukreti. *Load-Deflection Behavior of Smooth Dowels*. ACI Structural Journal, Vol. 96, No. 6, November/December 1999, pages 891-898. 17

[21] Judith Corley-Lay and Clark S. Morrison. *Thirty-Three-Year Performance of Jointed Concrete Test Sections in North Carolina*. Transportation Research Record No. 1806, Transportation Research Board, Washington, D.C., 2002. 18

[22] Jiwon Kim and Keith D. Hjelmstad. *Three-Dimensional Finite Element Analysis of Doweled Joints for Airport Pavements*. Transportation Research Record No. 1853, Transportation Research Board, Washington, D.C., 2003. 18

[23] Samir N. Shoukry, Gergis W. Willliam, Mourad Y. Riad, and Sri vani Sirisha Motamarri. *Effect of Bonding Force on Stresses in Concrete Slabs*. Report No. MAUTC #12, West Virginia University, Department of Civil and Environmental Engineering, Morgantown, WV, July 2003. 21, 22, 62, 63, 64

[24] R.I. Gilbert. *Shrinkage, Cracking and Deflection – the Serviceability of Concrete Structures*. Electronic Journal of Structural Engineering, 2001. 30, 34

[25] Erika E. Holt. *Early age autogenous shrinkage of concrete*. Technical Research Centre of Finland, VTT Publications, Espoo 2001. 30

[26] Rajeev Goel, Ram Kumar, and D. K. Paul. *Comparative Study of Various Creep and Shrinkage Prediction Models for Concrete*. Journal of materials in civil engineering, ASCE, March 2007. 31, 32

[27] J.-K. Kim and C.-S. Lee. *Prediction of Differential Drying Shrinkage in Concrete*. Cement and Concrete Research, Vol. 28, No. 7, 1998, pages 984-994. 31, 32, 65, 66

[28] Andrew C. Heath and Jeffery R. Roesler. *Shrinkage and Thermal Cracking of Fast Setting Hydraulic Cement Concrete Pavements in Palmdale, California*. Preliminary report, California Department of Transportation, December 1999. 31, 36, 37, 128

[29] Zachary C. Grasley and David A. Lange. *Modeling Drying Shrinkage Stress Gradients in Concrete*. Journal of Testing and Evaluation, Vol. 26, No. 2, September 2002. 31

[30] W. Jason Weiss, Wei Yang, and Surendra P. Shah. *Shrinkage Cracking of Restrained Concrete Slabs*. Journal of Engineering Mechanics, Vol. 124, No. 7, July 1998. 33, 34

[31] Seungwook Lima, Jin-Hoon Jeongb, and Dan G. Zollinger. *Moisture Profiles and sShrinkage in Early-Age Concrete Pavements*. International Journal of Pavement Engineering, Vol. 10, No. 1, February 2009, pages 29-38. 35, 36

[32] Wei Liu and Tien Fang Fwa. *Effects of Nonlinear Temperature Distribution on Stresses in Concrete Pavements*. Journal of the Eastern Asia Society for Transportation Studies, Vol. 5, October 2003, pages 1023-1034. 38

[33] Kamyar C. Mahboub, Yinhui Liu, and David L. Allen. *Evaluation of Temperature Responses in Concrete Pavement*. Journal of Transportation Engineering, May/June 2004, pages 395-401. 38, 39

[34] Steven A. Wells, Brian M. Phillips, and Julie M. Vandenbossche. *Characterizing Strain Induced by Environmental Loads in Jointed Plain Concrete Pavement*. Transportation Research Record No. 1947, Transportation Research Board, Washington, D.C., 2006. 39, 40

[35] Dhananjay Rao Hejamadi. *Thermal Stress in Concrete Slabs under Different Constraints*. Master's thesis, West Virginia University, Department of Mechanical and Aerospace Engineering, Morgantown, West Virginia, 2006. 40, 41

[36] Chia pei Chou and Mei hui Lee. *Analysis of Slab Thermal Stresses and Concrete Joint Movements*. International Journal of Pavement Research and Technology, Vol. 1, No. 4, October 2008, pages 148-154. 42, 68, 128

[37] Seung Woo Lee. *Characteristics of Friction between Concrete Slab and Base*. KSCE Journal of Civil Engineering, Vol. 4, No. 4, December 2000, pages 265-275. 43, 44, 61

[38] J. Zhang and B. Leng. *Analysis of Shrinkage-Induced Stresses in Concrete Pavements*. Magazine of Concrete Research, Vol. 56, No. 10, December 2004, pages 585-595. 45, 46

[39] Jin-Hoon Jeong and Dan G. Zollinger. *Early-Age Curling and Warping Behavior*. Transportation Research Record No. 1896, Transportation Research Board, Washington, D.C., 2004. 46, 68, 69, 127, 128

[40] ABAQUS. *ABAQUS Online Documentation: Version 6.7*. Dassault Systèmes, 2007. http://129.97.46.200:2080/v6.7/. 54, 55, 56, 57, 58, 59, 60

[41] A. Van Gysel and L. Taerwe. *Analytical Formulation of the Complete Stress-Strain Curve for High Strength Concrete*. Materials and Structures, Vol. 29, November 1996, pages 529-533. 56

[42] FIB. *Constitutive Modelling of High Strength/High Performance Concrete: State-of-the-art Report*. Task Group 8.2, Fédération Internationale du Béton, 2008. 58

[43] Elin A. Jensen and Will Hansen. *Fracture Energy Test for Highway Concrete*. Transportation Research Record No. 1730, Transportation Research Board, Washington, D.C., 2000. 58, 79

[44] American Concrete Institute. *Prediction of Creep, Shrinkage, and Temperature Effects in Concrete Structures*. ACI 209R-92 (Reapproved 2008). 65, 66

[45] Salah A. Altoubat and David A. Lange. *Creep, Shrinkage, and Cracking of Restrained Concrete at Early Age*. ACI Materials Journal, Vol. 98, No. 4, July-August 2001, pages 323-331. 65

[46] Samir N. Shoukry, G. W. Willliam, and M. Riad. *Nonlinear Temperature Gradient Effects in Dowel Jointed Concrete Slabs*. International Journal of Pavement Engineering, 4:3, September 2003, pages 131-142. 68, 128